Materials Science & Engineering R xxx (xxxx) xxx–xxx

Contents lists available at ScienceDirect

Materials Science & Engineering R

journal homepage: www.elsevier.com/locate/mser

Thermoelectrics: From history, a window to the future

Davide Beretta[a,b,*], Neophytos Neophytou[c], James M. Hodges[d], Mercouri G. Kanatzidis[d], Dario Narducci[e], Marisol Martin- Gonzalez[f], Matt Beekman[g], Benjamin Balke[h], Giacomo Cerretti[i], Wolfgang Tremel[j], Alexandra Zevalkink[k], Anna I. Hofmann[l], Christian Müller[l], Bernhard Dörling[m], Mariano Campoy-Quiles[m], Mario Caironi[a,*]

[a] Center for Nano Science and Technology @PoliMi, Istituto Italiano di Tecnologia, via Giovanni Pascoli 70/3, 20133 Milano, Italy
[b] Department of Mechanical Engineering, University of California Riverside, Riverside, CA 92521, USA
[c] School of Engineering, University of Warwick, Coventry, CV4 7AL, UK
[d] Chemistry Department, Northwestern University, Evanston, IL 60208, USA
[e] University of Milano Bicocca, Dept. Materials Science, via R. Cozzi 55, I-20125 Milano, Italy
[f] Instituto de Micro y Nanotecnología, IMN-CNM-CSIC, Tres Cantos, Madrid, 28760, Spain
[g] Department of Physics, California Polytechnic State University, San Luis Obispo, CA 93407, USA
[h] Institute for Materials Science, University Stuttgart, 70569 Stuttgart, Germany
[i] Thermal Energy Conversion Technologies, Jet Propulsion Laboratory, California Institute of Technology, 4800 Oak Grove Drive, Pasadena, CA 91109-8099, USA
[j] Institut für Anorganische Chemie und Analytische Chemie, Johannes Gutenberg - Universität, Duesbergweg 10-14, 55099 Mainz, Germany
[k] Chemical Engineering and Materials Science Department, Michigan State University, East Lansing, MI, USA
[l] Department of Chemistry and Chemical Engineering, Chalmers University of Technology, 41296 Göteborg, Sweden
[m] Institute of Materials Science of Barcelona (ICMAB-CSIC), Campus of the UAB, Bellaterra, 08193, Spain

ARTICLE INFO

Keywords:
Thermoelectrics
Seebeck
Peltier
Power factor
Electrical conductivity
Thermal conductivity
Materials
Theory
Transport
Complex materials
Nanostructure
History

ABSTRACT

Thermoelectricity offers a sustainable path to recover and convert waste heat into readily available electric energy, and has been studied for more than two centuries. From the controversy between Galvani and Volta on the *Animal Electricity*, dating back to the end of the XVIII century and anticipating Seebeck's observations, the understanding of the physical mechanisms evolved along with the development of the technology. In the XIX century Ørsted clarified some of the earliest observations of the thermoelectric phenomenon and proposed the first thermoelectric pile, while it was only after the studies on thermodynamics by Thomson, and Rayleigh's suggestion to exploit the Seebeck effect for power generation, that a diverse set of thermoelectric generators was developed. From such pioneering endeavors, technology evolved from massive, and sometimes unreliable, thermopiles to very reliable devices for sophisticated niche applications in the XX century, when Radioisotope Thermoelectric Generators for space missions and nuclear batteries for cardiac pacemakers were introduced. While some of the materials adopted to realize the first thermoelectric generators are still investigated nowadays, novel concepts and improved understanding of materials growth, processing, and characterization developed during the last 30 years have provided new avenues for the enhancement of the thermoelectric conversion efficiency, for example through nanostructuration, and favored the development of new classes of thermoelectric materials. With increasing demand for sustainable energy conversion technologies, the latter aspect has become crucial for developing thermoelectrics based on abundant and non-toxic materials, which can be processed at economically viable scales, tailored for different ranges of temperature. This includes high temperature applications where a substantial amount of waste energy can be retrieved, as well as room temperature applications where small and local temperature differences offer the possibility of energy scavenging, as in micro harvesters meant for distributed electronics such as sensor networks. While large scale applications have yet to make it to the market, the richness of available and emerging thermoelectric technologies presents a scenario where thermoelectrics is poised to contribute to a future of sustainable future energy harvesting and management.

This work reviews the broad field of thermoelectrics. Progress in thermoelectrics and milestones that led to the current state-of-the-art are presented by adopting an historical footprint. The review begins with an historical excursus on the major steps in the history of thermoelectrics, from the very early discovery to present technology. A panel on the theory of thermoelectric transport in the solid state reviews the transport theory in

* Corresponding authors at: Department of Mechanical Engineering, University of California Riverside, Riverside, CA 92521, USA.
E-mail addresses: mail.davide.beretta@gmail.com (D. Beretta), mario.caironi@iit.it (M. Caironi).

https://doi.org/10.1016/j.mser.2018.09.001
Received 24 July 2018; Received in revised form 7 September 2018; Accepted 17 September 2018

complex crystal structures and nanostructured materials. Then, the most promising thermoelectric material classes are discussed one by one in dedicated sections and subsections, carefully highlighting the technological solutions on materials growth that have represented a turning point in the research on thermoelectrics. Finally, perspectives and the future of the technology are discussed in the framework of sustainability and environmental compatibility.

Nomenclature

List of symbols

α	Seebeck coefficient [V K^{-1}]
α_p	Seebeck coefficient of *p*-type thermoelements [V K^{-1}]
α_n	Seebeck coefficient of *n*-type thermoelements [V K^{-1}]
$\alpha_{pn} = \alpha_p - \alpha_n$	Seebeck coefficient of thermocouples [V K^{-1}]
π	Peltier coefficient [V m^{-1}]
τ	Thomson coefficient [V K^{-1}]
σ	Electrical conductivity [Ω^{-1} m^{-1}]
ρ	Electrical resistivity [Ω m]
κ	Thermal conductivity[W m^{-1} K^{-1}]
κ_{el}	Electronic contribution to the thermal conductivity [W m^{-1} K^{-1}]
κ_{ph}	Phonon/lattice contribution to the thermal conductivity [W m^{-1} K^{-1}]
R	Electrical resistance [Ω]
K	Thermal conductance[W K^{-1}]
$PF = \sigma\alpha^2$	Power factor [W m^{-1} K^{-2}]
V	Voltage [V]
T	Absolute temperature [K]
$\dot{Q}$	Heat per un unit time [W]
$\dot{q}$	Heat per unit time per unit volume [W m^{-3}]
i	Electric current [A]
$\boldsymbol{j}$	Electric current density vector [A m^{-2}]
DOS	Density of states [m^{-3} J^{-1}]
E	Energy [J]
μ	Mobility [m^2 V^{-1} s^{-1}]
m^*	Effective mass [kg]

1. History of thermoelectrics

The first evidences of the direct conversion between thermal and electrical energy date back to the end of the XVIII century. In those years, the Italian physician, physicist, biologist and philosopher Luigi Aloisio Galvani (Bologna, September 9, 1737 - Bologna, December 4, 1798), who was conducting experiments at the university of Bologna on the effect of electricity on animals, was about to discover what is now given the name of galvanism. In the late 1780s, Galvani accidentally observed muscles contractions in a dead frog sample when its crural nerves were touched by a conductive lancet and sparks were simultaneously emitted from a nearby electric machine [1]. This unexpected phenomenon set the ground for a series of experiments aimed at understanding the role of electricity in living beings, which eventually led to the discovery of muscles contractions in dead frogs when the muscles and the crural nerve were short circuited by means of a metallic body (see Fig. 1a). To explain the phenomenon, Galvani supposed that the nerves and the muscles were electrically unbalanced, and that the muscles contractions occurred when the electrical equilibrium was restored by short-circuiting the nerve and the muscles with a metallic body, in analogy with what occurs in a Leyden Jar. This reasoning led him to conclude that muscles acted as some sort of reservoir for electricity in living beings, the discharge of such electricity being commanded by the brain. Although unable to correctly explain the pehonomenom, Galvani's research triggered the interest of the Italian physicist and chemist Alessandro Giuseppe Antonio Anastasio Volta (Como, February 18, 1745 - Como, March 5, 1827) who, conducting similar experiments at the University of Pavia, noticed the particular efficacy of arcs made of dissimilar metals at provoking muscles contractions. He then conceived the possibility that muscles contractions were induced by some amount of electricity externally produced by experimental manipulations, ultimately assuming that the electric disequilibrium was produced by the metallic contact, and that muscle contractions were a simple response to external stimuli [2]. To support his thesis, Volta even explored the effect of a bi- metallic arc on his own tongue, feeling and correctly interpreting the acid taste perceived as caused by stimulation of gustatory nerves by the current flowing in and out of his tongue [3]. This clearly contradicted Galvani's hypothesis on muscles as electrical reservoirs, and initiated one of the most debated scientific controversies in history that would result in the birth of electrophysiology, electromagnetism and electrochemistry, and the invention of the electrical battery [4]. Still, Volta wasn't able to relate the muscles contractions to the temperature difference of the metallic junctions until he set up an experiment (shown in Fig.1b) where a dead frog was prepared in such a way that its hind legs were immersed in one glass full of water, while its back spine in another one, and both glasses were short circuited by a metallic arc [2]. In this configuration, Volta was able to observe violent contractions of muscles only for some

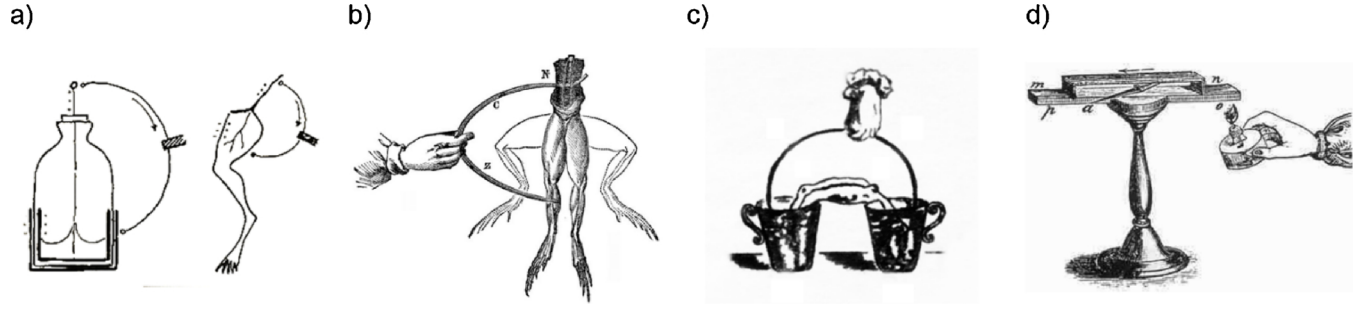

Fig. 1. a) Sketch showing Galvani's analogy between electric discharge in Leyden Jars and electric discharge in frogs. b) Examples of Galvani's and Volta's experiment involving dead frogs and metallic/bimetallic arcs short circuiting the muscles with the crural nerve: when the electrodes touch the frog, the legs twitch into the upward position. c) Scheme of the Volta's experiment on dead frogs that unveiled the thermoelectric effect: short circuiting the two glasses of water with a metallic arc, the muscles of the frog contracts and the frog jumps out of the glasses. Reproduced and adapted from [8]. d) The instrument used by T. J. Seebeck during his experiments. Heating one junction of the bimetallic circuit, he observed a deflection of a nearby magnetic needle [9].

conductors, and he realized that a temperature difference between the water of the two glasses was needed in order for the contractions to occur. After a series of experiments, Volta correctly concluded that the electromotive force originated from the temperature difference between the junctions of two dissimilar conducting materials, ultimately unveiling the thermoelectric effect.

This happened more than twenty years before Johann Seebeck (Tallin, April 9, 1770 - Berlin, December 10, 1831), a German physicist from a wealthy Baltic German family of merchants, observed that a closed circuit made of two dissimilar metals, i.e. a *thermocouple*, deflects a compass magnet placed in proximity of the circuit when the two junctions of the circuit are not isothermal, the angle of deflection depending on the temperature difference between the junctions. Seebeck, who reported his results in 1821 [5], erroneously believed that the observed phenomenon was due to magnetism induced by temperature differences, a conclusion which eventually lead him to suppose that the Earth's magnetic field was a consequence of the temperature difference between the two cold poles and the hot equator. This was happening after the Danish physicist Hans Christian Ørsted (Rudkøbing, August 14, 1777 - Copenhagen, March 9, 1851) proved in 1820 that electrical currents interact with magnetic materials [6]. Moreover, even after Ampere, Biot, Savart, Laplace, and other scientists studied the interaction of electrical currents with magnetic fields, Seebeck disclaimed the electrical nature of the phenomenon and called the observed effect *thermomagnetism* [5]. Although Seebeck misinterpreted the physical origin of the phenomenon, he built a setup similar to the one sketched in Fig. 1d and measured the deflection angle of the magnetic compass due to a series of thermocouples subjected to different temperature differences, hence setting the ground for the very next development of thermoelectricity. The name *thermoelectric* was later coined by Ørsted who, with the help of the mathematician and physicist Jean Baptiste Joseph Fourier (Auxerre, March 21, 1768 - Paris, May 16, 1830), few years later, realized the first thermoelectric pile, made of three bars of bismuth and three bars of antimony [7].

The same thermoelectric device was then improved by two Italian physicists, Leopoldo Nobili (Trassilico, July 5, 1784–Florence, August 22, 1835) and Macedonio Melloni (Parma, April 11, 1798–Portici, August 11, 1854), who, in 1831, presented at the French Academy of Science an Ørsted's thermoelectric pile, consisting of thirty-six thermocouples of antimony and bismuth, used for measurements of temperature and infra-red radiation [7]. Meanwhile, the scientific community had correctly established the physical origin of Seebeck's observations as the electromagnetic interaction between the magnet itself and a current induced in the closed circuit by a temperature difference applied between the metallic junctions [10,11]. Today, the phenomenon of electromotive force generated from temperature gradients is given the name of *Seebeck effect* even if, more precisely, it was discovered much earlier by Alessandro Volta,[1] and is expressed by the Seebeck coefficient

$$\alpha = -\frac{dV}{dT}$$

where V is the electric potential and T the absolute temperature.

The understanding of the Seebeck effect, accompanied by the evolving theories on electromagnetism, initiated a new field of research on the conversion between heat and electrical currents. In 1834, a French watchmaker and part-time physicist, Jean Charles Athanase Peltier (Ham, February 22, 1785–Paris, October 27, 1845), discovered that when a current is forced across an isothermal junction of dissimilar metals, the junction is heated or cooled depending on the direction of the current [12]. Peltier did his best in trying to correlate the phenomenon with the Joule theory of heat dissipation. However, he inevitably failed in finding a satisfactory explanation, and uncertainties about the physical origin of the effect persisted until 1838. That year, the Russian physicist Heinrich Friedrich Emil Lenz (Dorpat, February 12, 1804 - Rome, February 10, 1865) proved that the effect discovered by Peltier is an autonomous physical phenomenon, not directly related to the Joule effect, which consists in the release and absorption of additional heat by junctions between dissimilar conductors when a current is forced across them [13]. Today, this phenomenon is given the name *Peltier effect*, and is quantified by the Peltier coefficient

$$\pi = \frac{\dot{Q}}{i}$$

where $\dot{Q}$ is the heat released or absorbed per unit time at the junction, and i is the electric current flowing through the junction.

Later on, in 1851, Heinrich Gustav Magnus (Berlin, May 2, 1802–Berlin, April 4, 1870), discovered that the Seebeck voltage does not depend on the distribution of temperature along the metals, but only on the temperature difference between the junctions [14]. This was the perfect indication that the Seebeck coefficient is a thermodynamic state function.

However, a comprehensive thermodynamic explanation of the thermoelectric effects had to wait until 1854, when the British mathematical physicist and engineer William Thomson (Belfast, June 26, 1824–Largs, December 17, 1907), also known as Lord Kelvin, finally issued a comprehensive thermodynamic treatment of the Seebeck and Peltier effects [15,16]. Thomson, who did fundamental works at the university of Glasgow on the mathematical analysis of electricity and on the formulation of the first and second law of thermodynamics, was able to predict the existence of a third thermoelectric effect, which manifests itself in the release or absorption of heat when a current flows in a homogeneous material subjected to a temperature gradient. He found that the amount of heat exchanged is proportional to both the electric current and the temperature gradient, and that their mutual direction determines if the heat is absorbed or released. This effect is now given the name *Thomson effect*, and is expressed by the Thomson coefficient

$$\tau = \frac{\dot{q}}{\boldsymbol{j} \bullet \nabla T}$$

where $\dot{q}$ is the heat absorbed or released per unit time and unit volume, and $\boldsymbol{j}$ is the current density. Following a methodology not anymore accepted to describe non-equilibrium thermodynamics, Thomson was finally able to derive the Thomson coefficients for time-reversal-symmetric materials, that is [17]

$$\pi = \alpha T$$

$$\tau = T\frac{d\alpha}{dT}$$

thus demonstrating that the thermoelectric effects are related one to the other.

The discovery and understanding of the three fundamental thermoelectric effects triggered the development of a new field of science and engineering that studies and utilizes the processes of conversion between thermal and electrical energy. It was the British physicist John William Strutt Rayleigh (Langford Grove, November 12, 1842–Witham, June 30, 1919) who suggested in 1885 to exploit the Seebeck effect for power generation [18]. Despite the erroneous results of his work, it can be considered the origin of the thermal-to-electrical energy conversion concept. In the second half of the XIX century, a variety of thermoelectric devices, made of a number of conductors connected electrically in series and thermally in parallel, and exploiting hot gases or liquids as heat source, were designed and realized for the generation of electrical current (see Fig. 2b) [19]. These devices were given the name of thermoelectric generators (TEGs). Among them, the Cox's pile, made of bars of a mixture of zinc and antimony joined by flexible tinned iron,

[1] In July 14, 2005, the International Thermoelectric Academy, gathered in the council room of Como municipality, have finally ascribed the honor of the discovery of the thermoelectric effect to Alessandro Volta [700].

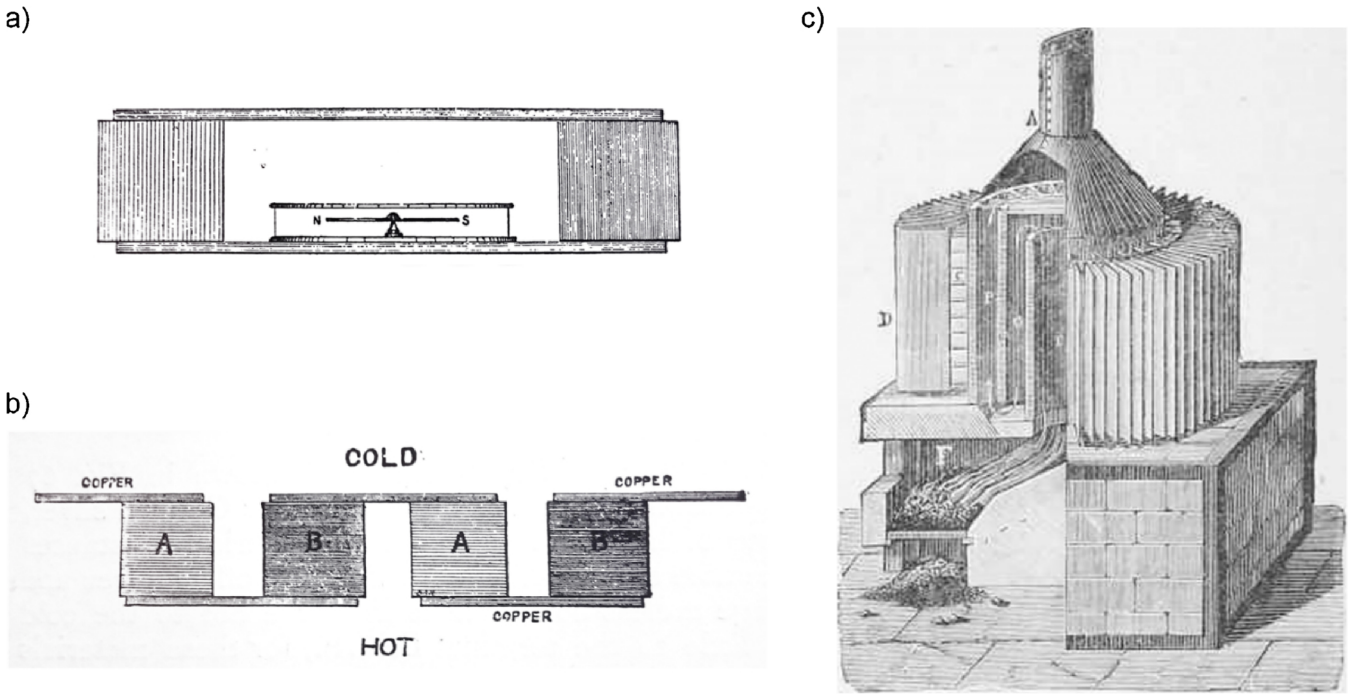

Fig. 2. a) Sketch of a thermoscope made of a couple of dissimilar metals. b) Old scheme of a thermoelectric generator. b) Picture of a Clammond's thermopile. Reproduced and adapted from [19].

received some notoriety because of its unreliability due to the poor mechanical and chemical properties of the constituent materials; the Gulcher thermopile, by better design and construction, was able to stably sustain 1.5 V and deliver a current of 3 A; the Clammond pile (Fig. 2c), built over a coke fireplace, made of 3000 thermocouples, was able to generate no less than 109 V with a maximum power output of approximately 200 W for about 10 kg of burned coke per hour (see Fig. 3) [19]. On the other hand, despite the knowledge of the Peltier effect, devices designed to use electricity for heating or cooling the environment were not even taken into consideration until the discovery of the semiconductor technology, which allowed for larger efficiency of conversions. These devices, based on the Peltier effect, were then given the name of Peltier cells, or simply coolers.

The German physicist Edmund Altenkirch (Ljubljana, August 11, 1880–Unknown, November 28, 1953) was the first who satisfactorily derived, in 1909, the *maximum* efficiency of a thermoelectric generator η, i.e. the ratio between the electric power returned by the generator and the heat per unit time supplied at the hot side, using a simplified model in which the thermoelectric properties of the thermocouples were considered independent from temperature. In 1922, he also derived the coefficient of performance *COP* of a Peltier cooler, i.e. the ratio between the heat per unit time absorbed at the cold side and electric power consumed [20]. Altenkirch found that the efficiency of thermoelectric conversion is proportional to the Carnot's cycle efficiency, which represents its upper limit, and identified the material properties that determines the thermoelectric performance of engines based on the thermoelectric effect. In particular, he discovered that good thermoelectric devices should be made of thermocouples characterized by large Seebeck coefficients, low electrical resistance and low thermal conductance.

Although the scientific community was making great advances in the engineering of thermoelectric devices, the theoretical understanding of the microscopic origins of the thermoelectric effects did not make any progress until the advent of statistical and quantum mechanics, and non-equilibrium thermodynamics. Ludwig Boltzmann (Vienna, February 20, 1844 - Duino, September 5, 1906), an Austrian physicist and philosopher, father of statistical mechanics, played a primary role at this time in history. In fact, his studies on irreversible phenomena set the ground for the subsequent development of non-equilibrium thermodynamics, thus paving the way for the work of the new generations of theoreticians. Among them, the Norwegian-born American physical chemist Lars Onsager (Oslo, November 27, 1903–Coral Gables, October 5, 1976) finally formulated in 1931 a systematic method to describe transport phenomena in systems out of equilibrium, where the approximation of quasi-equilibrium is valid [21,22]. The theory of Onsager has been intensively applied to thermoelectricity, ultimately allowing to derive, in the 1950s, generalized versions of the Thomson coefficients for anisotropic non-time-reversal-symmetric media [23,24], which are currently casted in the form

$$\bar{\bar{\pi}}(\boldsymbol{B}) = \bar{\bar{\alpha}}'(-\boldsymbol{B})T$$
$$\bar{\bar{\tau}}(\boldsymbol{B}) = T\frac{d\bar{\bar{\alpha}}'(-\boldsymbol{B})}{dT}$$

where the double overline indicate tensor quantities, $\boldsymbol{B}$ is the magnetic field, and the apex stands for transposed.

Meanwhile the world had entered one of the darkest periods in history. During World War II, the arms race gave a boost to the whole scientific research, and in the first half of the XX century the semiconductor science and technology made a big jump. Great contributions to the field were given by the Russian physicist Abram Fëdorovič Ioffe (Romny, October 29, 1880 - Leningrad, October 14, 1960), who begun to formulate the modern theory of semiconductor physics. While modeling the conversion efficiency of thermoelectric devices under approximation of temperature- independent thermoelectric properties, in 1949 he introduced for the first time the *dimensionless thermocouple figure of merit* [25]

$$Z\bar{T} = \frac{\alpha_{pn}^2}{KR}\bar{T}$$

where $\alpha_{pn} = \alpha_p - \alpha_n$ is the thermopower of the thermocouple, α_p and α_n being the Seebeck coefficient of the p and n -type thermoelements forming the thermocouple, R the series electrical resistance of the thermoelements, K their thermal parallel conductance, and $\bar{T}$ the

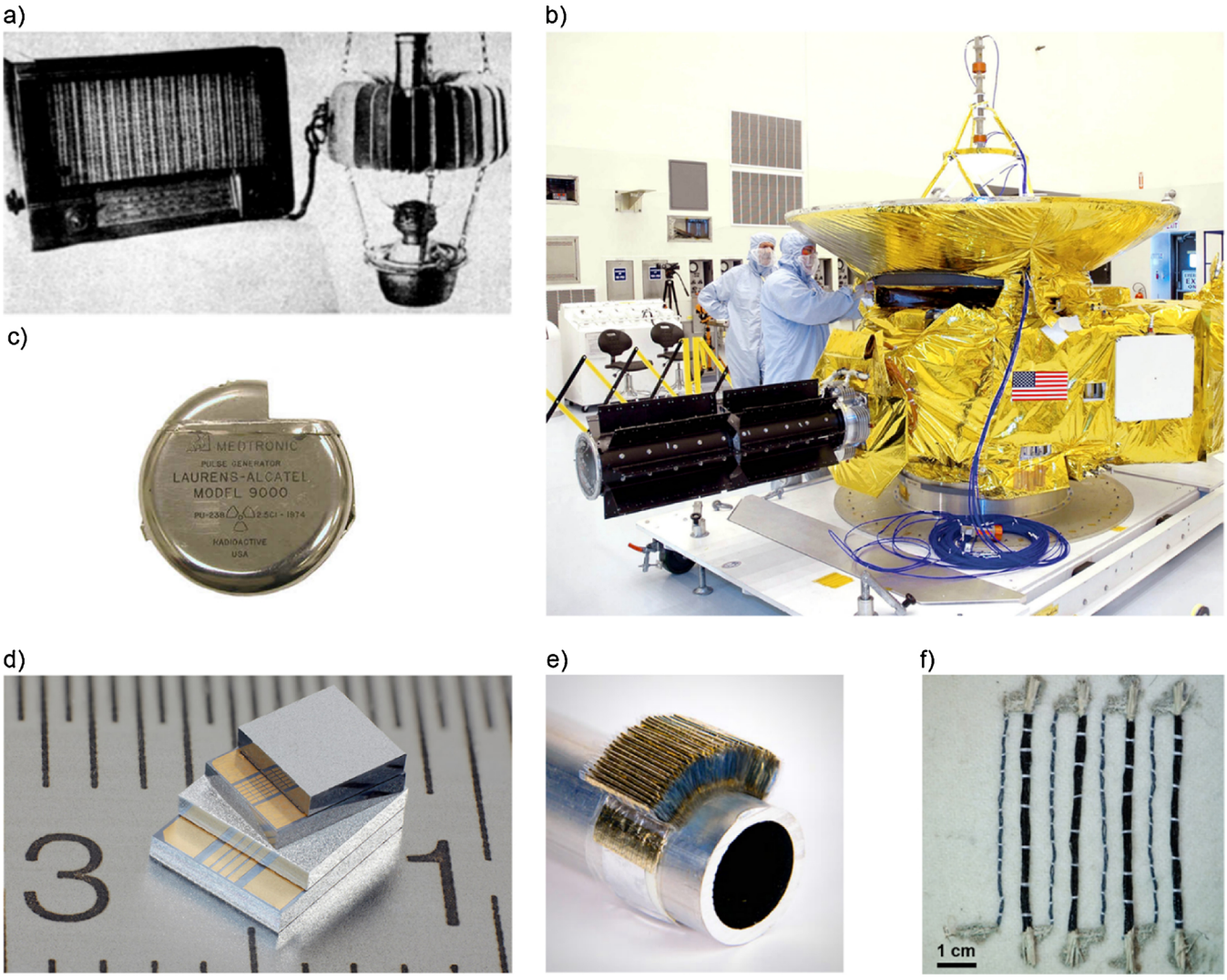

Fig. 3. a) Oil burning lamp powering a radio by means of one of the first commercial thermoelectric generators, made of ZnSb/constantan thermocouples. Built in USSR in the beginning of 1948. Reproduced and adapted from [25]. b) New Horizons in assembly hall. The black RTG is clearly visible on the left side of the satellite. c) Cardiac peacemaker Medtronic Laurens-Alcatel Model 9000, incorporating a small bar of ^{238}Pu as heat source. Reproduced and adapted from [32]. d) Micro thermoelectrics generators from Micropelt. Reproduced and adapted with permission from Micropelt. e) Concept of an organic-based generator design suitable for round surfaces. Reproduced and adapted with permission from otego GmbH. f) In-plane embroidered textile thermoelectric device with 4 n/p elements, comprised of *n*-type coated PET yarns (11 yarns per leg), *p*-type dyed silk yarns (2 yarns per leg) and silver paste for contacts [33].

average absolute temperature at which the thermoelectric device is operating. Ioffe identified in $Z\bar{T}$ a quantity that when maximized leads to the maximization of the conversion efficiency of generators and coolers. Under approximation of constant thermoelectric properties, η and *COP* assume the well-known, and most commonly used, forms [25]:

$$\eta = \frac{\Delta T}{T_h} \times \frac{\sqrt{1+Z\bar{T}} - 1}{\sqrt{1+Z\bar{T}} + \frac{T_c}{T_h}}$$

$$COP = \frac{T_c}{\Delta T} \times \frac{\sqrt{1+Z\bar{T}} - \frac{T_h}{T_c}}{\sqrt{1+Z\bar{T}} + 1}$$

where $\bar{T}$ is the average temperature at which the device is operating. Further considerations on the thermoelectric properties of the *p*- and *n*-type materials forming the thermocouples led him to the introduction, starting from ZT, of the *material dimensionless figure of merit* [25]

$$zT = \frac{\sigma\alpha^2}{\kappa}T$$

where α is the Seebeck coefficient, σ the electrical conductivity, and κ the thermal conductivity of the given material. Although zT was originally derived assuming temperature independent thermoelectric properties, it is currently evaluated as a function of temperature, and since its introduction it has been used as the fundamental parameter for comparison among different materials at different temperatures. Ioffe's studies on semiconductors, which culminates in the classic book *Semiconductor thermoelements, and thermoelectric cooling*, [25] led him to recognize heavily doped semiconductors as the most promising materials for thermoelectric conversion, the best of which at that time were the telluride of antimony, of bismuth and of lead.

The progress in semiconductor technology paved the way for the thermoelectric breakthrough that characterized the immediate post-war period. In particular, in 1947, Maria Telkes (Budapest, December 12, 1900–Boston, December 2, 1995), a Hungarian-American scientist who carried out her studies at the Massachusetts Institute of Technology, was able to fabricate a thermoelectric generator, based on PbS and ZnSb, showing a conversion efficiency higher than 5% when operating under a temperature difference of 400 K [26]. Few years later, in 1954,

Hiroshi Julian Goldsmid, at the research laboratories of The General Electric Company in Wembley, UK, demonstrated cooling at 273 K using a thermoelectric device made of Bi_2Te_3 thermocouples [27]. Meanwhile, in the 1950s, the Soviet Union designed and commercialized ring-shaped thermoelectric generators made of ZnSb/Constantan thermocouples to convert the heat produced by kerosene lamps and power radio receivers for rural areas not directly served by electricity [28].

In the same years, the advancements in solid-state-physics that followed the formulation of statistical mechanics first, and quantum mechanics then in the first half of the XX century, inevitably led to a much deeper understanding of the thermoelectric phenomena. In 1959, Chasmar and Stratton introduced a new way to describe the dimensionless figure of merit by reformulating it in terms of the thermoelectric *material factor*, often referred to as the *material quality factor* and denoted by β. The material factor is a parameter that depends only on the physical properties of the semiconductor, and its maximization corresponds to achieving the maximum possible zT for a given material having a given charge carrier concentration [29].

Nevertheless, the efficiency of thermoelectric devices was still not exceeding 5%. Therefore, despite few unsuccessful attempts to commercialize home products based on thermoelectric cooling, like the full-size refrigerator from Westinghouse launched in 1959, at the end of the 1960s the progress slowed down in favor of more efficient and conventional engines. Consequently, many research programs were dismantled and, little by little, thermoelectrics became a niche field of research. However, the advantages of thermoelectric devices of being solid state, highly reliable, with no mechanical moving parts and thus with limited need of maintenance and probability of failure over long periods, were recognized fundamental in all those situations where accessibility was limited, and/or the need of non-interchangeability prevailed on others requirements like efficiency and costs. According to the needs of the time, thermoelectric devices found direct implementation as coolers in those applications where accurate and precise temperature conditioning was of primary importance, such as optoelectronics, and in deep space missions as generators, where photovoltaic converters are not sufficient to power the on-board instrumentation of satellites and probes. In particular, the latter were designed in such a way that the heat source was provided by the decay of a suitable radioactive material and was converted into electricity by means of a thermopile. These engines, which were given the name of Radioisotope Thermoelectric Generators (RTGs) or, more commonly, nuclear batteries, were first developed in the late 1950s, in the Mound Laboratories in Miamisburg, Ohio, under contract with the United States Atomic Energy Commission (later Department of Energy) and under the guide of Bertram C. Blanke [30]. Subsequent generators realized for practical applications made use of a pellet of $^{238}PuO_2$ as heat source, whose radioactive decay, being of the alpha type, is relatively easy to shield. RTGs are capable of generating hundreds of watts with an appreciable diminution of the power output of only few percent points over a period of decades. The first RTG launched into space by the United States was SNAP 3 in 1961, aboard the Navy Transit 4 A spacecraft. Then, others were mounted on Pioneer 10, Pioneer 11, Voyager 1, Voyager 2, Galileo, Ulysses, Cassini, New Horizons and on the Mars Science Laboratory. RTGs were also used to power the two Viking landers, and for scientific experiments they have been left on the Moon surface by the crews of Apollo 12 through 17.

In the 1970s, the healthcare company Medtronic extended the use of thermoelectrics to the biomedical sector replacing the old Hg-Zn batteries implemented in cardiac peacemaker, which were suffering of high failure rates within few months of implantation, with small nuclear batteries. Despite the success of the technology, due to nuclear waste disposal issues, the nuclear thermopiles were abandoned in the late 1980s in favor of lithium batteries. No health issues regarding the human implantation of nuclear batteries has ever been demonstrated while, since their substitution with lithium batteries, patients had to update their peacemaker with invasive surgery approximately once a decade, thus lowering their life expectation, until the advent of wireless charging [31].

The second half of the XX century was characterized by the development of nanotechnology, and by the profound changes it brought along. In the 1990s, L. D. Hicks and Mildred Dresselhaus (Brooklyn, November 11, 1930 - Boston, February 20, 2017), both physicists at the Massachusetts Institute of Technology, published a couple of theoretical papers indicating that materials nanostructuration may offer significant advances in the thermoelectric properties of matter, giving new hope for materials with higher zT [34,35], and thus devices with higher conversion efficiency (see the panel “On the theory of thermoelectric transport in the solid state”). It would take few years before such improvements were shown experimentally [36,37], and more than a decade before they were incorporated into working systems [38]. However, together with the introduction of the *material quality factor* long before, which subsequently evolved into Slack’s *phonon-glass electron-crystal* concept [39] that phonons should be disrupted like in a glass but electrons should have high mobility as in crystalline semiconductors, this concept renewed the interest in the thermoelectric technology and culminated in the search for new complex and/or nanostructured materials, and the re-consideration of the thermoelectric technology for everyday life applications. This was happening at the doors of the XXI century.

Today, the increasing attention to the worldwide energy issues and the recognized need of pursuing a sustainable society to assure prosperity and health to the next generations [40], has moved the attention of the scientific community to the problem of energy efficiency and sustainability. While thermoelectric generators based on state-of-the-art materials remain far from being competitive with more conventional engines (see Fig. 4) [41,42], when used in combination with other primary engines they provide a way to partially recover the waste heat and thus increase the overall efficiency of the engine. In this context, the thermoelectric technology has been recognized as a potential asset for direct thermal-to-electrical energy conversion in a variety of processes affected by significant energy losses in the form of waste heat, such as those involved in power plants and factories. Thermoelectric generation has been widely considered also for the automotive sector. However, with the new generation of cars based on *cold* electric engine slowly replacing current car models based on ignition- and combustion-engines [43], the interest in this sector is slowly decreasing. Nevertheless, the transition to electric cars will take no less than a couple of decades, and meanwhile the automotive companies will have to pay the

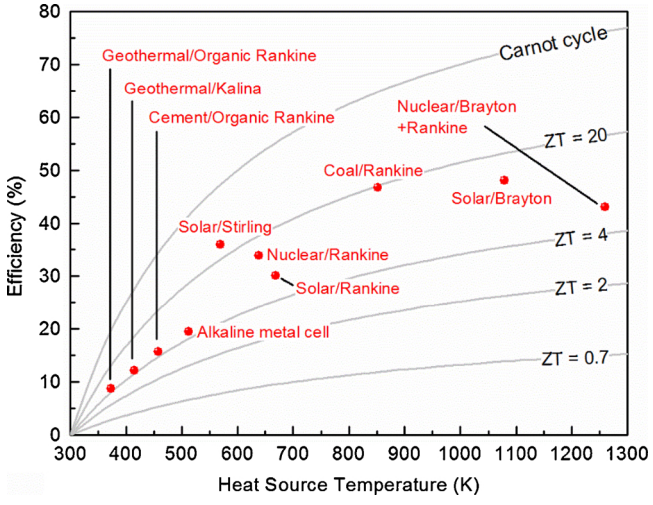

Fig. 4. Comparison between the efficiency of conventional engines and the efficiency of thermoelectric generators reported as a function of ZT (Data reproduced from Refs. [41] and [42]).

European Union for the emission of each additional gram of CO_2 above a certain established value that decreases every three or four years [44,45]. Therefore, the automotive companies have, and will have for a relatively long period, interest in all those technological solutions, including thermoelectrics, that can help to reduce CO_2 emissions and that have cost per gram smaller than the fee they have to pay to the European Union because of the emissions.

On the other hand, unlike conventional engines, thermoelectric devices are scalable, and scalability allows for the design of micro generators that can exploit local and small temperature differences to power distributed low power electronics. Considering the recent advances in the electronics sector, which have enabled modification of the size and shape of the electronic components down to the microscale, with commensurate scaling of their power requirements to mW and μW ranges, many complex electronic systems, such as networks of wireless sensors and actuators, are now operated on batteries. While a small fraction of these systems are already equipped with local generators exploiting renewable energy sources, like small photovoltaic panels, thermoelectric generators could provide a complementary, or alternative, source of energy wherever other forms of generation alone cannot fulfill the requirements. Therefore, in this framework, thermoelectric conversion is currently investigated to help overcoming the actual need of replacing or periodically recharging the batteries of low energy devices, thus providing additional assets towards the practical realization of smart grids. To the purpose of serving devices having small dimensions and operating at room temperature, special microthermoelectric generators (μTEGs) have been designed and fabricated, and are currently intensive object of research. State of the art μTEGs made of Bi_2Te_3-based thermocouples are capable of generating few mW cm^{-2} under a temperature difference of few degrees [46,47].

Newer technological opportunities come from the recent development of organic, carbon-based electronics, which has opened a world of applications for flexible, stretchable, and even biocompatible materials. In this context, a novel class of thermoelectric generators, based on innovative architectures and cost-effective solution processing, are now an active field of research for room-temperature flexible applications to be used for distributed electronics and integration into wearables [48,49]. As solution processing can enable high-throughput mass printing fabrication, research is not limited to organics in this context, but invests also inorganics and hybrid materials suitably dispersed in stable formulations, with the aim of lowering the final costs of generators.

With the increasing number of potential fields of applicability, thermoelectrics is now facing its major challenge: developing higher-performance, non-toxic and sustainable thermoelectric materials, in order for the technology to go green and be practically implemented. Materials currently used to build commercial devices, such as tellurium, lead and germanium, are rare and/or toxic, and thus they can hardly be considered for mass production (see Fig. 5). To overcome this obstacle, the scientific community has been working, since the second half of the XX century, on a series of different compounds, including silicides, chalcogenides, skutterudites, oxides, clathrates, Heusler, Zintl phases, and more recently organics, each more or less suited to specific working environments and temperature intervals. The conventional optimization of the thermoelectric properties of materials is generally pursued adopting two strategies: the optimization of the charge carrier density and the minimization of the lattice thermal conductivity [17]. While the former is about finding the best compromise between the power factor $\sigma\alpha^2$ and the electronic contribution to the thermal conductivity, the latter consists in increasing the scattering of phonons by adopting complex crystal structures having cages occupied by rattling atoms, or by inducing point defects such as interstitials and vacancies, by alloying, and/or by adopting multiphase composites mixed on the nanometer scale [17,38]. In particular, complex structures were addressed as a potential pathway towards the phonon-glass electron-crystal model, allowing to simultaneously tune the charge carrier density and provide effective scattering centers for phonons [50]. In parallel, engineers and material scientists are developing techniques and device architectures that allows to exploit the thermoelectric materials in the temperature intervals where their figure of merit is maximized. These include cascade and segmented thermoelectric devices. Cascade devices are multiple-stage thermoelectric generators assembled in thermal

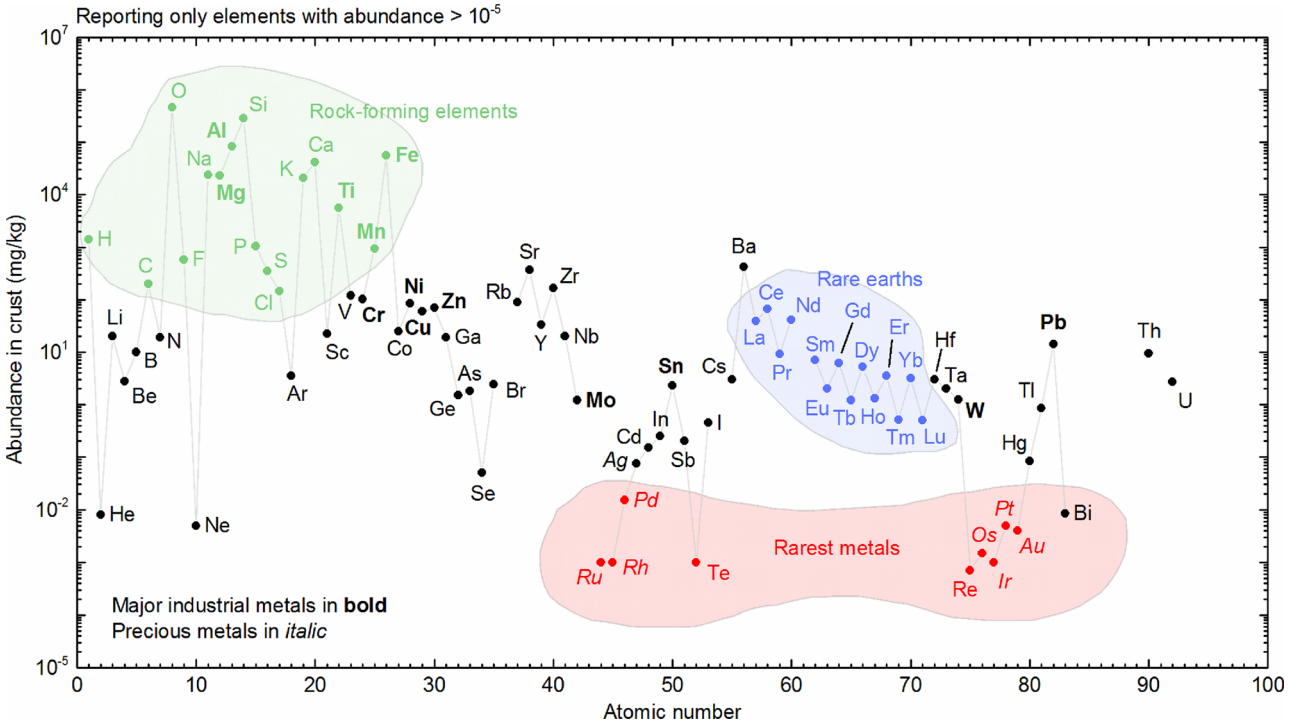

Fig. 5. Chart of the abundance of the chemical elements in Earth's crust. Data elaborated from Refs. [54] and [55]. Bismuth is often excluded from the rarest metals group, possibly due to its higher abundance compared to tellurium. However, according to Ref. [54], both of them should be considered very rare metals.

series, with the stage having higher ZT at higher temperatures facing the hot side, and where each stage contains an independent electric circuit. Segmented devices are single-stage generators where the thermocouples legs are realized by arranging different thermoelectric materials on top of each other in both thermal and electrical series, and where heat is applied to the side close to the thermoelectric materials having higher zT at higher temperatures [51,52]. In the light of understanding the thermodynamics behind segmented devices, Gerald Jeffrey Snyder has recently introduced the thermoelectric compatibility factor

$$s = \frac{\sqrt{1 + zT} - 1}{\alpha T}$$

which is the value that the intensive reduced current $u = J/\kappa\nabla T$ must achieve to maximize the contribution given by each thermoelectric material segment to the conversion efficiency of the generator [51,53]. It was shown that in order for segmented generators to have conversion efficiencies higher than non-segmented generators made of the same materials, it is not sufficient to simply maximize zT of each segment: the compatibility factor of the materials used to build the segmented thermocouples legs also need to be similar.

As the technology is making its own room in the market of everyday applications, device engineers are now facing the costs challenges: μTEGs are required to be battery competitive, TEGs designed for the automotive sectors must be characterized by a cost per gram lower than the fees that the automotive companies have to pay for each gram of CO_2 emitted by their cars, and TEGs designed for waste heat recovery in industrial process have to reach payback time in a reasonably competitive timeframe. It has been recently assessed that materials costs represent only a small fraction of the overall cost of thermoelectric devices, and that design optimization with respect to the cost to performance ratio leads to different device architectures with respect to those required to optimize the power output or the efficiency alone [56]. This result demonstrates potential for the thermoelectric market to diversify its product, hence opening the doors to a world of opportunity that so far has been only partially explored.

1.1. Panel. On the theory of thermoelectric transport in the solid state

Nanostructuring techniques and tuning the complex crystal structure of materials allows to achieve i) extremely low κ compared to those of their corresponding bulk material, and to ii) improve the *PF* by increasing σ and α independently, relaxing their adverse interdependence to some extent. This panel describes the usual theoretical approaches employed to extract the thermoelectric properties of complex materials and nanostructures.

1.2. Complex bulk materials

A large number of new materials with complex crystal structures, including clathrates, skutterudites and half-heuslers, to name a few, have recently been the subject of intense study from the experimental and theoretical point of view. Their complex bandstructures and phonon spectra provide possibilities to achieve high *PF* by decoupling σ and α, especially near their band edges, while keeping low κ [57,58], and to manipulate the nature of phonon scattering [59–62]. A variety of techniques have been considered and adopted so far. On the one hand, bands alignment at band edges [63], the introduction of resonant states by alloying [64], doping, vacancies and lattice imperfections, are exploited to directly tune the bandstructures, with the ultimate goal to increase the *PF*. On the other hand, strain field and mass fluctuations due to disorder at the atomic scale, higher mass difference and a lattice mismatch between imperfections and lattice, the introduction of second-phases, [65] and alloying [66], significantly increase the scattering of short- and medium- phonon mean-free-paths ($\sim < 100$ nm), ultimately leading to lower κ [67]. Phonons with long mean-free- paths (0.1–1 μm) are usually manipulated by mesoscale features such as grain boundaries [67].

The complexity of their bandstructure, phonon spectra, and transport properties, make it essential for involved computational studies to understand, and improve, their thermoelectric properties. These are typically calculated by solving semi- classical electron and phonon Boltzmann Transport Equations (BTE) using calculated electron and phonon dispersion relations. In calculating the electronic dispersions, semi-empirical tight-binding methods [68] and *ab initio* density functional theory (DFT) based methods [59,60,69–71] are commonly used, while more computationally demanding many-body perturbation methods, such as the GW approximation [72,73] are employed when higher accuracy is required. Phonon spectra, on the other hand, are often obtained by analyzing the forces associated with a systematic set of atomic displacements using the finite displacement method (FDM) [74,75]. Alternative approaches include density functional perturbation theory (DFPT) [76,77], where direct calculation of second order derivatives of the energy provide inter-atomic force constants. Albeit less accurate than first principles approaches, Molecular Dynamics (MD) can also be used to extract phonon dispersions [78] and other phonon transport properties [79].

To extract the transport properties σ, α and κ_{ph}, the semi-classical electron and phonon BTE is typically solved under the relaxation time approximation, in conjunction with rigid band and constant electron relaxation time approximation. However, recent progress in linear scaling DFT software [80,81] has enabled DFT calculations on large systems, thus allowing the generation of more accurate band structures for highly doped structures, beyond the rigid band approximation. Other sophisticated recent approaches use *ab initio* extracted electron-phonon scattering Wannier method (*EPW*) [82], which allows electronic transport considerations beyond the simplified constant relaxation time approximation and beyond deformation potential theory. Similarly, when it comes to phonon transport, molecular dynamics approaches [83] that can treat anharmonicity to all orders, or techniques that involve the exact solution of the BTE, go beyond the phonon-phonon relaxation time approximation [84,85].

As high substitutability of the lattice sites in complex crystal structures, as well as targeted alloying, provide many opportunities for tuning electronic and lattice properties, high throughput screening methods have recently been advanced to screen best compound combinations [86,87]. High throughput screening [87,88] for DFT calculated material properties is often combined with machine learning techniques [86,87] to accelerate the discovery of promising thermoelectric materials in terms of the power factor, thermal conductance and thermal, mechanical, and chemical stability. The ability to decouple σ and α is also used as an additional efficient measure for screening [89,90].

1.3. Nanostructures and nanostructured bulk materials

The initial motivation for nanostructures for thermoelectric materials originated from the theoretical suggestion of Hicks and Dresselhaus, who indicated that channels of lower dimensionality can potentially improve α [34]. The sharp features in the low- dimensional density of states DOS(E) function can improve α, as this quantity is proportional to the energy derivative of DOS(E). Mahan and Sofo have further shown analytically that thermoelectric energy conversion through a single energy level (zero-dimensional channel) can reach the Carnot efficiency when the lattice part of the thermal conductivity is zero [91]. Despite the initial excitement, however, in practice these approaches failed to achieve power factor improvements. Involved calculations for the power factor in 0D single level systems [92], 1D nanowires [93], and 2D ultra-thin layers in various orientations [94], and matrix materials with embedded nanoinclusions (see Fig. 6) [95], including all scattering mechanisms (electron-phonon scattering, surface roughness scattering, and ionized impurity scattering) and all

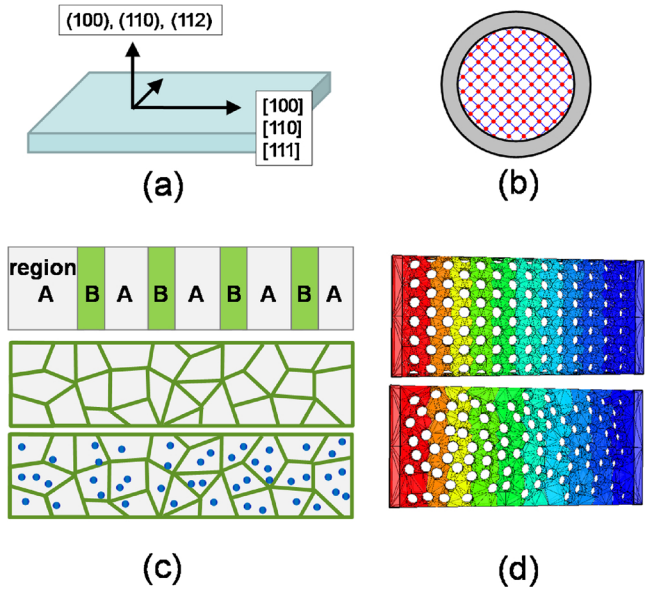

Fig. 6. Schematic examples of low-dimensional and nanostructured materials: (a) Ultra-thin Si layers of various transport and confinement orientations. (b) Ultra-narrow Si nanowire described on the atomistic lattice. (c) Nanostructured bulk materials – superlattice, nanocrystalline material, nanocrystalline material with hierarchical nanoinclusions. (d) Nanomeshes (nanoporous material) with a temperature gradient indicated (red for hot, blue for cold) (for interpretation of the references to colour in this figure legend, the reader is referred to the web version of this article).

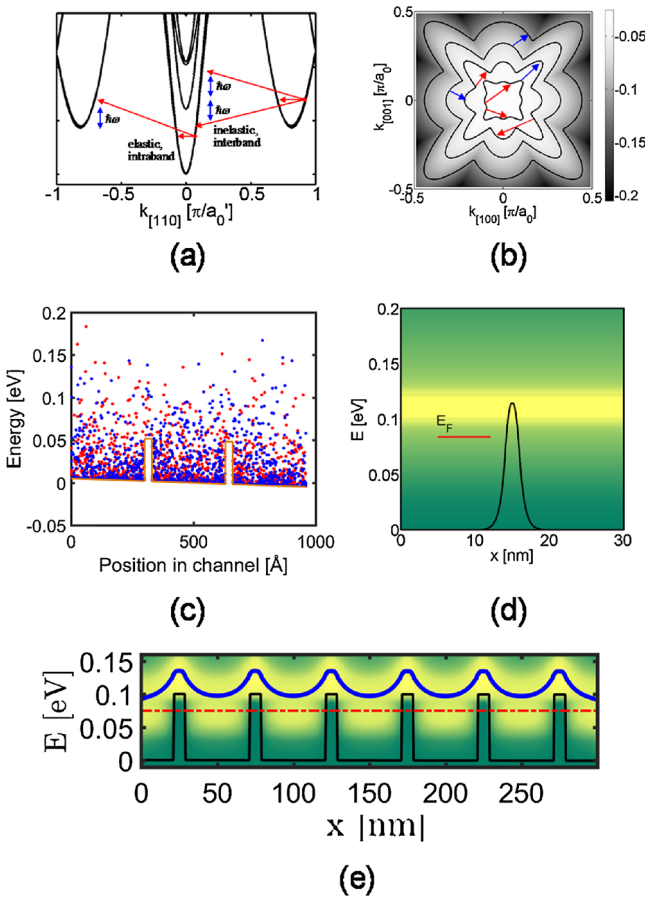

Fig. 7. Electrothermal transport methods and important effects: (a) A Si nanowire bandstructure indicating elastic/inelastic, and intra/inter-valley scattering mechanisms used within the BTE formalism. (b) A *p*-type Si ultra-thin-layer bandstructure indicating scattering mechanisms as in (a). (c) Electron distribution in a Monte Carlo simulation in a superlattice channel. Red/blue indicates right/left going electrons. (d) Electron transport demonstrating quantum tunneling (yellow color) through a potential barrier using the NEGF formalism. (e) The average energy of the current flow (blue line) through the potential barriers of a superlattice (red potential barriers). Semi-energy relaxation can be observed in the potential wells. The red-dashed line indicates the Fermi level for that simulation example (for interpretation of the references to colour in this figure legend, the reader is referred to the web version of this article).

relevant subbands [93,96], have been performed over the last several years. These have indicated that although α can be increased in such systems, σ is degraded severely, such that improvements in *PF* are difficult to be achieved.

More elaborate simulation studies in nanocomposite materials, however, have identified some ways in which power factor improvements can be achieved, which involves energy filtering through the use of potential barriers, semi-relaxation of the carriers' energy in specific regions of the material, variations in the thermal conductivity in different regions of the material, as well as non-uniform distribution of the dopant atoms [97–100]. The latter relates to one of the modulation doping techniques, which allow for high mobility carriers in regions away from high dopant scatterer concentrations.

On the other hand, where the low-dimensional and nanostructured strategy has paid off, is in the remarkable reduction of κ. Phonons in solids have mean-free-paths that are distributed in energy over orders of magnitude, from nm to μm, even mm, with average (over energy) phonon mean-free- path much larger than that of the charge carriers. In Silicon, for example, the average phonon-mean-free path is reported to be a few hundreds nm, whereas the electron/hole mean-free-path is in the order of few nm, up to tens of nm [101,102]. The introduction of surfaces, atomistic and nanoscale defects, and grain boundaries, scatter phonons of different wavelengths (frequencies and mean-free-paths), such that phonon transport is impeded across the spectrum and κ is drastically reduced, in many cases even below the amorphous limit [67,103,104].

1.4. Transport regimes and methods

Understanding and computing thermoelectric properties in nanostructures and nanostructured bulk materials mixes different transport regimes, from diffusive to semi-ballistic, and from incoherent to fully coherent. In addition, narrow channels such as nanowires and ultra-thin layers undergo significant quantum confinement that alters their bandstructures. From the theoretical point of view, these transport regimes are treated on a similar manner for electrons and phonons, with the main difference that they have very different mean-free-paths.

Even in large scale, bulk-sized materials, embedded nanostructuring changes the transport properties locally by introducing resonances, semi- ballistic transport and quantum interferences in some regions of the material, whereas diffusive transport can dominate in other regions. Typical schemes of nanostructured bulk materials are shown in Fig. 6c. The regular placement of the boundaries could provide resonances, and non-equilibrium transport features can emerge. Carriers relax their energy in the potential well within a specific energy relaxation length, after overpassing the boundary potential barriers, resulting in a partial energy relaxation transport, depending on the size of the grains (see Fig. 7e). The situation is somewhat more complicated in hierarchically disordered structures, where embedded nanoinclusions or voids exist in addition to nanograin boundaries [103,105]. Geometrical details now become even more important in mixing ballistic and diffusive regimes and determining transport.

When it comes to phonon transport, nanostructured material regions that are diffusive for a specific group of phonons can be semi-ballistic or essentially fully ballistic for some of the long wavelength

phonons, and can be affected in a different manner by different disorder features.

Therefore, it is essential that geometrical details are accurately captured, as well as the wave and particle nature of the transport carriers, which interacts differently under different circumstances and leads to different transport properties. In addition, significant quantum confinement alters the bandstructure of low-dimensional regions, which dictates the utilization of atomistic full-band description of materials within the transport formalisms. In general, however, for material feature sizes down to 30 nm, continuum formalisms, with reasonable adjustments from bandstructure information, provide adequate insight into experimental measurements [93].

Here below, the main techniques used to investigate transport are briefly discussed separately.

- The *Boltzmann Transport Equation* (BTE) is frequently solved in the relaxation time approximation in the linear response regime, either with constant or energy dependent relaxation times. It has experienced considerable success in interpreting experimental data by introducing simplified scattering rates from complex geometrical features for both electrons and phonons. This treats transport in the fully diffusive, semi-classical regime, does not capture the geometrical features in detail, but can incorporate full-bandstructure information. Within the Linearized Boltzmann formalism, the σ, α, and κ_{el} are defined as [91,93,106–108]:

$$\sigma = {q_0}^2 \int_{E_0}^{\infty} dE \left(-\frac{\partial f_0}{\partial E}\right) \Xi(E)$$

$$\alpha = \frac{q_0 k_B}{\sigma} \int_{E_0}^{\infty} dE \left(-\frac{\partial f_0}{\partial E}\right) \Xi(E) \left(\frac{E - E_F}{k_B T}\right)$$

$$\kappa_0 = {k_B}^2 T \int_{E_0}^{\infty} dE \left(-\frac{\partial f_0}{\partial E}\right) \Xi(E) \left(\frac{E - E_F}{k_B T}\right)^2$$

$$\kappa_e = \kappa_0 - T\sigma\alpha^2$$

here $\Xi(E)$ is the so- called transport distribution function, defined as:

$$\Xi(E) = \sum_{k,n} v_{k,n}^2(E)\tau_{k,n}(E)g_{k,n}(E)$$

where $v_{k,n}(E)$ is the bandstructure velocity, $\tau_{k,n}(E)$ is the momentum relaxation time, and $g_{k,n}(E)$ is the density of states for a state in a specific k-point and subband n. All material related properties are contained in this function, including all atomistic and confinement effects for low-dimensional 1D/2D channels as indicated in Fig. 7a–b. Electronic state transitions (intra- or inter-band) due to scattering can be numerically accounted for upon different scattering mechanisms as indicated by the arrows in Fig. 7a–b. Numerically extracted bandstructures from density functional theory (DFT), tight-binding, or even continuum methods are routinely used within the BTE formalism in the relaxation time approximation. One can easily observe from the previous equations that σ is determined by energies around the Fermi level, whereas α, being weighted by the energy, is determined by somewhat higher energies. The fact that α is weighted by energies higher than the Fermi level, has driven large efforts in identifying materials in which the density of states increases around the Fermi level. This leads to the tremendous effort in studying low-dimensional materials which have very sharp increases in their DOS (step-function for 2D subbands, van Hove singularities for 1D subbands).

It is useful to examine here a few usually encountered cases for the energy resolved shape of $\Xi(E)$ and its effect on the thermoelectric coefficients. Under the simple acoustic phonon limited scattering conditions, it holds that $\tau_{k,n}(E) \propto 1/g_{k,n}(E)$, in which case $\Xi(E) \propto E$ as $v_{k,n}(E) \propto \sqrt{E}$, for subbands of any dimensionality. In the case of the constant relaxation time approximation, $\tau_{k,n}(E) \propto C$, the $\Xi(E) \propto EE^{d/2-1} = E^{d/2}$ where d is the dimensionality of the channel, indicating that away from the energy regions that have sharp features in their DOS, a 3D bandstructure will benefit the Seebeck coefficient more. In more general terms, the transport distribution function can be written as $\Xi(E) \propto E^{d/2+r}$, where r is a characteristic exponent of the energy dependence of the relaxation time. Again, as r increases, as in the case of ionized impurity scattering dominated transport, for example, the Seebeck coefficient increases as well. When various scattering mechanisms are involved in transport, the Matthiessen's rule is used to combine them [109]. Specifically for nanostructures, the bulk material scattering mechanisms (electron-phonon, electron-impurity, electron-alloy), are combined with scattering events on boundaries and defects. The latter are usually treated in a simple manner, where the scattering times are given by the ratio of geometrical features to the group velocities. However, for nanostructured materials with high degree of disorder and geometrical complexity, simple expressions for the scattering times of electrons or phonons on boundaries and defects lose predictive power, and more advanced methods are needed, such as the Monte Carlo method that is briefly described below.

- The use of *Monte Carlo* techniques solve the semi-classical BTE in a statistical manner by simulating particle trajectories in an arbitrary nanostructured domain and can capture geometrical details [110–113] (see Fig. 7c, where red/blue dots represent right/left going particles crossing potential barriers). In this method the energetics of particles are initialized at the channel contacts and/or in the channel according to information from their specific bandstructures and are allowed to move in the simulation domain. Their trajectories interchange between free flight and scattering events, either from intrinsic scattering (i.e. electron-phonon, phonon-phonon scattering), or specifically in the case of nanostructures scattering resulting from collisions with boundaries, defects, embedded nanoinclusions, etc. Thus, this method can, in general, very accurately capture the transport properties of nanomeshes and nanocrystalline structures of high degree of disorder (as shown in Fig. 6c–d). Usually comparison to experimental data is performed after adjusting the boundary scattering strength through simple wavevector dependent equations with a few parameters that describe the nature of these boundaries such as the roughness strength. Both electronic transport and phonon transport can be treated, although for thermoelectric studies Monte Carlo is mostly used for phonon transport [110–113]. Quantitatively, once the simulations are initially calibrated to the bulk values, the influence of nanostructuring is then examined by altering the geometry details accordingly (see Fig. 6).

- The *Non-Equilibrium Green's Function* (NEGF) method is a more advanced, fully quantum mechanical method, that accounts for effects such as subband quantization, tunneling, resonances, and quantum interferences (see Fig. 7d), as well as all geometrical complexities (see Figs. 6 and 7c). It can incorporate electron-phonon scattering, and it can capture transport from fully coherent (ballistic) to fully incoherent (diffusive) regimes. It has been employed in the past for both electrons and phonons, and it is ideal for treating transport in nanostructures which intermix different transport regimes and contain features in the order of the electronic/phononic wavelength (and mean-free-path). However, it becomes computationally expensive as the size of the structures extends beyond several tens of nanometers. NEGF can also be combined with atomistic bandstructures, but this further increases computational costs and limits the size of the computational domain.

NEGF method solves the Schrodinger equation for an open system in which electrons can enter/exit the material channel through open, semi-infinite long contacts. Under a bias voltage or a temperature gradient applied to those say left/right contacts, the charge current, conductance, and Seebeck coefficient can be calculated. Within the NEGF formalism, the retarded Green's function is given by:

$$G(E) = \frac{1}{(E + i0^+)I - H - \Sigma_1 - \Sigma_2 - \Sigma_{scatt}}$$

where H is the Hamiltonian of the channel material, $\Sigma_{1/2}$ represents the semi-infinite contacts to the left and right of the channel, Σ_{scatt} is the self-energy for scattering, which allows the incorporation of electron-

phonon scattering in the formalism, and an infinitesimal positive value, $[i0^+]$, is added to the energy to push the poles of G to the lower half plane of the complex energy. The current in the material is computed self- consistently from specific elements of the Green's function and the Hamiltonian [114,115]. The formalism is also applicable for phonon transport, but in that case the Hamiltonian matrix is replaced by the Dynamic matrix (which contains all relevant information about the phononic properties of the material system). Due to its computational complexity it is often used in the ballistic/coherent transport, i.e. $\Sigma_{scatt} = 0$. Recently, however, acoustic and optical phonon scattering has been included within the NEGF formalism ($\Sigma_{scatt} \neq 0$) in thermoelectric power factor studies in 1D and 2D superlattices and materials with embedded nanoinclusions [92,98]. NEGF provides a more complete picture of the influence of nanostructuring on the thermoelectric properties since it is very flexible in describing geometrical details and quantum mechanical effects (such as tunneling – Fig. 7d), and possibilities that allow for performance improvements can be identified without strong approximations in the calculation [95,98]. Computation-wise, on the other hand, both deviating from purely 1D channels, and including phonon scattering, add a large numerical complexity. All self-energies become quantities that can only be solved iteratively (contact self-energies) and self-consistently (scattering self-energies), which requires numerical convergence, but progress is steadily being made.

- *Molecular Dynamics* can also capture phonon transport in nanostructured materials at the atomistic level, including anharmonic effects. MD has been extensively used in understanding the role of surfaces, boundaries, disorder, discontinuities, and interfaces in nanostructures and superlattices, cases where the thermal conductivity drops below the amorphous limit. MD calculations of thermal conductivity can require domains with thousands of atoms and long simulation times (in the order of nanoseconds) [116,117] that are not computationally affordable with first principles methods. When studying bulk materials properties, MD employs the use of periodic boundary conditions [118–120]. However, when it comes to materials with extended nanostructuring, it is only computationally convenient when the important features and dimensions of the material under investigation are within a few nm. For this reason, MD is used for nanowires, or thin layer structures of at most up to a few hundreds of nm in length [117,121].

In classical MD the total forces on all atoms are computed and used to solve Newton's equations of motion to determine how the atoms evolve. This is done iteratively, using a numerical scheme, such as *Verlet* or *leapfrog*. In a classical simulation, the forces between the atoms are defined by an interatomic potential. Choosing the best available potential and understanding its limitations is therefore crucial. Interatomic potentials are generally based on simple functional forms with adjustable parameters, but can have varying degrees of complexity. The problem of accurately mimicking true energy surfaces is far from trivial, and the parameters are often chosen such that the empirical potential matches results obtained with first principles calculations or experimental data [122]. Potentials vary in terms of the nature of the bonding described (covalent, polar covalent, ionic, metallic, hydrogen, van der Waals), whether short- and/or long-range interactions are considered, and the number of atoms that interact with each other (pair potentials versus many-body potentials) [122,123]. The use of classical potentials confers MD the advantage of naturally including anharmonic effects (through the form of the potential). This in turn makes classical MD suitable to model systems at non-zero temperature, when anharmonic effects become relevant and higher theoretical approaches become more cumbersome.

The effect of imperfections in lowering the mean free path of materials is more noticeable at low to medium temperatures. Phonon-phonon scattering is weak in this regime and defect scattering plays a more significant role [124]. However, strictly speaking, classical molecular dynamics is only applicable to solids above the Debye temperature, below which quantum effects are more relevant.

Thermal transport in MD, and related quantities (such as phonon relaxation times and velocities), are generally obtained by computing thermal conductivity using one of two major approaches: (1) equilibrium, via the Green–Kubo formalism [125,126], and (2) non- equilibrium or direct methods, such as the Müller-Plathe [127]. Each has advantages and disadvantages, and the method chosen strongly depends on the problem of interest [120]. In general, the equilibrium approach is preferable for bulk phase simulations and the direct method is best for finite structures [120]. Direct methods rely on disturbing a system and measuring its response, while in the equilibrium MD approach the response is computed from the averaging of small, local deviations from equilibrium that occur in the simulation time domain.

2. Inorganic materials

2.1. Metal chalcogenides

Metal chalcogenides are an important class of materials that have rich compositional diversity and can adopt a wide variety of structures, and for this reason, span a broad range of chemical and physical properties. These compounds contain one or more chalcogen atoms (S, Se, Te) and are less ionic than their metal oxide cousins, which affords them with smaller band gaps that are well suited for thermoelectrics. In particular, the chalcogenides of the p-block metals (Bi, Pb, Sn, etc.) are perhaps the most studied systems for thermoelectric cooling and power generation. These materials have intrinsically low thermal conductivity and electronic properties that can be fine-tuned for applications across a wide range of temperatures [50,128–130]. For example, Bi_2Te_3 and its alloys are the best materials for low- temperature cooling and have been used commercially since the 1950's [27,131,132]. Heavily doped PbTe is effective for mid-temperature (600–800 K) power generation and have been exploited in RTG for several decades [133,134]. For applications beyond 1000 K, rare-earth chalcogenides are among the best due to their high thermal stability [134], and $La_{3-x}Te_4$ can deliver a zT value of approximately 1.2 at 1300 K [135,136]. More recently, a new generation of binary and ternary chalcogenides with complex structures and ultralow κ, which offers a new perspective on designing high performance thermoelectric materials, has emerged. In 2014, SnSe was shown to have an unprecedented zT of 2.6 at 923 K in single crystal samples, which is attributed to its structural anisotropy and ultralow κ_{ph} [137]. Similarly, numerous ternary chalcogenide systems with complex structures and ultralow κ have been reported, many of which have zT values exceeding 1.0, including $CsAg_5Te_3$ [138], $AgBi_3S_5$ [139], and $K_2Bi_8Se_{13}$ [140].

This section gives a brief overview of the importance of metal chalcogenides in thermoelectrics. To better handle this vast topic, the section is mostly focused on the key structure-types and chemical compositions that have received the most attention. Specifically, the important advances related to bismuth chalcogenides, lead chalcogenides, tin selenide, binary copper chalcogenides, and complex ternary chalcogenides that exhibit ultralow κ, are addressed. More comprehensive reviews on these topics can be found elsewhere [129,141–143].

2.1.1. Bismuth chalcogenides

Bismuth telluride and its alloys, most notably $Bi_{2-x}Sb_xTe_3$ (p- type) and $Bi_2Te_{3-x}Se_x$ (n-type), have been used in thermoelectric cooling applications for several decades [132,144,145]. Bi_2Te_3 itself was first discovered in 1815 in Telemark, Norway, and its mineral form is tellurobismuthite [146]. Bi_2Te_3, Sb_2Te_3, and Bi_2Se_3 adopt the tetradymite structure, which is in the rhombohedral crystal system with the $R\bar{3}m$ space group. Bi_2Te_3 has an indirect band gap of approximately 0.15 eV and the electronic structure is such that the valence band maximum and conduction band minimum have 6 valleys in the mirror plane of the Brillouin zone [147–149]. This material is often described as having a distorted rocksalt structure with Te(1)-Bi-Te(2)-Bi-Te(1) layers that are

held together via Van der Waals interactions. The layered motif results in highly anisotropic properties, and studies have shown that the best performance is measured along the direction perpendicular to the c-axis [17]. It should be mentioned that bismuth and tellurium are in low abundance in the earth's crust, with tellurium falling under the category of the rarest elements (see Fig. 5) [150].

Bismuth telluride and its alloys have relatively low melting points, which allows these materials to be synthesized by melting the constituent elements in sealed quartz tubes. Single crystal samples are typically generated using the Bridgman method, where reaction tubes are slowly lowered out of a furnace to allow for controlled nucleation and growth of crystals [132]. More sophisticated zone melting techniques can be used to improve chemical homogeneity and also align grains within the ingot. Although single crystals are often preferred for device fabrication, polycrystalline samples are not uncommon and can be generated by sintering powders into dense pellets. Sintering can be achieved using a variety of techniques, and such processes typically yield samples with significantly improved mechanical properties [151]. Due to the low melting point and small band gap of bismuth chalcogenides, these materials are typically limited to low temperature applications.

The first study of the thermoelectric properties of Bi_2Te_3 was reported by Goldsmid in 1954 [27]. In the following years, *p*-type $Bi_{2-x}Sb_xTe_3$ and *n*- type $Bi_2Te_{3-x}Se_x$ emerged as the best materials for cooling and low-temperature power generation and have an intrinsic zT value of approximately 1.0 at 300 K [142,152,153]. Surprisingly, there was only minimal progress made over the next several decades, and it was widely believed that the upper zT limit had been reached. However, in the last ten years, there have been remarkable advances due to an influx of new ideas for engineering materials with low κ [154]. In 2008, Poudel et al. reported a method for generating $Bi_{0.5}Sb_{1.5}Te_3$ with a high density of grain boundaries, which was accomplished by hot pressing pre-synthesized nanopowders [155]. The resulting *nanobulk* material exhibited unusually low κ ($\sim$ 1.0 W m^{-1} K^{-1}) due to additional phonon scattering at the nanoscale grain boundaries, and displayed a zT of 1.4 at 373 K. Since this study, an array of bottom-up and top-down strategies for incorporating nanostructures into bulk materials have been investigated [156–160]. More recently, Kim et al. described a method for incorporating grain boundary dislocations into $Bi_{0.5}Sb_{1.5}Te_3$, and the authors reported a zT of 1.9 at 323 K [161], although this extraordinarily high value has not been confirmed by other groups.

Progress in *n*-type bismuth chalcogenides has been markedly slower, in large part because σ in these compounds is highly anisotropic. Notably, Zhao and coworkers reported a zT of 1.2 at 445 K for $Bi_2Te_{2.3}Se_{0.7}$ using a *point-defect engineering* strategy for lowering κ to less than 1.2 W m^{-1} K^{-1} at 450 K [162]. A variety of other *n*-type systems have been reported with good performance, which has been summarized well by Han [142]. As the field moves forward, it is critically important to develop new high-performance *n*-type materials to compliment the advances made in *p*-type systems.

2.1.2. Lead chalcogenides

In the 600–800 K temperature regime, heavily doped lead chalcogenides (PbTe, PbSe, PbS) are the leading materials for thermoelectric power generation [163–165]. PbTe was first discovered in 1845 as the rare mineral altaite [166], while the more abundant galena (PbS) has been the main source of Pb ore since ancient times. Lead chalcogenides adopt the rocksalt-type structure, which is in the cubic crystal system with the $Fm\bar{3}m$ space group, and have direct band gaps ranging from 0.27 to 0.41 eV. The valence band maximum and conduction band minimum are found at the L-point in the Brillouin zone and have 4-fold degeneracy [133]. Interestingly, the band gaps of these materials increase with temperature, which facilitates advantageous band convergence while also suppressing bipolar diffusion [167,168]. Although lead is considerably more abundant than bismuth, it is also more toxic, which may be a concern in future large-scale applications.

Since lead chalcogenides have cubic symmetry they exhibit minimal transport anisotropy, and for this reason, polycrystalline samples are often preferred. These materials are typically generated by melting the appropriate elements in sealed quartz tubes followed by sintering. Critically, sintered samples must exhibit good mechanical stability in order to withstand the thermal stresses found in working thermoelectric modules [132]. It has been observed that the brittleness of lead chalcogenides increases in the order PbTe > PbSe > PbS for both *p*-type and *n*-type samples [169,170]. The mechanical stability of PbTe can be improved by altering its microstructure using eutectic mixtures, for example PbTe-Si [171] and PbTe-Ge [172], since the incorporated precipitates prevent crack propagation.

Seebeck was the first to notice the high thermopower of PbS, more than a century before Ioffe's pioneering work describing the thermoelectric properties of lead chalcogenides [28,134,173,174]. At that time, there was not an accurate method for measuring κ at high temperatures, and consequently, zT for these materials was grossly underestimated until the arrival of the laser flash diffusivity method [133]. The intrinsic zT for optimized *n*- and *p*-type PbTe are now believed to be approximately 1.4 [175,176], and 1.2 for *n*- and *p*-type PbSe [177,178]. The performance of PbS is significantly lower due to higher κ and poor μ, although there is interest in these systems because sulfur is considerably cheaper than selenium and tellurium [165,177,179–181].

Similar to Bi_2Te_3, there has been significant progress in the performance of PbTe thermoelectrics in recent years, in large part due to advances in nanostructuring [182–184]. In 2004, Hsu found that *n*-type $AgPb_mSbTe_{2+m}$ (m = 10, 18), which adopts the rocksalt structure and is essentially a solid solution of PbTe and $AgSbTe_2$, exhibits a high zT of 1.7 at 700 K due to unusually low κ_{ph} [185]. High resolution transmission electron microscopy (HRTEM) analysis of these compounds revealed the presence of Ag/Sb-rich nanostructures, which are coherently embedded within the material and scatter mid-wavelength phonons. These strained, endotaxial precipitates form spontaneously during the cooling of the melt through spinodal decomposition and offer a useful technique for incorporating nanostructures into bulk materials. Similarly, *p*-type $NaPb_mSbTe_{2-m}$ (m = 20) was reported to have a zT of 1.6 at 675 K [186], which was attributed to low κ (as low as 0.85 W m^{-1} K^{-1}) facilitated by dense arrays of nanoprecipitates embedded within the material.

In addition to advances in nanostructuring, recent developments in band structure engineering have led to remarkable improvements in the electronic properties of lead chalcogenides. In 2008, Heremens et al. showed that Tl-doped PbTe (*p*-type) exhibits extraordinarily high thermopower due to the presence of resonant states at the Fermi level, yielding a zT of 1.5 at 773 K [64]. Similarly, Pei et al. showed that the energy offset between the valence band maximum (L-band) and the so-called heavy band (Σ-band) in *p*-type PbTe could be modified by alloying with Se, which increased the valley degeneracy from 4 to 16 at high temperatures [63]. Combined with a decrease in κ due to point defects, Na-doped $PbTe_{0.85}Se_{0.15}$ was shown to have a zT of 1.8 at 850 K. Such alloying strategies that modify the temperature of band convergence while also introducing point defects have been used to enhance the thermoelectric performance of numerous metal chalcogenides [187–189].

Perhaps the most impressive performance to date was observed in Na-doped $Pb_{1-x}Sr_xTe$, which was first reported by Biswas et al. in 2011 [190]. This material incorporates several important design features, including band convergence and all-scale hierarchical architectures (atomic scale disorder, nanoscale precipitates, mesoscale boundaries), which combine to give a zT of 2.2 at 915 K [67]. Furthermore, in a subsequent study, it was shown that non-equilibrium processing methods can be used to increase the amount of Sr dissolved in the PbTe matrix (greater than 5 mol%), which achieves better light hole/heavy hole band convergence and pushes the performance of this *p*-type material to zT = 2.5 at 923 K, a record for PbTe [191]. Such strategies,

which combine all-scale architectures along with enhanced electronic properties facilitated by chemical alloying, have become a new paradigm for designing high performance thermoelectric materials [143,192–196].

Progress in *n*-type PbTe has been slower than in state-of-the-art *p*-type materials, in large part because band convergence is inaccessible in these systems [173]. Nevertheless, there are now numerous reports of *n*-type PbTe materials with zT values greater than 1.5 [197,198]. For example, He and coworkers demonstrated a zT of 1.8 at 773 K in PbTe-4%InSb, which was accomplished by introducing *multiphase nanostructures* that dramatically reduce κ [199]. Moving forward, an important goal in the field is to develop high performance *n*-type materials to match the *p*-type systems described above. Additionally, new synthetic and processing methods that can deliver materials with greater mechanical stability are needed, since this is a common issue encountered during commercialization [132].

2.1.3. Tin selenide and copper selenide

Recently, SnSe has emerged as a new candidate for mid- temperature power generation, which is cheaper and less toxic than lead-based systems [141,200]. This material adopts the layered GeSe-type structure, which is in the orthorhombic crystal system and has the Pnma space group. SnSe has an indirect band gap of 0.86 eV and its electronic structure has multiple extrema in both the valence and conduction band [201,202]. Importantly, this material undergoes a reversible second-order phase transition (Cmcm space group) at approximately 750–800 K, and the accompanying change in volume makes it challenging to synthesize [141]. Due to highly anisotropic transport properties of SnSe, single crystals exhibit the best thermoelectric performance and are typically synthesized using the Bridgman method. SnS has also been explored for thermoelectric applications, but is reported to have significantly lower performance [203].

In 2014, Zhao et al. reported an unprecedented zT of 2.6 at 973 K along the b-axis in single crystal SnSe, and the extraordinary performance was attributed to ultralow κ (0.23 W $m^{-1} K^{-1}$ at 973 K) caused by highly anisotropic bonding (Fig. 10) [137]. Interestingly, the high-temperature phase transition produces a dramatic enhancement in *PF* due to an increase in band gap coupled with improved carrier mobility. In a subsequent study, the authors showed that the performance of SnSe at low temperatures could be dramatically improved by heavily doping the material with Na (*p*-type), which yielded an ultrahigh power factor of approximately 40 μW $cm^{-1} K^{-2}$ at 300 K, which rivals commercial $Bi_{2-x}Sb_xTe_3$ [204]. The device ZT in the temperature interval of 300–773 K was found to be approximately 1.34 for hole-doped SnSe, which is a new record. Since these groundbreaking studies, there have been numerous reports highlighting the exceptional thermoelectric performance of SnSe [205,206]. Notably, Duong et al. found that Bi-doped SnSe (*n*-type) shows a zT of 2.2 at 733 K along the b-axis of single crystals [207], while in 2018 Zhao et al. reported a zT of 2.7 at 773 K along the a-axis of Br-doped crystals, which is the current record for *n*-type SnSe [208].

More recently, there have been several reports highlighting the performance of polycrystalline SnSe samples [209–211], which are easier to synthesize and better suited for commercial applications. Interestingly, although polycrystalline materials typically exhibit lower κ than single crystals due to grain boundary scattering, this is not the case for SnSe, possibly owing to the very small mean free path of phonons in this compound [141]. Still, significant progress has been made in this area, and state-of-the-art polycrystalline SnSe samples with zT values greater than 1.0 are being reported with increasing frequency [206,212].

Similar to SnSe, $Cu_{2-x}Se$ and $Cu_{2-x}S$ are composed of earth abundant, nontoxic elements, and can display extraordinary thermoelectric performance when properly optimized [213–217]. Becquerel was the first to notice the high thermopower of copper chalcogenides while burning sulfur on top of Cu wires [143]. The first comprehensive studies of their thermoelectric properties were conducted by 3 M in 1960′s [218,219]. Interestingly, these studies suggested $Cu_{2-x}Se$ was not a viable candidate for thermoelectric applications due to the extremely high mobility of Cu ions when exposed to an electric field, which causes the material to decompose under working conditions. Nevertheless, there has been resurgent interest in this material due to its high

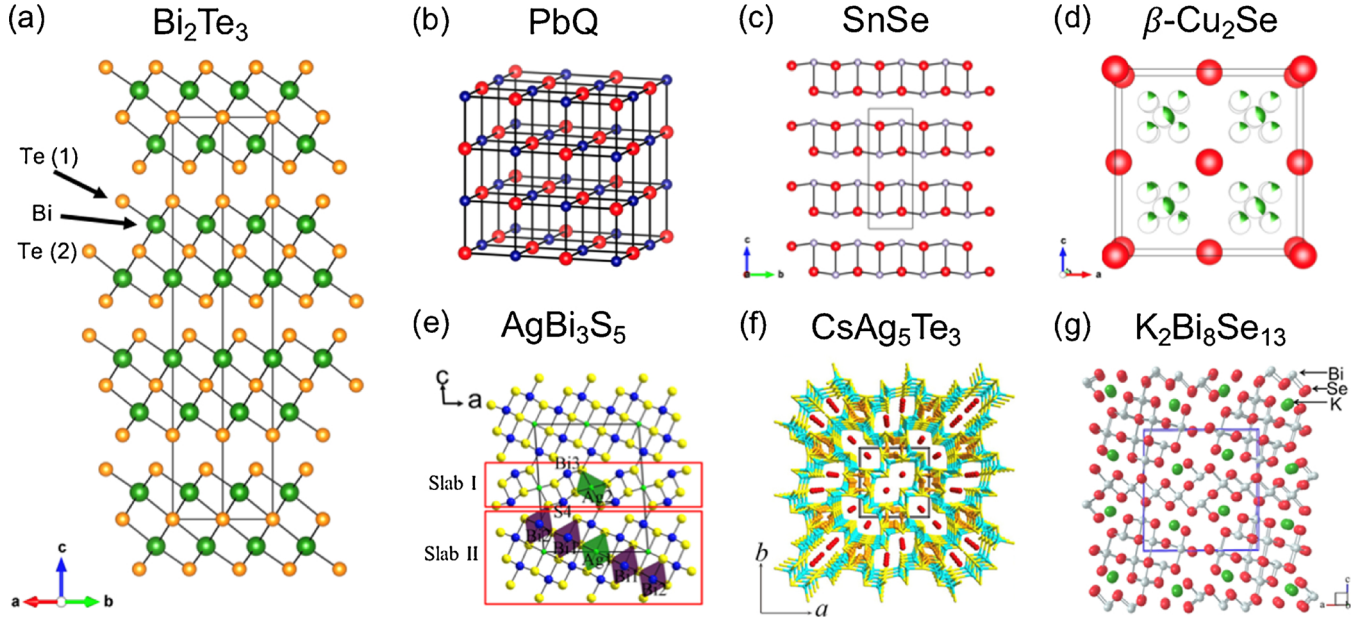

Fig. 8. Crystal structures of metal chalcogenides. (a) Bi_2Te_3 adopts the layered tetradymite structure while (b) PbQ (Q = S, Se, Te) is found in the cubic rocksalt structure. (c) Layered, orthorhombic SnSe viewed along the a-axis. (d) The high-temperature β-phase of Cu_2Se is cubic and has Cu atoms partially occupying various sites within the fcc Se sublattice. (e) $AgBi_3S_5$ adopts the complex pavonite-type structure. Adapted with permission from Ref. [14] Ref. [139]. Copyright 2017 American Chemical Society. (f) The tunnel- like structure of $CsAg_5Te_3$ facilitates Ag rattling modes and ultralow thermal conductivity. Adapted with permission fromRef. [13] Ref. [138]. Copyright 2016 WILEY-VCH Verlag GmbH & Co. KGaA, Weinheim. (g) $K_2Bi_8Se_{13}$ adopts a low-symmetry monoclinic phase. Adapted with permission fromRef. [15] Ref. [140]. Copyright 2016 American Chemical Society.

performance and low cost. $Cu_{2-x}Se$ has a complex structure that undergoes a phase transition at approximately 400 K, and the high temperature cubic β -phase is superionic with a *glass-like* phonon structure (Fig. 8d) that yields ultralow κ and a zT of 1.5 at 1000 K [220]. Poudeu and coworkers recently reported a remarkable zT of 2.6 at 850 K in $Cu_2Se/CuInSe_2$ nanocomposites [221], and the high performance was attributed to a combination of increased carrier mobility and decreased κ. The authors suggested that the nanostructured material is more stable than simple $Cu_{2-x}Se$. Importantly, such fundamental studies are providing insights into the thermal transport phenomena in fast ion conductors, although it is unclear whether these materials will ever be utilized in practical thermoelectric applications (Fig. 9).

2.1.4. Complex ternary chalcogenides

In the last two decades, an array of new ternary chalcogenides with complex structures and low κ have emerged in the thermoelectrics literature [222–226]. The importance of solid state chemistry in designing and selecting such compounds has been discussed [227]. In general, these compounds have large unit cells and low κ, and their chemical versatility allows them to be optimized across a range of temperatures. In 2000, Chung et al. described the thermoelectric properties of $CsBi_4Te_6$, which is compositionally similar to Bi_2Te_3 but has a distinct structure [228]. This narrow band gap semiconductor was shown to have a zT of 0.8 at 225 K (higher than $Bi_{2-x}Sb_xTe_3$) when properly hole-doped, which remains a record in the 150–275 K temperature regime. Recently, $AgBi_3S_5$, which is a member of the pavonite family (Fig. 8e), was demonstrated to have a zT of approximately 1.0 at 800 K when appropriately *n*-type doped with Cl [139]. The high performance is attributed to ultralow κ_{ph} (less than 0.4 W m^{-1} K^{-1} at 800 K) caused by *double rattling* phonon modes of Ag and Bi atoms. Similarly, $CsAg_5Te_3$, which adopts a tunnel-like structure that can be described as an array of parallel $AgTe_4$ chains (Fig. 8f), was reported to have a zT of 1.5 at 727 K [138], which can be attributed to an ultralow κ of approximately 0.2 W m^{-1} K^{-1} that derives from a *concerted rattling* motion of Ag atoms [138]. $K_2Bi_8Se_{13}$ has a low-symmetry monoclinic structure with a similar tunnel-like structural motif (Fig. 8g) and κ ranging from 0.42 to 0.20 W m^{-1} K^{-1} in the 300–800 K temperature interval [140]. Multiple conduction bands near the Fermi level create a high α in this material at elevated temperatures, and when properly electron doped, it yields a zT of approximately 1.3 at 873 K (Fig. 10i). Such studies are inspiring new strategies for designing materials with low κ and high thermoelectric performance.

2.2. Silicon, silicon-germanium alloys, and Silicides

Silicon, silicon-germanium alloys (SiGe), and silicides share the common attractive feature of being based on the most well-known material and, at least in principle, of being compatible with integrated electronics technology.

Silicon discovery is traditionally credited to Berzelius (1823). Silicon crystallizes in the $Fd\bar{3}m$ space group, the well-known diamond structure, and forms solid solutions with germanium over the whole compositional range, with unlimited substitution of Ge at Si lattice sites [229].

Germanium was isolated for the first time by Winkler in 1886. Its geo-abundance is far lower than that of Si ($\approx 1.5 \times 10^{-4}$ % at.) [230]. Germanium is primarily recovered as a by-product from sphalerite zinc ores and from fly ashes of power plants fueled by Ge-rich coal, although in 2007 about 35% of the world demand was met by recycled germanium.

Silicides are a wide class of binary or multinary compounds wherein silicon forms either stoichiometric or non-stoichiometric compounds with metals. Although a very large number of silicides are known, quite a large fraction of which has been considered for thermoelectric applications, as of today only two silicides have been found to meet all requirements for practical prospective deployment, namely Mg_2Si and the so-called Higher Manganese Silicides (HMSs) of general formula $MnSi_x$ (with $1.71 \leq x \leq 1.75$). The reason, further to the achieved zT, is the silicides sustainability, which quite obviously depends upon the abundance and the toxicity of their metallic constituent. Two recent reviews [231,232] summarize the most studied metal silicides, reporting their thermoelectric characteristics, the abundance of their metallic constituent, and their stability.

2.2.1. Silicon and SiGe

Bulk growth of silicon and Si-Ge ingots are carried out using the standard Czochralski (CZ) technique [233], namely from molten Si or Si-Ge by nucleating the crystal using a suitably oriented single- crystalline seed. More often, in thermoelectric applications powders of Si or Si-Ge are used [234], which are obtained directly by decomposition of SiH_nCl_{4-n} (GeH_nCl_{4-n}) obtained by reaction of metallurgical-grade silicon with suitable bleaching agents [235]. Doping is either carried out during the CZ growth using dopants in their elemental form or by solid-state diffusion. Both Si and SiGe are thermally stable up to their melting point, and report (as single-crystals) a hardness at room temperature of $\approx$ 10 GPa, quickly decreasing at higher temperatures down to 1 GPa at

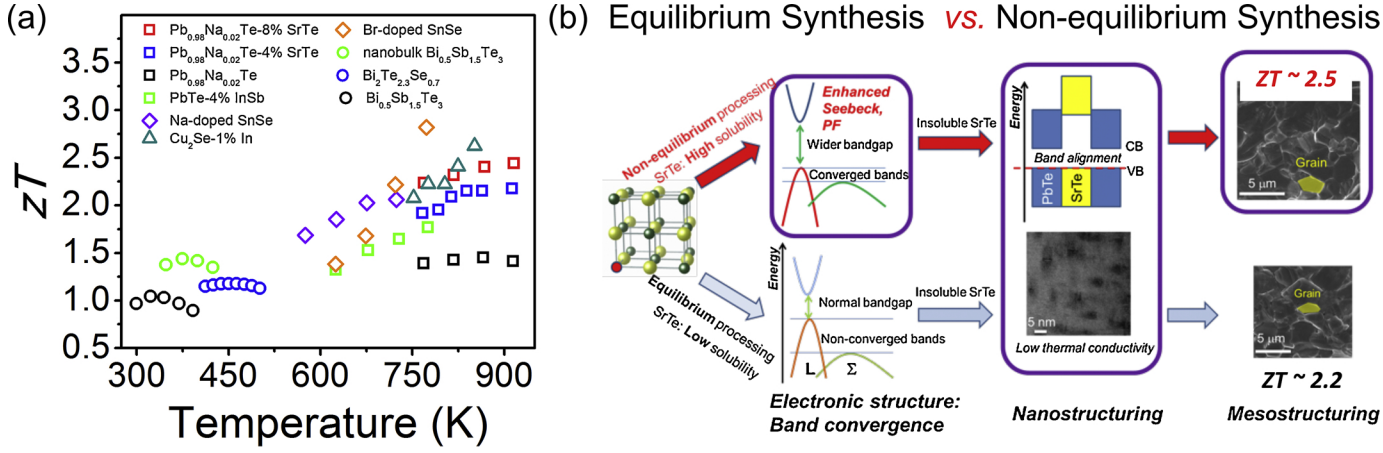

Fig. 9. (a) Peak zT values for high performance metal chalcogenide thermoelectrics. (b) Equilibrium vs. non-equilibrium synthesis of $Pb_{0.98}Na_{0.02}Te$-x%SrTe. Lower pathway: using standard high-temperature (equilibrium) synthetic methods a zT of 2.2 is achieved in $Pb_{0.98}Na_{0.02}Te$-4%SrTe, which is attributed to a decrease in κ facilitated by all-scale hierarchical architectures (atomic scale point defects, nanoscale precipitates, mesoscale grains). Upper pathway: fast quenching after synthesis (non-equilibrium) delivers greater solubility of SrTe in the PbTe matrix (greater than 5 mol%), which increases the band gap and facilitates strong valence band convergence, producing a record high zT of 2.5 in $Pb_{0.98}Na_{0.02}Te$- 8%SrTe. Adapted with permission from Ref. [191]. Copyright 2016, Nature Publishing Group.

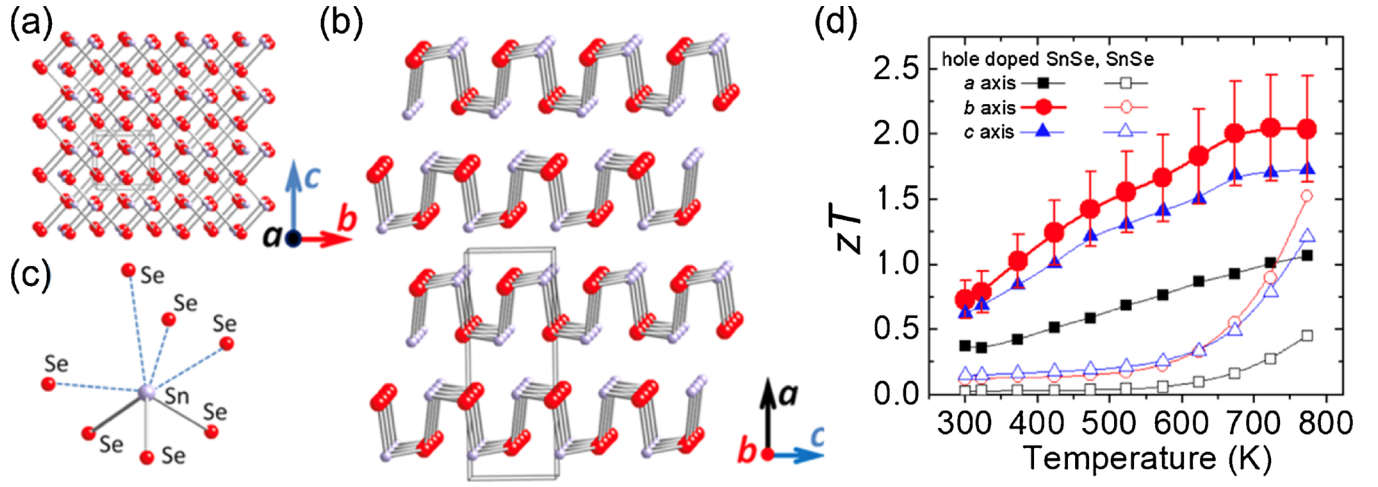

Fig. 10. SnSe crystal structure and thermoelectric performance. SnSe viewed along the a-axis (a), b-axis (b), and distorted $SnSe_7$ polyhedron with three short and four long Sn-Se bonds (c). Thermoelectric performance of undoped and hole-doped SnSe single crystals along each axis (d). Adapted with permission from Ref. [86] Ref. [204]. Copyright 2016 The American Association for the Advancement of Science.

1000 °C [236].

Low cost and the fantastic technological know-how accumulated on silicon over the last fifty years in the microelectronic industry and, more recently, in photovoltaics, has motivated a significant and growing research effort on thermoelectric applications of Si and SiGe alloys. Thermoelectric properties of single-crystalline silicon were studied in the 1950s by Geballe and Hull [238], and recently re-measured by Stranz et al. [239]. Silicon has relatively high *PF* at high doping levels. However, its relatively high κ, of about 120 W $m^{-1} K^{-1}$ at room temperature, leads to zT values of only ≅ 0.01 at room temperature. Despite its limited performances, Si-based thermoelectric generators have been developed to obtain prototypes of integrated micro-harvesters [240,241].

Increasing Si thermoelectric efficiency has been pursued by decreasing κ without reducing σ. Use of SiGe alloys was found to be a successful strategy. First studies on SiGe alloys were carried out in 1964 by Dismukes [242], who measured maximum zT values of ≅ 1 and 0.7 for *n*- and *p*-type $Si_{0.70}Ge_{0.30}$ alloys at 1100 K, with doping carried out using As or P for *n*-type, and B for *p*-type. The combined effect of alloying and polycrystallinity on κ was further exploited by Rowe et al. [243] and then by Vining et al. [244], who reported further reduction of κ by compressing (sub)micrometric powders of *n*-type $Si_{0.8}Ge_{0.2}$, although not obtaining significant changes in zT due to the increased electrical resistivity.

In 1988 Vining anticipated that thermoelectric properties of boron-doped nanocrystalline silicon (ncSi) display an improvement, difficult to be predicted, upon prolonged annealing resulting in the precipitation of SiB_3 [245], leading to an unexpected increase of hole mobility when carrier density exceeds 10^{19} cm^{-3} [244]. Similar results were also reported by Loughin et al. [246] on B:SiGe alloys ($Si_{0.790}Ge_{0.197}B_{0.013}$). Upon annealing for 30 min at 1273 K, carrier density was found to decrease from 3.4 × 10^{20} to 3.1 × 10^{20} cm^{-3} with a zT improvement of 12%, an effect also ascribed to the precipitation of a silicon boride from the solid solution.

Despite being the standard component of RTGs [249] and, as such, the benchmark for all arising new thermoelectric materials, Si and SiGe alloys did not progress appreciably as of their efficiency from 1960 to 2000. It was just with the introduction of nanotechnology that major advances could be obtained. Two avenues were walked through. Dimensional constrains were demonstrated to lead to a remarkable reduction of κ in Si. Silicon nanowires with diameters smaller than 100 nm, either obtained by electrochemical techniques [250] or by extreme lithography [251], were found capable of zT close to 1 at room temperature due to the damping of κ down to < 5 W $m^{-1} K^{-1}$ by incoherent phonon scattering at wire walls. Comparable results were reported also for nanolayers (i.e. thin films with thickness below 200 nm) [102]. The same approach was attempted for SiGe alloys. As expected, the reduction of their κ (from 3.0 to 1.8 W K^{-1} m^{-1}) [252] was found to be much less important than in Si, as Ge substitutional defects already limit phonon mean free path. SiGe nanowires were reported to improve zT values by a factor two [253], up to 0.46 at 450 K [254]. Nanotechnological control of κ was also achieved in bulk material [247] (Fig. 12a–b). A record zT of 1.3 at 1173 K was reported in 2008 [255] for phosphorus-doped $Si_{0.8}Ge_{0.2}$ pellets obtained by hot pressing nanopowders. At a final grain size of 10–20 nm the material was found stable under operative conditions. Similar outcomes were obtained in boron-doped pellets, with a zT of 0.95 at 1173 K [255].

A significant research effort [256] has further addressed the manufacturability of silicon nanowires [257,258] and the factors controlling the reduction of their κ [259], also extending this strategy to nanolayers [260,261] and to *holey* silicon, namely silicon membranes with an ordered array of nanometric holes [262], where values of κ of 1.5 and ≅2 W $m^{-1} K^{-1}$, respectively, could be achieved. Silicon rejuvenated not only as 1D and 2D systems, however [263]. Also in bulk silicon, several authors reported enhanced zT. Si nanoparticles compacted by Spark Plasma Sintering (SPS) to yield average crystallite size between 40 and 80 nm displayed zT values up to 0.32 at 973 K depending on the sintering temperature [264]. Evidence of a concurrent increase of α and of σ in nanocrystalline $Si_{0.91}B_{0.09}$ upon second phase precipitation was reported [265,266]. The simultaneous increase of both transport coefficients (up to 480 Ω^{-1} cm^{-1} and 0.5 mV K^{-1}) [100], ascribed to energy filtering, led to a *PF* value of 15.9 mW m^{-1} K^{-2} at 350 K and therefore to zT values exceeding 0.5 [267]. High *PF* (≈ 4.4 mW m^{-1} K^{-2} at 1073 K) was also reported in Si and $Si_{0.99}Ge_{0.01}$ pellets by Yusufu et al. [268] upon precipitation of a phosphorus-rich second phase structurally (semi)coherent with the embedding microcrystalline silicon. The reduction of κ and the increase of *PF* led to a zT of 0.6 at 1050 K. Defect-engineering was used instead by Bennett et al. [269] to reduce κ of non-nanostructured single-crystalline Si thin films to 4.7 W $m^{-1} K^{-1}$, therefore leading to zT = 0.2 at 360 K, a temperature at which vacancy diffusion is negligible even over long operation times. This further confirmed the potential of Si as a low- temperature alternative to tellurides.

Some improvements were also quite recently reported on SiGe alloys. Using the concept of modulation doping, enhanced *PF* and a zT ≈ 1.3 at 1173 K were observed in SiGe in mixtures of two types of SiGe nanoparticles, one of which heavily boron-doped [270]. Favier et al. [271] showed instead that $Si_{0.91356}Ge_{0.07944}P_{0.0070}$ mechanically

alloyed with 1.3 vol.% nanosized Mo upon SPS is capable of a zT of ~ 1.0 at 973 K.

2.2.2. Silicides

Most silicides are obtained as powders by solid state reaction between silicon and the relevant metallic phase [231,272,273]. Stability ranges widely change depending on the metallic species. For HMSs, stability extends up to 950 K. Instead, Mg_2Si is stable below 850 K [232].

First studies on silicides for thermoelectric applications date back to 1958, when Nikitin carried out the first studies of transition metal silicides [274]. Mg_2Si attracted primary research attention due to the easy preparation [231] and the ample possibility of tailoring its thermal properties and its electronic structure by the formation of solid state solution of general formula $(Mg,Ca)_2(Si,Ge,Sn)$. Mg_2Si crystallizes in the antifluorite structure (*Fm3m* space group) (Fig. 11a). Values of zT of 0.8 were reported already in 1989 by Marchuck et al. [275]. In the same years, $MnSi_x$ (with $1.71 \leq x \leq 1.75$) was the subject of extended investigations, which were however initially hampered by the structural complexity of the system. HMS crystallizes with a complex chimney-ladder structure with tetragonal cells (Fig. 11b) [237]. Furthermore, it forms with many compositions. HMS crystals are made up of compositionally homogeneous regions separated by layers of MnSi, oriented normally to the crystal c-axis. Early investigations of HMS reported zT values of 0.3 at 673 K [276].

The evolution of performances of Mg_2Si and HMS runs quite in parallel. A noteworthy efficiency improvement of Mg_2Si was obtained in 2011 by Fedorov and coworkers [278] by partial substitution of Si with Sn. Mg_2Si-Mg_2Sn solid solutions were obtained with a peak zT of 1.2 at 750 K. Ternary Mg_2Si- $Si_{0.88}Ge_{0.12}$ and $FeSi_2$- $Si_{0.88}Ge_{0.12}$ systems were proposed in 2009. In these materials, silicides form nanoinclusions that reduce κ by a factor ranging from 4 to 8, thereby enhancing zT over that of $Si_{0.8}Ge_{0.2}$, despite the lower amount of Ge [279].

Concerning HMS, comparable results required an initial major effort to be spent to further clarify its structure, also in combination with its very complex phase diagram [280–282]. The momentum that such endeavor provided to research led however to remarkable improvements in HMS efficiency. In 2009 Itoh and Yamada reported that phases of $MnSi_{1.73}$ mechanically alloyed with MnSi and then submitted to pulse discharge sintering displayed zT of 0.47 at 873 K [283]. A year later Zhou et al. [277,284] found that addition of SiGe to polycrystalline HMS led to a partial substitution of Ge to Si along with the precipitation of SiGe phases (Fig. 13a). Mostly because of the reduction of κ_{ph} down to 1.6 W m^{-1} K^{-1} at 450 °C, while not affecting *PF*, a maximum zT of 0.5 was achieved in $MnSi_{1.733}$ – 0.02SiGe at 823 K. Use of nanoprecipitates was also reported by Luo et al. [272] in p-type HMS wherein a nanophase of MnSi precipitated. Energy filtering led to an increase of σ by 30% with unchanged α, while κ was significantly reduced from 3.0 to 1.3 W m^{-1} K^{-1} so that a zT of 0.62 at 800 K could be obtained. Nanoprecipitates were not the only route to increase zT, however. Still in 2011 Luo et al. reported a zT of 0.65 at 850 K by substituting Si with Al in HMS to form a solid solution of Mn $(Al_{0.0015}Si_{0.9985})_{1.80}$ [285].

Further advances were achieved over more recent years. Also guided by theoretical estimates [286], Al doping (2.0% mol) was found to increase Mg_2Si maximum zT to 0.47 at 823 K [287] while Sb doping (1.5% mol) was shown to be capable of a zT of 0.46 at 810 K [288]. Battiston et al. [289] reported in 2013 a larger maximum zT at 873 K of 0.50 for the 1.0% mol. Al-doped Mg_2Si. In the same year zT of ≅ 1.4 for Bi-doped and of ≅ 1.2 for Sb-doped were reported at 800 K. Studies also covered the critical mechanical stability of the silicide [290]. Although powders of Mg_2Si react with water and moisture, it was found that the reaction does not drive crack growth, which is beneficial to the fabrication of Mg_2Si-based devices wherein microcracks induced by mechanical operations during fabrication might have led to TEG failure. More recently, Mg_2Si was also considered for nanoinclusions in SiGe alloys. This resulted in zT enhancements for $Si_{0.88}Ge_{0.12}$-Mg_2Si nanocomposites, reaching 1.3 at 1250 K [291].

Comparable achievements were presented for HMSs. Gelbstein et al. described nanostructured n-type $Mg_2Si_{1-x}Sn_x$ and p-type HMSs with high maximal zT values respectively of 1.1 and 0.6 at 723 K [292]. In 2017 Te nanowires embedded to HMS were shown to increase zT from 0.41 to 0.70 at 800 K [293].

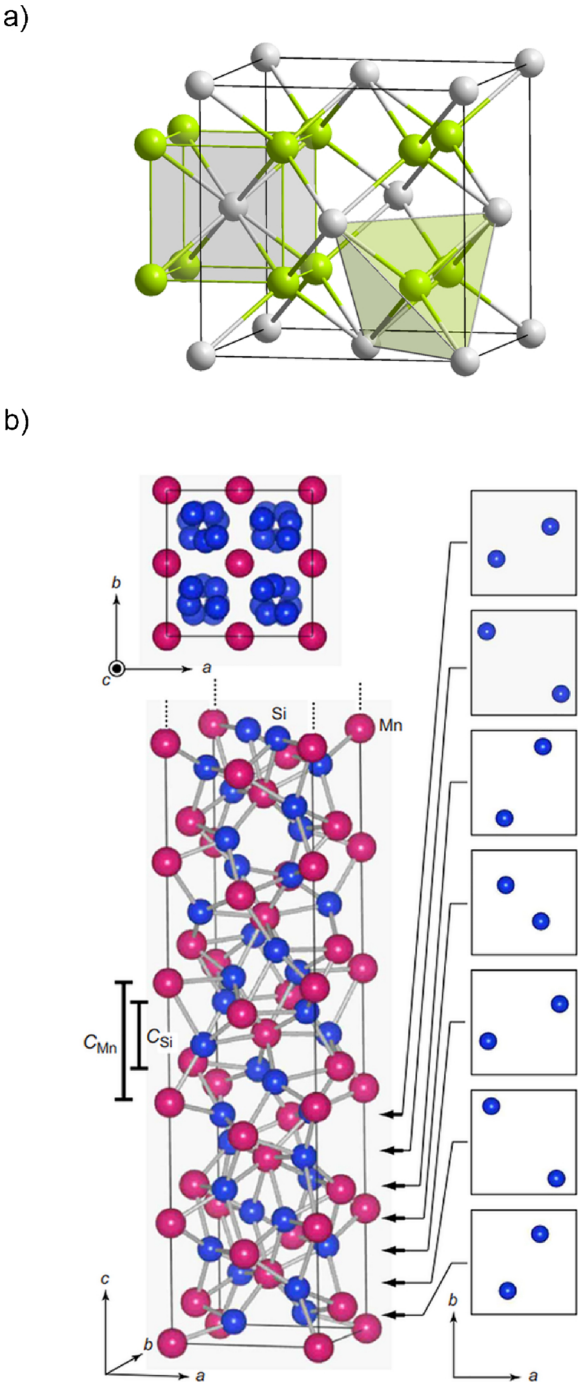

Fig. 11. Crystallographic structure a) of Mg_2Si, showing the coordination shells of Mg (gray) and of Si (green); and b) of the incommensurate phase $MnSi_{1.71}$ at 295 K. The c-axis projection (top) displays the rotational arrangement of chimney-Si atoms while the squares (right) are sections normal to the c-axis of the first seven Si layers. Reproduced with permission from Ref. [237]. Copyright 2008 American Physical Society (for interpretation of the references to colour in this figure legend, the reader is referred to the web version of this article).

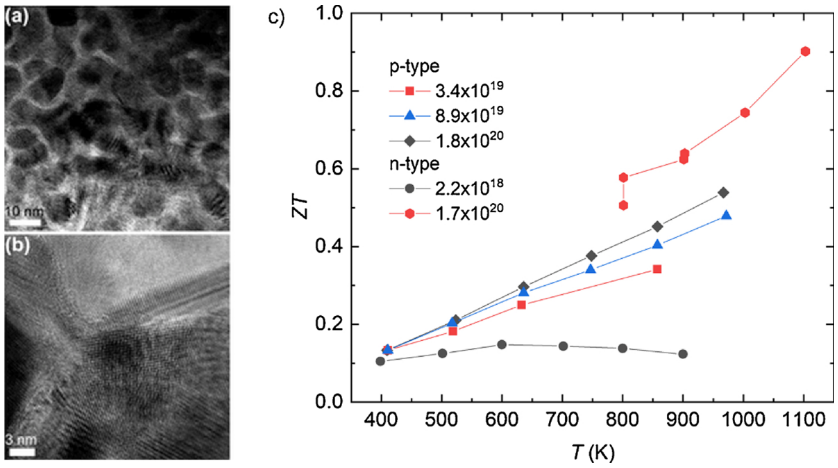

Fig. 12. TEM images with (a) low and (b) high magnifications of as-pressed $Si_{0.8}Ge_{0.2}$ hot-pressed nanopellets. Reproduced with permission from Ref. [247]. Copyright 2008 American Institute of Physics. c) Summary of zT values vs. temperature for *p*- and *n*-type $Si_{0.7}Ge_{0.3}$ nanopellets at high doping levels. Dopant densities in cm^{-3}. Reproduced with permission from Ref. [248]. Copyright 2009 American Physical Society.

2.3. Skutterudites

Skutterudite is a natural occurring mineral - cobalt arsenide ($CoAs_3$) - discovered in Skotterud (Norway, 1845). Its general formula is TPn_3, where T is a transition metal and Pn stands for pnictogen (elements from group 15 of the periodic table), as firstly described by Oftedal [294,295]. It presents a cubic structure (Space Group: Im3) containing a transition metal (T = Co, Rh, or Ir; in blue in Fig. 14) with six out of the eight cubes filled with pnictogen in nearly square rectangles (in purple in Fig. 14). The Pn-Pn bonds are close enough to be considered formal bonds. The two unfilled cubes can be filled by large cations that act as *rattlers* in the structure. These rattlers serve to optimize both electronic and thermal properties by tuning the carrier concentration and the phonon scattering. This *filled skutterudites* are not naturally occurring and can be described by the general formula $\square\ {}_1T_4Pn_{12}$ ($\square$: can be a rare earth or an alkaline earth element). The structure can also be described as a distorted perovskite ReO_3, as shown in Fig. 14b. In this description of the structure, the rattler occupies the void space between the distorted octahedral (mark in gray in Fig. 14b) and forms a weak bond. Detailed information on structural parameters of binary skutterudites, based on P, As, and Sb can be found in Refs. [296–298].

Among all the skutterudites, the most studied as thermoelectric materials are those based on antimony, because of their unusual band structure showing a pseudogap around the Fermi level, high μ, atomic mass, σ, and α [299].

The first values in single crystals were obtained in 1996 by Caillat et al. They observed high μ ($3445\ cm^2V^{-1}s^{-1}$) and a charge concentration of $10^{17}\ cm^{-3}$ at room temperature for $CoSb_3$ [300]. Those values were increased at higher temperatures and when doped, reaching zT values up to 0.52 at 873 K for heavily doped *n*-type $CoSb_3$ single crystals.

Even though Sb is not one of the most abundant elements, skutterudites are among the most appealing thermoelectrics to date in the fabrication of modules for applications at medium temperatures (400–850 K), since they are among the most efficient in this temperature range. In addition, depending on the charge carrier concentration, which can be controlled by chemical substitution and filling factor, skutterudites solid solutions can behave as *n* or *p*-type semiconductor with high power factors ($> 30\ \mu W\ cm^{-1}\ K^{-2}$) and high zT values. For instance, $zT = 1.3$ has been measured in *p*-type $DD_{0.59}Fe_{2.7}Co_{1.3}Sb_{11.8}Sn_{0.2}$ and $zT = 1.8$ was measured in *n*-type (Sr, Ba, Yb) Co_4Sb_{12} + 9.1 wt.% $In_{0.4}Co_4Sb_{12}$ [301,302].

The main drawback for skutterudite single crystals is their high κ ($8.9\ W m^{-1} K^{-1}$ at 300 K). Accordingly, most of the efforts to increase the zT of skutterudites in the last decades have been focused on the reduction of κ [39,132,143,298,303–305], with one of the most

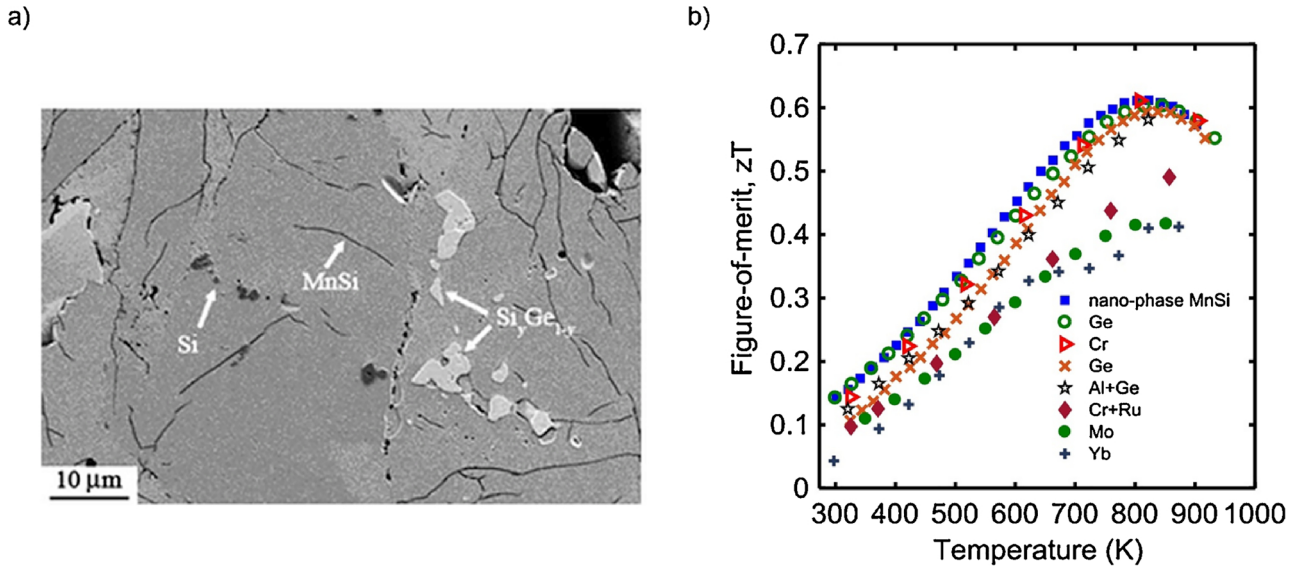

Fig. 13. a) Si_yGe_{1-y} inclusions in $Mn(Si_{1-x}Ge_x)_{1.733}$ with x = 1.6%. Reproduced with permission from Ref. [277]. Copyright 2009 Springer Nature. b) Summary of zT values vs T for HMS samples doped with different species. Reproduced from Ref. [234]. Copyright 2017 The Japan Society of Applied Physics.

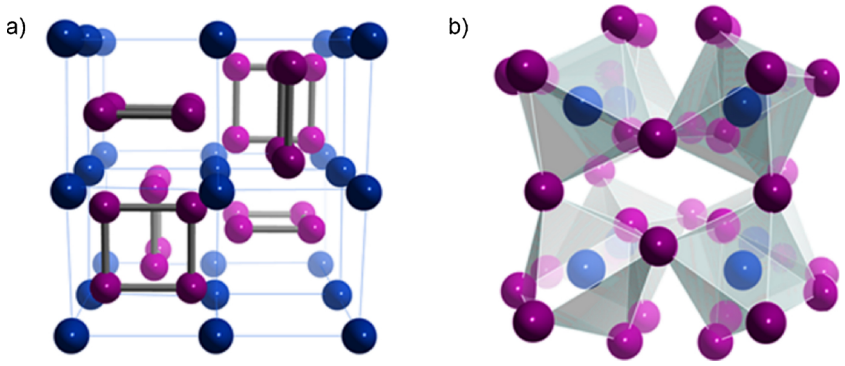

Fig. 14. crystalline structure of the skutterudite a) described by Oftedal et al. and b) defined by Kjekshus et al., as a distorted perovskite structure. Structures produced using the crystallographic data reported in Ref. [297].

investigated strategy relying on Slack's phonon-glass electron-crystal concept [39]. The latter applies particularly well to skutterudites due to their crystallographic structures: in fact, the *cages* can host guest atoms (*rattlers*) that can play a role in diminishing the lattice thermal conductivity by scattering acoustic phonons. Other ways to improve zT in skutterudites has consisted in the substitution of Co and/or Sb atoms to generate defects and doping, and in material nanoengineering to produce inclusions, nanocomposites, or interfaces that help to further reduce κ due phonon scattering. In particular, in regards of the Co and/or Sb substitution, the research in the last decades has focused on their replacement by ions with a higher number of electrons (for *n*-type), or by ions with a lower number of electrons (for *p*-type). Moreover, it has been proved that doping can also reduce κ. [307]. The most commonly employed dopants at the Co sites have been Fe (for *p*-type) and Ni, Pd, and Pt (for *n*-type) and, on the Sb site, Te, Ge, Sn, and/or Se. Among them, Fe and Ni are the most studied.

The fabrication process of $CoSb_3$ compounds (doped and undoped) is based on the combination of material synthesis and compaction. A variety of different methods have been explored so far. On the one hand, material synthesis has been successfully achieved by chemical synthesis, mechanical alloying melting, high-energy ball milling, melting-annealing-grounding, melting-quenching-grounding, self-propagating high temperature synthesis, solid state reaction, and radio frequency [298,303]. On the other hand, compaction from powder has been done by plasma activated sintering, hot press, high- pressure torsion, high pressure, and spark plasma sintering, to cite a few. It is important highlighting that the selection of the fabrication and the compaction techniques places a crucial role on the final thermoelectric properties of the material, as the same material produced from different routes can present different properties. This is due to, for example, the segregation of impurities at the grain boundaries, the formation of different nanoinclusion, and/or the degree of compaction. All these can regulate the final properties. Although this is not important for skutterudites only, it is evident that in this particular case it places a significant role.

The most recent works on novel synthetic methods of skutterudites are mainly focused on large-scale production and/or fast production, e.g. by means of microwave-assisted or ball milling. The first work reporting large quantities (5 Kg) of *n*-type La-filled skutterudite with a zT of 1 at 773 K skutterudite has appeared in 2017 [306].

In the case of *n*-type skutterudites, some of the highest zT ever achieved for compounds doped at the cobalt site are 0.6 at 800 K in bulk $Co_{3.8}Ni_{0.2}Sb_{12}$, and 0.9 at 750 K in single crystal $CoSb_3$ co-doped with Pt and Pd at 5% each [308,309]. While the highest zT of *n*-type skutterudites doped at the Sb site are 0.95 at 800 K in bulk $CoSb_{2.8}Te_{0.2}$, and 1.1 at temperatures above 800 K for $CoSb_{2.75}Ge_{0.05}Te_{0.2}$ and $CoSb_{2.75}Sn_{0.05}Te_{0.2}$ [307,310,311]. The highest reported zT value for an unfilled skutterudite is of 1.6 for a porous microstructure of $CoSb_{2.75}Si_{0.075}Te_{0.175}$ containing nano and micropores, random in shape and orientation. This type of structure appears to scatter a wide range of phonons, thus significantly reducing k [312]. Finally, for co-doping on Co and Sb site, the best values obtained so far are for $Co_{3.9}Ni_{0.1}Sb_{11.5}Te_{0.4}Se_{0.1}$ with a zT of 1.1 at 725 K [313]. By combining the doping with rattlers to reduce the thermal conductivity, the thermoelectric properties of skutterudites have experienced a noticeable increase, and zT equal to 1.2 at 800 K, 1 at 800 K, and 1.2 at 775 K have been achieved in $Ba_{0.3}Ni_{0.05}Co_{3.95}Sb_{12}$, $Ca_{0.18}Co_{3.97}Ni_{0.03}Sb_{12}$ and $Ca_{0.07}Ba_{0.23}Co_{3.95}Ni_{0.05}Sb_{12}$, respectively [314,315]. At that point, it seemed a limit in the efficiency had been reached by introducing a unique guest atom. Nevertheless, the so-called multi-filling was found to be efficient in scattering a broader number of phonon modes by using fillers with different size, mass, etc. This effect was first postulated by Yang et al., who predicted a higher phonon scattering by choosing two guest atoms with an as high as possible different resonance frequency [316]. One of the first experimental works in showing a strong reduction in thermal conductivity by using two different guest atoms was done by Lu et al. [317]. Some of the best-reported results so far are found in the $Ba_{0.08}Yb_{0.09}Co_4Sb_{12.12}$ compound, with $zT = 1.36$ at 800 K, in $Ba_{0.14}In_{0.23}Co_4Sb_{11.84}$, with $zT = 1.34$ at 850 K and in $Ba_{0.18}Ce_{0.05}Co_4Sb_{12.02}$, with $zT = 1.26$ at 850 K [318–320]. Up to now, the best *n*-type skutterudite obtained by adopting this approach is $Ba_{0.08}La_{0.05}Yb_{0.04}Co_4Sb_{12}$ with a $zT = 1.7$ at 850 K, in which three different guest atoms were used [321].

In the case of *p*-type skutterudites, the highest zT values achieved by doping alone never exceeded 0.5. Thankfully, significant improvement came from the introduction of rattlers. The first promising results for *p*-type were reported by Morelli et al. by the addition of Ce (rattler) to the $FeSb_3$ skutterudite [322]. They have shown a reduction of the thermal conductivity by one order of magnitude. Since then, different types of filler combinations have been studied, among which Pr and Nd, La and Yb, Nd and Yb, and Ce, with zT ranging from 0.7 to 1.3. [323–326]. One of the best results achieved adopting this strategy reported a zT of 1.3 for $DD_{0.59}Fe_{2.7}Co_{1.3}Sb_{11.8}Sn_{0.2}$ [301].

Some strategies can be applied to increase performances of both *n*- and *p*-type skutterudites. For example, as a way to increase the filling factors of skutterudites, techniques such as high-pressure sintering (HPS) or high pressure–high temperature (HPHT) using diamond anvil cells (DACs) are shown to be good alternatives [327–335]. In some occasions, these methods are also used in combination with non-equilibrium syntheses such as melt spinning $R_yCo_4Sb_{12}$ (R = Nd, Sm, Gd, Tb, and Dy with zTs up to 1.3) or super-cooling reaching similar zT for $R_yCo_4Sb_{12}$ (R = Ce, Ca, Nd, Sm, Gd, Yb, Dy).

Nowadays, there are some appealing ideas to increase the zT of skutterudites that need further exploration in the future, like the introduction of micro- and nanopores, the formation of hierarchical structures, or the control and understanding over grain boundary engineering, the connectivity, microstructure, and type of which have been show to play a role in the transport phenomena.

Nanoinclusions can be obtained by different fabrication strategies such as *in situ* precipitation, ultrasonic dispersion [336], or mechanical mixing. Examples of zT improvement by the introduction of nanoinclusions by hot pressing are given by Fu et al., who found that core-shell microstructures in skutterudites doped with a 2% of Ni reaches $zT = 1.07$ at 723 K [337], that the formation of nano-islands of InSb in the $In_{0.2}Ce_{0.15}Co_4Sb_{12}$ compound improves zT up to 1.43 at 800 K [338], and that GaSb nanoinclusions in $Yb_{0.26}Co_4Sb_{12}$/0.2GaSb allows achieving zT of 1.45 at 850 K [339], or $zT = 1$ in the *p*-type $Nd_{0.6}Fe_2Co_2Sb_{11.7}Ge_{0.3}$ at 770 K [340]. It is important to highlight that although nanoparticles (inclusions) play a key-role in the scattering of phonons at grain boundaries, they also affect the mechanical properties of the final nanocomposite.

Hierarchical design in thermoelectric skutterudites has also been proven to scatter phonons more intensely over a broader range of frequencies than bulk Te-doped skutterudite, with the maximum zT of 1.1 at 820 K for $CoSb_{2.875}Te_{0.125}$ [341].

Concerning grain boundaries engineering, Moure et al. showed that cell expansion and charges at the interfaces between skutterudites and oxides can help to decouple the power factor, controlled by the skutterudite phase, from the thermal conductivity, controlled by the interfaces, allowing to reach zT higher than 1 [342]. In Fig. 15, a clear and abrupt lattice expansion in the last 3 distances of the < 110 > direction of $CoSb_3$ when getting closer to the boundary with $CoSb_2O_4$ oxide, can be observed. This feature, supported by micro-Raman observations, points toward the presence of an effective interface to scatter phonon. Zhang et al. showed that the use of Yb_2O_3 nano- precipitates and the presence of CNTs at the grain boundaries can improve mechanical stability and zT properties up to 1.43 at 875 K [343]. Zong et al. have shown that graphene modified grain boundaries are good for enhancing zT [344]. All these works open a whole new research direction in the field and highlight the importance of proper nanoengineering of grain boundaries.

Thermopiles and/or generators for intermediate temperature range applications are starting to achieve remarkable efficiency values, close to 10% at laboratory scale, with excellent mechanical stability at high temperatures and interesting reproducibility [349–351]. Those 10% efficiencies are similar to the ones obtained for commercial Bi_2Te_3-based modules for close to room- temperature applications. A critical aspect when fabricating thermoelectric modules based on skutterudites is that *p*-type skutterudites have a predominantly higher thermal expansion coefficient than *n*-type ones. Thus, more work should be done in order to minimize the difference in thermal expansion coefficients between *p*- and *n*-type skutterudites. Finally, modules based on skutterudites materials must be encapsulated in order to avoid oxidation at high temperatures, which can severely damage the devices themselves. To this purpose, Park et al. demonstrated that an enamel coating is effective in avoiding oxidation in devices operating open air, up to 933 K [352]. In summary, skutterudites are currently among the best thermoelectric materials for medium range temperature applications. The zT versus temperature curves of some state-of-the-art p- and n-type skutterudites are shown in Fig. 16.

2.4. Zintl phases

The term *Zintl phase* refers to a large and continuously-growing class of intermetallic compounds that obey a common set of rules describing their structure and bonding. In general, Zintls can be defined as having structures composed of covalently-bonded polyanions surrounded by cations that donate their valence electrons to yield overall charge balance [353–355]. Although Zintl phases are relative newcomers to the field of thermoelectrics, the study of their structures and chemical

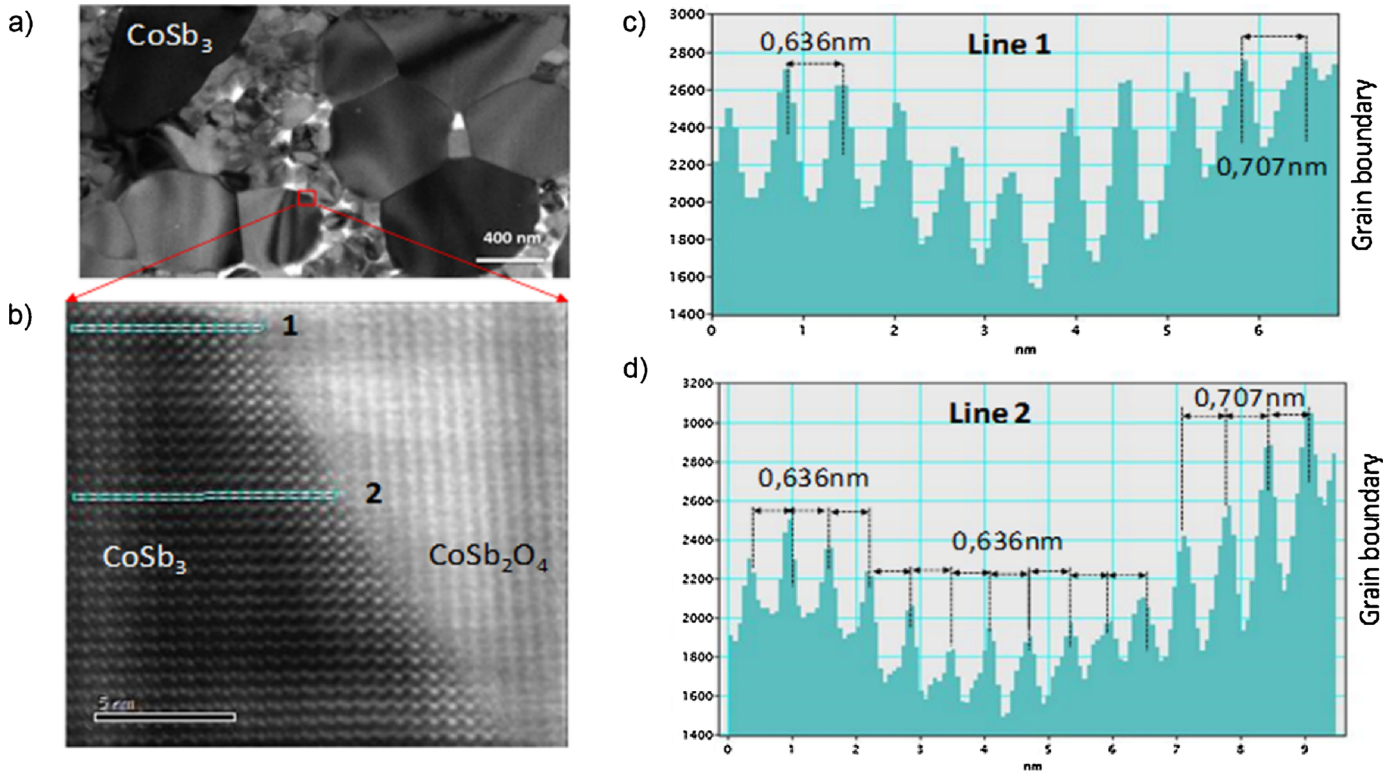

Fig. 15. HRTEM images of the interface $CoSb_3/CoSb_2O_4$ of a nanocomposite. a) General image of the CoSb3/oxides nanocomposites prepared in situ by ball milling. b) detailed HRTEM image of the $CoSb_3/CoSb_2O_4$ interface, where the interplanar distances of $CoSb_3$ in the < 110 > direction is observed. c) and d) line analysis (shown in green in Fig. 15b). It can be shown a lattice expansion of $CoSb_3$ when getting closer to the boundary with $CoSb_2O_4$. The last 3 lattice distance expand from 0.64 nm to 0.71 nm. This effect at the $CoSb_3$ grain boundaries seems to improve the scattering of phonons at the interfaces. Adapted with permission from Ref. [342]. Copyright 2017 Elsevier (for interpretation of the references to colour in this figure legend, the reader is referred to the web version of this article).

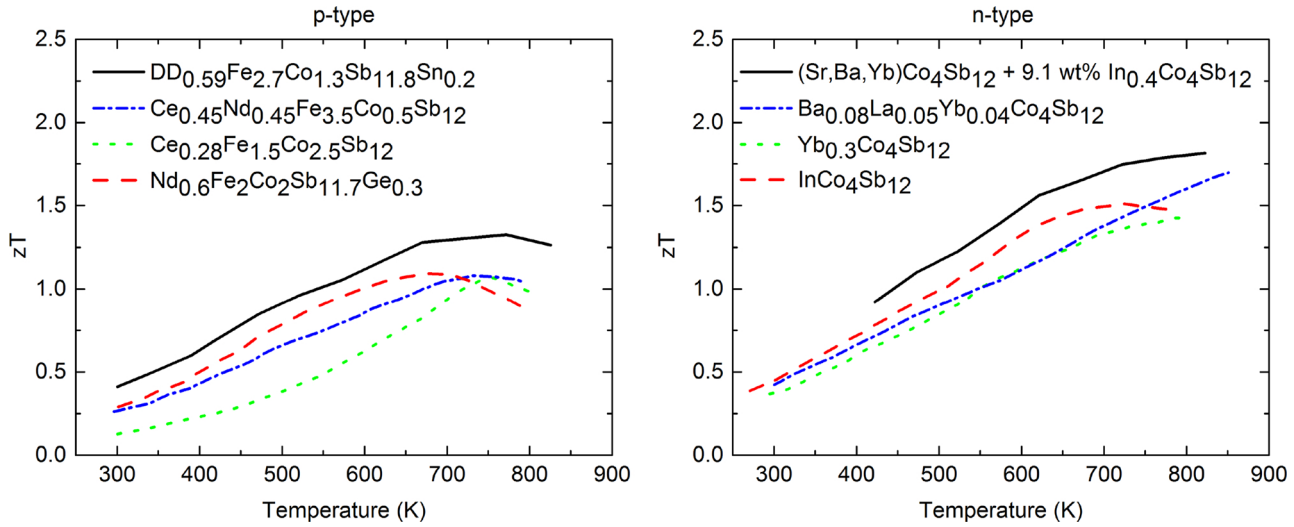

Fig. 16. zT values vs. temperature of some of the best *p*- and *n*-type skutterudites. Data from Refs. [301,302,321,340,345–348].

bonding began nearly a century ago, in the 1920s [355]. Zintl phases are named after Eduard Zintl, who, beginning in 1928, synthesized and characterized a series of intermetallic phases that appeared shiny like metals but possessed salt-like crystal structures - a contradiction that perplexed chemists at the time. Zintl proposed a set of rules - later extended by William Klemm and now known as the Zintl-Klemm concept - that can be used to rationalize the structures of even highly complex salt-like intermetallic compounds based on the number of valence electrons [355]. This rule holds that the number of covalent bonds formed by each anion is equal to 8- VEC_{anion}, where VEC_{anion} is the number of valence electrons available per formula unit, divided by the number of anions.

The strict relationship between the number of valence electrons available to each anion and the formation of covalent bonds leads to the manifestation of an incredibly diverse range of polyanionic sub-structures. These include isolated zero-dimensional moieties, 1D chains, 2D slabs and 3D networks. The structures of several Zintl phases shown in Fig. 17 illustrate the range of polyanion dimensionalities. $Yb_{14}MnSb_{11}$ contains isolated 0-dimensional polyanions [356], $YbZn_2Sb_2$ forms 2-dimensional anionic Zn_2Sb_2 slabs [357], Ca_3AlSb_3 contains chains of corner-linked tetrahedra [358], and the Ga and Sb in $BaGa_2Sb_2$ form a tunnel-like 3D structure in which the cations reside [359]. In general, we see that a higher cation-to-anion ratio has the effect of *cutting* the polyanions into smaller units, thus reducing the dimensionality.

It is difficult to draw a strict border around what is, and what is not, a Zintl compound. This is further complicated by the wide applicability of Zintl electron counting rules, which can be used for most semiconductors. For the purpose of this section, Zintl phases will be distinguished from other semiconductors by the presence of electropositive cations (e.g., Na, Ca, Yb) and the assumption of complete charge transfer (i.e., ionic bonding) to the anionic sub-structures. Thus, some intermetallic clathrate compounds can be formally considered Zintl phases, as they contain electropositive cations such as Ba or K, and they obey Zintl-Klemm electron counting rules [360]. However, because clathrates represent an important class of thermoelectric materials in their own right, they are covered separately in Section II.e. Half-Heuslers, on the other hand, are not considered Zintl phases, since complete charge-transfer from the transition metal cations to the anions is a poor assumption (although Zintl electron counting can still be applied) [361,362]. It is also important to stress that many of the Zintl phases of greatest interest for thermoelectric applications are those that push the boundaries of Zintl chemistry. They may deviate significantly from the valence-precise composition ($Yb_{14}Al_{1-x}Mn_xSb_{11}$) [363], contain intrinsic defects (interstitials as in $Ca_9Zn_{4+x}Sb_9$ [364] and or vacancies in $Yb_{1-x}Zn_2Sb_2$ [365]), or the *covalently-bonded* polyanions may have significant ionic character (Mb_3Sb_2 [366]).

The majority of the thermoelectric Zintl phases discussed here are ternary pnictides. Unlike traditional semiconductors, these typically cannot be synthesized by directly melting and annealing the constituent elements, since in many instances, melting occurs incongruently, at very high temperatures, and/or the cations are highly reactive with silica ampules (therefore, molten samples must always be contained in

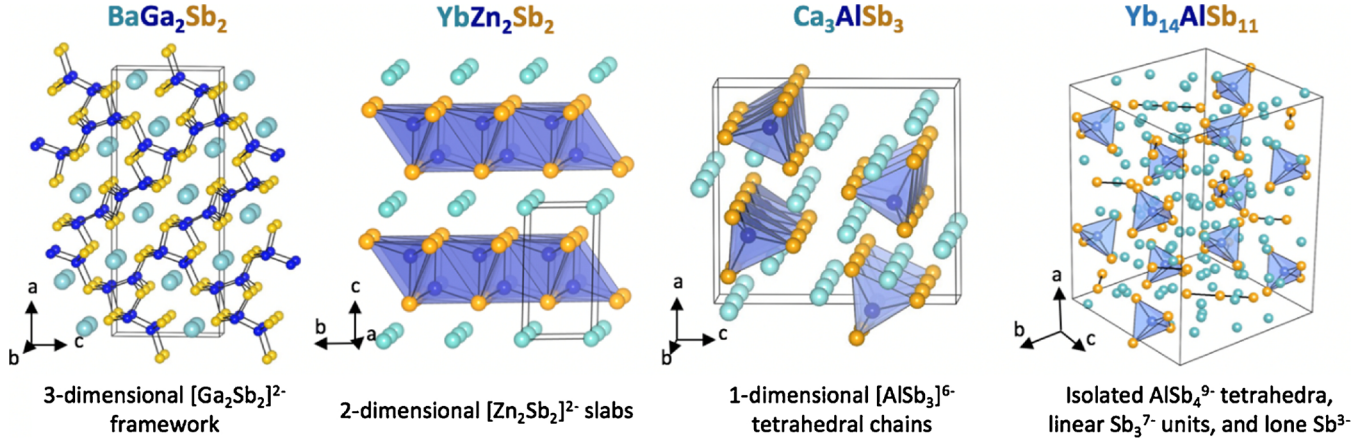

Fig. 17. The term "Zintl phase" encompasses many different structure types with polyanionic sub-structures that range from 3- to 0-dimensional.

an Al_2O_3 crucible). For these reasons, the most convenient and widely-used method for synthesizing bulk, polycrystalline Zintl samples is by direct ball milling of the elements in a high-energy mixer/mill, followed by hot pressing or spark plasma sintering in graphite dies [367]. This route is entirely solid state, thus avoiding all of the challenges associated with melting, and lends itself to preparation of larger batch sizes. For the synthesis of single crystals, growth from a molten metal flux has proven to be invaluable [368–370]. This involves dissolving components of the target compound in a lower melting-temperature flux (e.g., Sn [371], ZnSb, MgBi [372,373]), slowly cooling below the melting temperature of the target phase, followed by centrifugation to separate the molten flux from the grown crystals.

The salt-like nature of Zintl compounds sometimes leads to refractory behavior, with excellent chemical stability and performance at high temperature. $Yb_{14}MnSb_{11}$ exemplifies this, with a maximum zT at approximately 1273 K. Lifetime testing of polycrystalline $Yb_{14}MnSb_{11}$ at the NASA Jet Propulsion Laboratory has verified its long-term stability at the maximum operating temperature [374]. The figure of merit of a sample aged for six months at 1325 K under dynamic vacuum (to approximate the conditions experienced in space applications) showed no significant deterioration in performance. There are very few other reports of life-time testing of Zintl phases. Some Zintl thermoelectrics have been shown to be stable under repeated measurements up to 1000 K (e.g., chain-forming Zintls) [375–377], while others may be stable only to ~800 K (e.g., layered AM_2Sb_2 compounds). Little is known, however, about the mechanical properties, thermal expansion, and chemical robustness of these materials at high temperatures.

Serious interest in Zintl phases as thermoelectric materials (see Section II.e for a separate discussion of clathrates) began in 2005, when Gascoin et al. reported promising thermoelectric properties in the *p*-type $Ca_xYb_{1-x}Zn_2Sb_2$ system [378], with a peak zT of 0.55 at 750 K. Shortly thereafter, a peak zT of 1.0 at 1200 K in $Yb_{14}MnSb_{11}$, which exhibits exceptionally low κ_{ph} (0.5 W $m^{-1}K^{-1}$), was reported by S. Brown et al. [371]. This represented an immense improvement over the heritage high-temperature *p*-type material, $Si_{0.8}Ge_{0.2}$, prompting serious interest from the NASA Jet Propulsion Laboratory in the development of $Yb_{14}MnSb_{11}$ for use in RTGs. The discovery of $(Ca,Yb)Zn_2Sb_2$ and $Yb_{14}MnSb_{11}$ spurred an initial flurry of studies on isostructural antimonides with the layered $CaAl_2Si_2$ structure type and the $Ca_{14}AlSb_{11}$ type [363,379–385], many of which are narrow band gap semiconductors with promising zT. Much of the progress in Zintl thermoelectrics since 2005 has been in the identification of new compounds and structure types that possess the necessary combination of semiconducting behavior, tunable carrier concentration, and low κ_{ph}. Structurally, today's Zintl thermoelectrics can be broadly categorized into the following groups: chain-forming compounds (Ca_3AlSb_3,

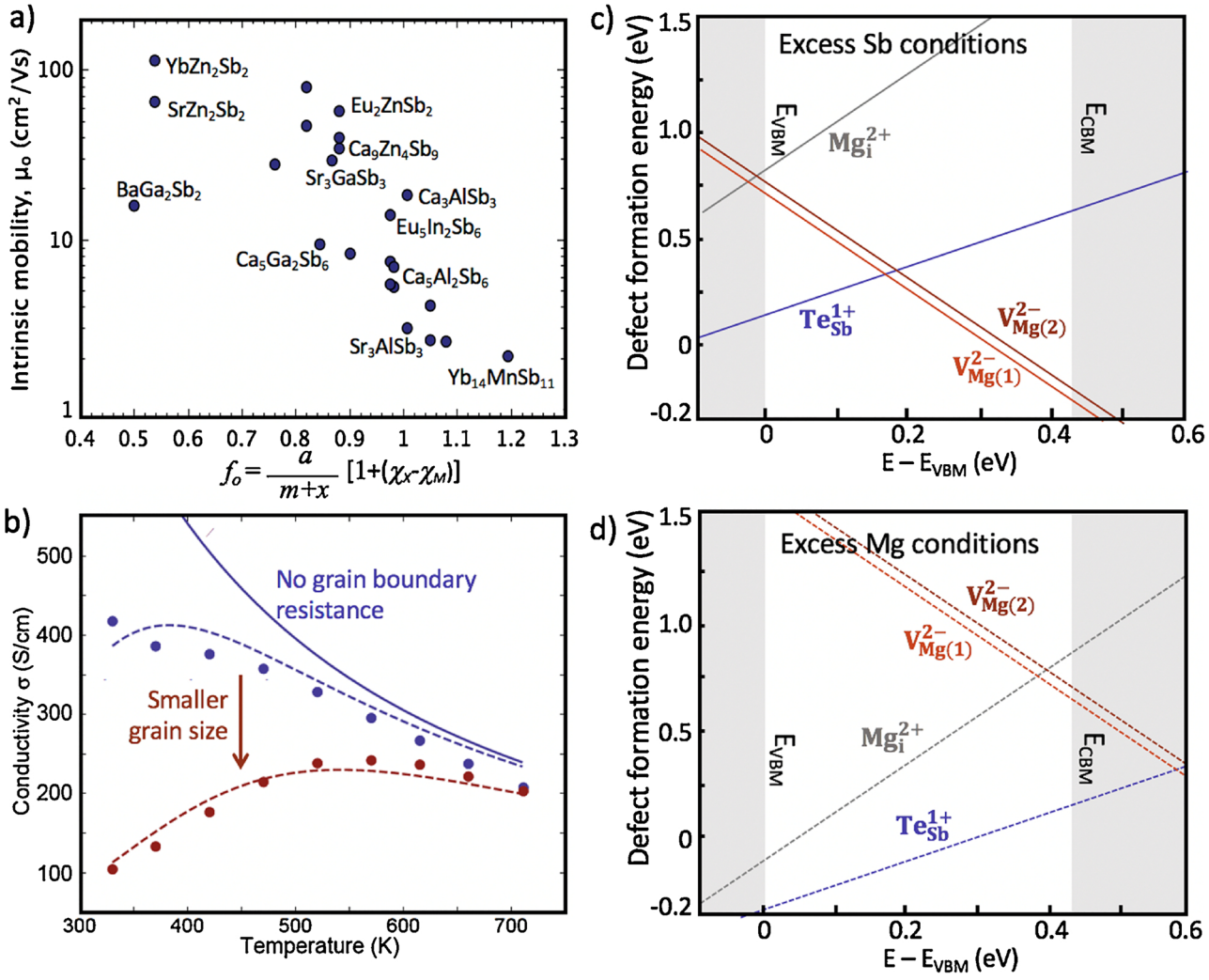

Fig. 18. a) The intrinsic electronic mobility of *p*-type $A_aM_mX_x$ Zintl phases tends to be lower in compounds with more cations (large a), or having polyanions with highly polar bonds (large electronegativity difference). b) Processing changes such as higher pressing temperatures can lead to higher σ by decreasing the resistivity of grain boundaries, adapted from Ref. [397]. c)–d) *n*-type doping can be facilitated by cation- excess synthesis conditions, which leads to lower formation enthalpy for donor-type defects in Mg_3Sb_2. [398].

$Ca_5In_2Sb_6$, Sr_3GaSb_3) [386], compounds with ribbon-like structures with partially-filled interstitial sites ($Yb_9Mn_{4.5}Sb_9$) [387,388], layered compounds ($CaMg_2Bi_2$ [389], $SrZnSb_2$) [390], tunnel-forming compounds ($BaGa_2Sb_2$ [391], $KGaSb_4$ [392]), and compounds with isolated polyanions ($Yb_{14}MnSb_{11}$ [371], $Yb_{11}GaSb_9$ [393]).

Achieving high zT is a balancing act that necessitates materials with light carrier effective mass, high band degeneracy [63], small deformation potentials (reduced electron-phonon scattering) [177], and low, ""glass like" κ_{ph}. Most of the Zintl compounds listed above have succeeded on the basis of their intrinsically low κ_{ph} as well as their excellent stability at high temperature (i.e., they benefit from the T in zT). The low κ_{ph} in Zintl phases has often been attributed to their large unit cells [394], which in turn lead to complex phonon dispersions, low average group velocity, and ample channels for phonon- phonon scattering. To some degree, however, this simple explanation has been challenged by recent examples of low κ_{ph} ($1.5\ W\ m^{-1}\ K^{-1}$) in relatively simple compounds such as Mg_3Sb_2 [395], which forms the $CaAl_2Si_2$ structure type with only 5 atoms per unit cell (see Fig. 17). Mg_3Sb_2 and Mg_3Bi_2 were found to have much lower κ_{ph} than other compounds with the same structure type, despite their lower density [396]. This anomalous behavior is attributed to strongly anharmonic bonding arising from the undersized Mg cations in the octahedral site, which lead to weak, unstable interlayer bonding.

In Zintl phases, the primary barrier to achieving high zT typically lies in the electronic behavior. Most thermoelectric Zintls phases reported to date are p-type and optimization of the p-type carrier concentration is usually straightforward. p-type doping can be accomplished either by aliovalent doping (e.g., Mn^{2+} on the Al^{3+} site in $Yb_{14}MnSb_{11}$, Zn^{2+} on the In^{3+} site in $Ca_5In_2Sb_6$ [399]) or by exploiting intrinsic acceptor-type defects [400]. For example, alloying with isoelectronic elements on the A site in $A_{1-x}Zn_2Sb_2$ compounds has been used to control the vacancy concentration, thus optimizing zT [385,389,401–404]. Unfortunately, low mobility is a common feature of p-type Zintl phases, an attribute that can be at least *partly* attributed to their salt-like, ionic character. To quantify the degree of salt-like nature of a given $A_aM_mX_x$ compound, we consider the ratio of cations to anions, given by $a/(m + x)$, and the polarity of the bonds in the polyanion, measured by the difference in electronegativity, $\chi_X - \chi_M$, between the anions, M and X. Using these simple indicators, it was found that the intrinsic mobility of Zintl thermoelectrics, evaluated using high temperature Hall mobility data within a single band model, tends to be lower in the more salt-like, ionic compounds.

An additional factor that impacts the electronic mobility - particularly at lower temperatures - is the air sensitivity and tendency of the compound to form resistive phases at the grain boundaries. This leads to mobility and σ that are very low at room temperature, and increase with increasing temperature. This is shown in Fig. 18b), which compares a large-grained (5–20 μm) small-grained (0.5–2 μm) Mg_3Sb_2 sample [397], and similar behavior has been observed in many other Zintl phases, including Ca_3AlSb_3, Sr_3GaSb_3, $YbZn_2Sb_2$ [376,377,405]. Low mobility due to grain boundary resistance is, fortunately, not necessarily an inherent problem, but one that can typically be improved by processing modification, leading to large improvements in the average zT (Fig. 19).

A recent high-throughput investigation by Ortiz et al. suggests that electron transport is more favorable than hole transport in the vast majority of known Zintl phases [409,410]. This arises mainly from lighter band mass in the conduction bands. However, because Zintl phases tend to form acceptor-type defects, as demonstrated by Lasse et al. [411], n-type doping has only been achieved in a limited number of compounds [392]. Tamaki et al. recently highlighted the value of controlling the defect formation enthalpies by modifying the synthesis conditions. This is illustrated for Mg_3Sb_3 in Fig. 18c and d, which compares the formation energies of Mg interstitials (Mg_i), Mg vacancies ($V_{Mg(1)}$ and $V_{Mg(2)}$), and Te on the Sb site (Te_{Sb}) using either Mg-excess or Mg-deficient synthesis conditions. Use of excess Mg during synthesis facilitates n-type doping with Te on the Sb site, leading to the highest zT values found in any Zintl phase (Te-doped $Mg_3Sb_{1.5}Bi_{0.5}$ with $zT = 1.6$, $\kappa_{ph} = 0.8$, $PF = 12\ \mu W\ cm^{-1}\ K^{-1}$) [406]. It is likely that this strategy can be successfully applied to other Zintl phases as well. Thus, although Zintl phases have previously been known for their p-type, high- temperature thermoelectric performance, recent results have increasingly challenged those expectations.

2.5. Clathrates

As illustrated by the materials discussed elsewhere in this review, structure and chemical composition play integral roles in determining electrical and thermal transport properties, and therefore thermoelectric performance. This is particularly true for intermetallic clathrates, where the conspicuous geometrical arrangement of the atoms in these materials is directly connected to rather unusual thermal transport, combined with chemical flexibility that produces a wide variety of electrical transport behavior. The term “clathrate” encompasses a

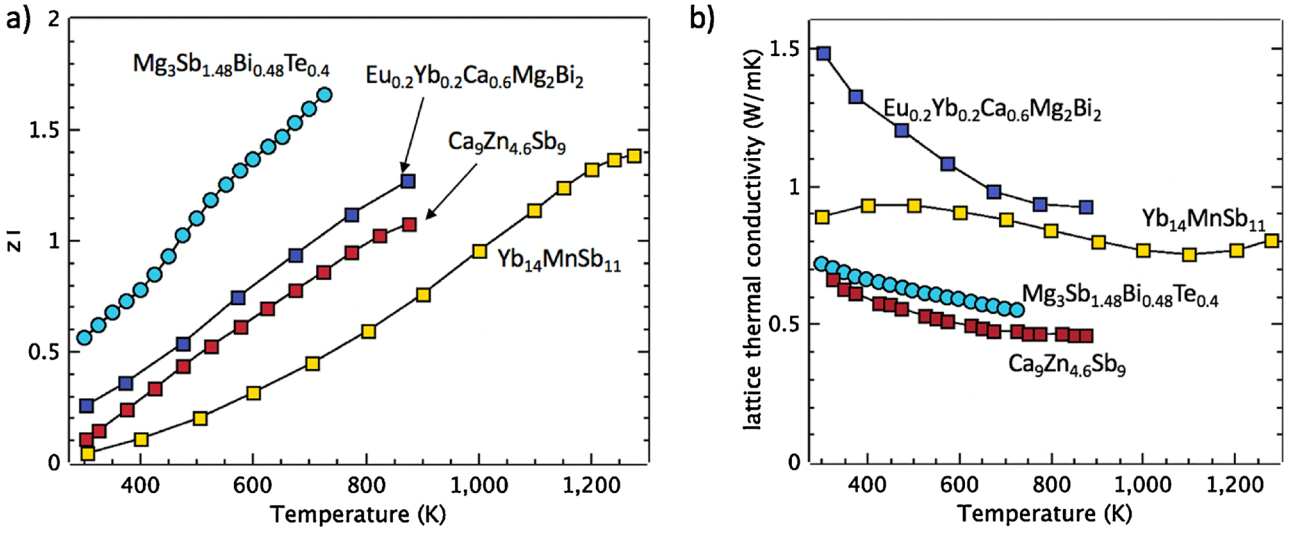

Fig. 19. a) The figure of merit, zT, and b) lattice thermal conductivity, κ_{ph}, of selected Zintl phases from Refs. [374,406–408]. Square symbols are p-type samples, circles are n-type samples.

diverse collection of inclusion compounds classified by a common basic structural feature: a host framework of one species that can encapsulate atomic or molecular guests of another [412]. The clathrate materials of interest for thermoelectric applications, however, comprise a much smaller subset of this vast collection of crystalline guest-host solids. The terms *inorganic* and *intermetallic* clathrates are often used interchangeably (if perhaps somewhat imprecisely) to describe those compounds in which covalently bonded atoms, usually tetrahedrally coordinated, form relatively rigid frameworks comprised of face- sharing coordination polyhedral that can encapsulate various guest atoms [17,360,413–416,701]. There are a variety of different possible structure types in which clathrate compositions may crystallize, each with characteristic polyhedral cages from which the framework is geometrically built [17,360,413–417]. However, most of the known compounds adopt structure types I, II, VIII, or IX with ideal structural formulas G_8 $[E_{46}]$, $G_{24}[E_{136}]$, $G_8[E_{46}]$, and $G_6[E_{25}]$, respectively (G = guest atom, E = framework atom). Shown in Fig. 20a, the type I clathrate crystal structure (and its structural variants) is by far the most frequently represented. Most inorganic clathrate structure types are cubic or pseudo-cubic, so that anisotropy effects in the polycrystalline materials used in thermoelectric modules are of little concern.

The four-coordinated bonding environment for the framework atoms is quite similar to that found in the diamond-structured allotropes of carbon, silicon, germanium, and tin, thus the group 14 elements are often the main constituents of the framework (though carbon clathrates have yet to be synthesized). The crystal chemistry of many ternary and multinary clathrate compositions can be rationalized using Zintl concepts (see Section 2.4) [360], in which framework substitution and/or vacancies accommodate the excess electrons formally transferred to the framework from the guest atoms (or *vice versa* in the case of the so-called "inverse" clathrates) [702]. Since the effective "free space" radii of the framework cages are often large compared to the ionic radius of the guest, the guest atoms typically undergo large amplitude thermal motion, commonly termed *rattling*. This is a key feature of these materials and has important consequences on the phonon heat transport and thermoelectric performance of clathrates.

The first known intermetallic clathrates were the binary type I Na_8Si_{46} and type II Na_xSi_{136} clathrates ($0 < x < 24$), both discovered in the 1960s [418], only a few years after the corresponding crystal structure of the analogous gas hydrates (ice clathrates) had been solved [419]. Binary germanium-based compositions were also reported a short time later [420]. As of 2018, nearly 60 years after the pioneering work of Cros, Pouchard, and Hagenmuller [418,420], close to 300 distinct inorganic/intermetallic clathrate compositions (excluding clathrate hydrates and clathrasils) have been experimentally synthesized (Fig. 21a), including a growing number of compositions completely lacking group 14 elements. The geometrical arrangements of atoms in the various clathrate structure types permit rich chemical diversity: nearly half of the stable elements in the periodic table are now known to be clathrate forming [17,360,413–418,421,701,702]. The remarkable chemical flexibility of these structure types is one of the reasons inorganic clathrates continue to be actively investigated for their potential as thermoelectric materials, with new compositions still being discovered at an impressive pace (Fig. 21a). This chemical flexibility also allows for a wide variation of electrical transport properties, with clathrates from good metals to semiconductors to semi-insulating materials prepared by adjusting the guest and framework constituents and content [17,360,413–418,701,702].

Although they do not exist naturally, the majority of known intermetallic clathrates are thermodynamically stable phases that can be prepared by conventional preparation routes such as direct reaction of the elements. Many of the intermetallic clathrates that are of interest for thermoelectric applications are congruently melting compounds and can thus be prepared from the melt [416]. Other compositions, although stable, do not melt congruently, while others still are only thermodynamically metastable [416]. A wide variety of synthetic routes have therefore been used to synthesize clathrate materials depending on the composition, including direct melting, flux growth, Bridgman method, Czochralski method, thermal decomposition, spark plasma sintering, high-pressure/high-temperature reactions, as well as novel precursor-based approaches that have been developed to access compositions that cannot be prepared by conventional methods [416]. Notwithstanding metastable compositions, the thermal stability of thermoelectric clathrates is relatively good. As expected from the strong Si-Si bond energy (226 kJ/mol), the melting points of the stable silicon-based clathrates are the highest, often in excess of 1200 K [417]. Since the overall thermal and chemical stability of clathrates is very much dependent on the composition, this, in conjunction with the temperature range of optimal thermoelectric performance, ultimately determines the temperature range of potential application.

As reflected in Fig. 21a, intermetallic clathrates attracted relatively limited research interest from their discovery in the 1960s up until about 1995. This changed, however, with two important developments in the 1990s: (i) the discovery of superconductivity at 12 K in $Na_2Ba_6Si_{46}$ [422], and (ii) Glen Slack's introduction of the *phonon-glass electron-crystal* design concept for thermoelectric materials [39,423]. Slack proposed that open-structured framework semiconductors with loosely bound *guest* atoms should have very low κ_{ph}, perhaps even approaching their theoretical minimum thermal conductivities [424,425], and might prove to be good candidates for thermoelectric applications. In particular, he noted that *phonon-glass electron-crystal* behavior might be found in ternary intermetallic clathrates with charge balanced compositions, as these compounds were expected to be semiconductors from simple electron counting principles [426].

At the time of Slack's proposal that intermetallic clathrates should receive a close look as potential thermoelectric materials, there were about sixty or so different intermetallic clathrate compositions known, a few of which might be expected to be semiconductors, but little to no thermoelectric characterization had been performed. In 1998, Nolas, Slack, and coworkers reported the first systematic thermoelectric studies on the ternary type I clathrate $Sr_8Ga_{16}Ge_{30}$ [427]. The results bolstered Slack's hypothesis: the thermal conductivity of $Sr_8Ga_{16}Ge_{30}$ is not only very low ($\sim 1\ W\ m^{-1}\ K^{-1}$ at room temperature), but the lattice contribution κ_{ph} literally exhibits the telltale temperature profile characteristic of a glass, even including the universal T^2 dependence down to the millikelvin temperature range [428]. Moreover, $Sr_8Ga_{16}Ge_{30}$ is indeed a semiconductor with relatively good values for both α and σ, and the electrical transport properties can also be optimized with the carrier concentration by slightly changing the Ga:Ge ratio. A zT value of 0.25 at

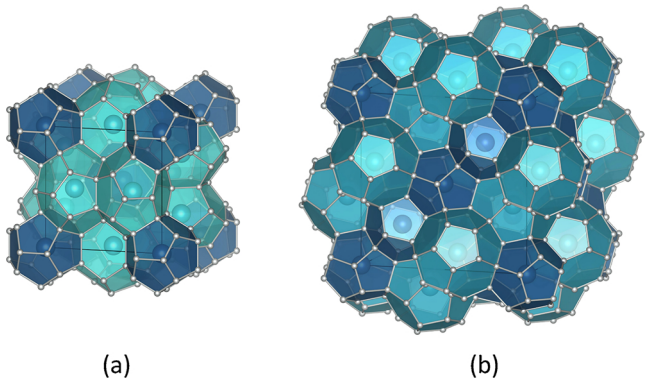

Fig. 20. (a) Type I and (b) type II clathrate crystal structures (space groups $Pm\bar{3}n$ and $Fd\bar{3}m$, *respectively*). The framework atoms are shown in silver. The two distinct framework polyhedral that encage the guest atoms in each structure, E20 and E24 for type I or E20 and E28 for type II, are highlighted in dark and light blue, respectively. The guest atoms are represented by the larger spheres located inside the polyhedral (for interpretation of the references to colour in this figure legend, the reader is referred to the web version of this article).

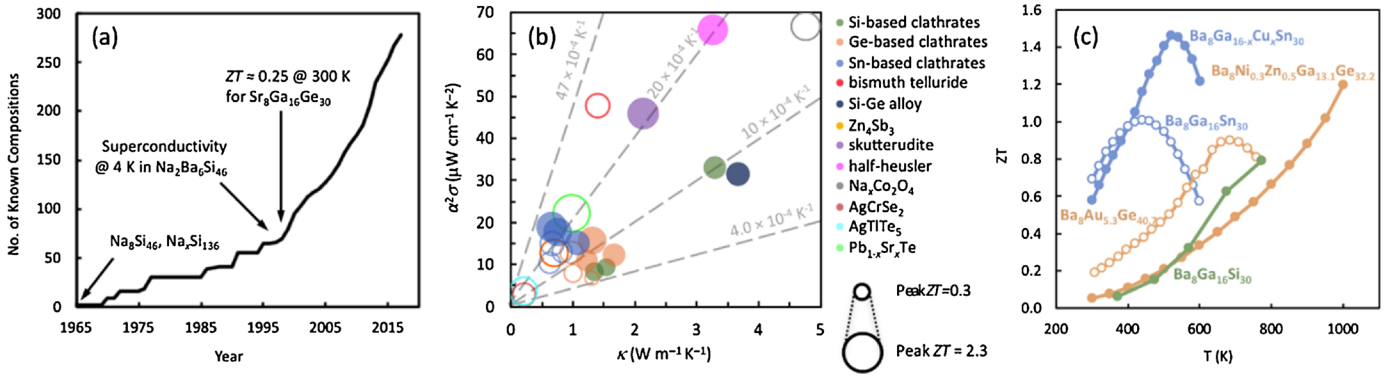

Fig. 21. (a) Number of known inorganic/intermetallic clathrate compositions as a function of year, from the discovery of Na_8Si_{46} and Na_xSi_{136} ($0 < x < 24$) to the present. A distinct composition is defined as a clathrate formed by a distinct set of elements (compositions with different ratios of the same elements are not counted as distinct). Clathrate hydrates and clathrasils are not included. (b) $\alpha^2\sigma$ vs. κ for several intermetallic clathrates [443–455] and other high-performance thermoelectric materials [456]. The size of each data point is proportional to the maximum (peak) zT. Selected curves of constant Z are indicated by the gray dashed lines. Filled circles correspond to *n*-type materials, whereas open circles correspond to *p*-type materials. Although zT at the average temperature of operation is more a more meaningful performance metric, maximum zT is more readily compared among different materials. (c) zT vs. temperature for several high performance thermoelectric clathrate.

300 K was obtained, with higher values projected for elevated temperature [427]. Shortly thereafter, Kunetsov et al. published the first thermoelectric measurements above room temperature for $Ba_8Ga_{16}Ge_{30}$, $Sr_8Ga_{16}Ge_{30}$, $Ba_8Ga_{16}Si_{30}$, and $Ba_8Ga_{16}Sn_{30}$, further corroborating the potential of clathrates for thermoelectrics, with estimated zT values in excess of 0.8 at elevated temperature in un-optimized compositions [429]. The remarkably good thermoelectric performance and glasslike thermal conductivity sparked increased scientific interest in intermetallic clathrates that continues today (Fig. 21a).

In the context of thermoelectrics, most experimental and theoretical work on clathrates in the past 20 years has been motivated by two primary objectives: (i) understanding the microscopic mechanisms for very low and sometimes glasslike κ_{ph}, and (ii) finding new clathrate compositions that have even better thermoelectric performance than those currently known. The former goal is important from the perspective of fundamental science but also feeds into the design of new high performance thermoelectric materials with very low κ. It should be noted that not all intermetallic clathrates have glasslike κ_{ph} – some have a temperature dependence that is more similar to that of a conventional crystal [428]. Nonetheless, the κ_{ph} of intermetallic clathrates, especially above room temperature, is universally low [416]. Though numerous theoretical and experimental studies have unequivocally established the importance of the lattice dynamics associated with the weakly bonded guest atoms in the thermal transport, the fundamental mechanisms for the unusual low temperature κ_{ph} observed in clathrates continue to be investigated and debated [414,417,421,423,425,430,431]. In particular, a symmetry avoided crossing in the phonon dispersion due to the interaction of the low-energy guest modes with the framework acoustic modes plays an important role. This avoided crossing (or anti-crossing) of guest and framework phonon branches was first observed in theoretical lattice dynamics calculations [432] and eventually in experimental single crystal inelastic neutron scattering [433]. Nevertheless, the mechanisms invoked to describe the glasslike thermal transport at low temperatures and generally low κ_{ph} in clathrates have been many and varied, including resonant phonon scattering of the heat carrying acoustic phonons on the guest atom vibrational modes [428], reduced phonon velocities due to the avoided crossing produced by the guest modes [433], effects associated with localization of propagative framework phonons due to the guest-host coupling [434–437], scattering on tunneling states associated with guest atom positional disorder [431], among others [438,439]. One challenge to unraveling the microscopic mechanisms of the thermal transport in clathrates is that the growing body of theoretical and experimental work has focused on a variety of different clathrate compositions. Furthermore, nominally similar compositions can show very different κ_{ph}, which can even depend on the charge carrier type [431]. It is likely that different mechanisms may be at play to different extents in the variety of compositions that have been studied, making generalizations nontrivial. Despite wide variation in the low temperature thermal transport, a picture that rationalizes the universally low κ_{ph} of intermetallic clathrates at temperatures above 300 K (where the best thermoelectric performance is observed) is emerging: the large number of atoms in the unit cell, phonon localization and depressed Debye temperature due to the guest-framework interaction (avoided crossing effect), and overall enhanced anharmonic phonon-phonon scattering can significantly reduce the heat flow in clathrates [436,437,440–442]. Although the details and understanding of the influence of the unusual guest-framework interaction on the κ_{ph} of clathrates continue to be refined, one of the most important lessons learned from intermetallic clathrates is that the lattice dynamics and thermal transport in a crystal can be engineered through structure and chemical bonding while maintaining good electrical properties. Indeed, this was the crux of Slack's original *phonon-glass electron-crystal* concept [39].

Fig. 21b shows a plot of $\alpha^2\sigma$ vs. κ at the temperature of maximum zT for selected silicon [443–445], germanium [446–451], and tin-based intermetallic clathrates [452–455], along with several other high-performance materials [456]. The size of each data point is proportional to the value of the maximum observed zT. Since $z = \alpha^2\sigma/\kappa$, lines of constant slope on this graph correspond to a constant value of z. This type of plot allows the power factor, thermal conductivity, z, and zT of different materials to be simultaneously compared, allowing the electrical and thermal transport contributions to high zT to be evaluated. It is clear from Fig. 21b that the high zT values of most intermetallic clathrates originate in very low κ, whereas on average the $\alpha^2\sigma$ values are modest in comparison to materials such as Bi_2Te_3, skutterudites, half-heuslers, and $Na_xCo_2O_4$. From the perspective of increasing zT, the continued exploration of new compositions in the last several years, in particular tin-based compositions, has been fruitful [417]. zT as high as 1.5 has been reported in *n*-type $Ba_8Ga_{16-x}Cu_xSn_{30}$ single crystals [454], and several distinct clathrate compositions with zT near or greater than unity have now been identified. Tin clathrates benefit from exceptionally low κ_{ph}, in part due to the heavier average atomic mass of the tin-based clathrate framework. Illustrated in Fig. 21b, higher power factors have also been observed in a number of *n*-type tin clathrates, also contributing to higher zT values. Although the power factors still remain relatively low in comparison to other high-performance materials (Fig. 21b), it is worth noting that tin-based clathrates have some of the highest z values of any known thermoelectric material. In discerning the physical reasons underlying improved thermoelectric

performance, it can be instructive to evaluate z as opposed to zT, since high T inherently favors high efficiency. Gaining an understanding of the clathrate structure-property relationships that produce the good balance of electrical and thermal transport properties (high z), and their similarities and differences with other materials, can feed into the design of better thermoelectrics in general. It is also worth noting that good thermoelectric performance is found in both *n*-type and *p*-type tin and germanium clathrate compositions, a balance that is less common in other classes of thermoelectric materials [456].

Due to their high chemical and thermal stability, low density, and low cost (especially relative to Ge-based compounds), silicon clathrates have been attracting increasingly more attention in the past several years [457]. Indeed, it has recently been demonstrated that Si-based ternary clathrate compositions comprised entirely of low density, earth abundant, and non- toxic elements can be prepared [458,459]. To date, however, the thermoelectric performance of most silicon clathrates remains inferior to that of the best germanium and tin-based materials. Although silicon clathrates also have inherently low κ_{ph} [442], their power factors so far are also relatively low (Fig. 21b). In part, this can be attributed to the relatively high carrier concentrations found in most silicon clathrates, which are also mostly observed to be *n*-type [417]. While there may be less inherent chemical flexibility in silicon clathrates than in the germanium and tin compounds, making it more difficult to optimize the carrier concentration or tune the material *n*- or *p*-type, some compositions with low carrier concentrations such as $K_8Al_8Si_{38}$ have recently been reported [458]. While the highest zT values in silicon clathrates have yet to exceed 0.8 [460], significantly higher values might be achieved if the carrier concentrations in these materials can be reduced to optimal values [444]. Recent results suggest the carrier density in *n*-type silicon clathrates can indeed be adjusted with composition [461]; further work in this area may yield earth-abundant silicon clathrates with better thermoelectric performance.

Since the lattice thermal conductivity of intermetallic clathrates appears to be universally low, significantly better thermoelectric performance in clathrates will likely require novel approaches to increasing the power factor. Such approaches have begun to be explored. Introducing strong electron correlation effects by incorporating rare earth guest atoms has been reported to enhance α at a given carrier concentration in $Ba_8Au_xSi_{46-x}$ [462]. Exceptionally large power factors were recently predicted for silicon-based type VIII clathrates at unusually high doping levels [463], though this material has yet to be synthesized experimentally. These encouraging results indicate that continued focus on understanding the electronic structure of thermoelectric clathrates, including identification of structures and compositions that have the best electronic properties and ways to manipulate electronic structure and carrier scattering through chemical substitutions, could yield significantly improved thermoelectric performance of clathrates.

2.6. Heusler compounds

The so-called Heusler compounds were discovered in 1903 by Fritz Heusler [464]. Heusler compounds adopt the elemental formula X_2YZ. Certain compounds of this materials class are ferromagnetic, even though they do not contain any ferromagnetic elemental components. Due to their magnetic properties, these materials are of high importance in the field of spintronics [465–467]. The Half-Heusler (HH) compounds are a variant of the Heusler compounds with the elemental formula *XYZ, i.e.* they contain vacancies on the *X* site. HH materials consist of three interlaced face-centered cubic sub-lattices (see Fig. 22left). Many HH materials are characterized by narrow band gaps [468,469], which makes them suitable for thermoelectric applications [470,471]. Nevertheless, only a few HH compounds have been studied extensively for their thermoelectric properties, suggesting that there is still a lot of room for advanced materials design in this area.

HH compounds contain elements that have high melting point such as Hf (2504 K), Zr (2128 K), Ti (1941 K), Ni (1728), or Co (1768 K), in combination with elements that have relatively low melting point such as Sn (505 K) or Sb (904 K) (see Fig. 22 right). Therefore, for synthesizing HH compounds, a high temperature alloying method is necessary. Usually, this can be achieved by weighting the constituting elements in stoichiometric amounts, followed by arc-melting in an Ar-atmosphere for at least three times. Subsequently, the samples are crushed and re-melted, to ensure the homogeneity of the samples. Other preparation techniques for HH compounds are inductive heating [472], solid state reaction [473] or new preparation techniques such as melt spinning [474] or spark plasma sintering (SPS) [475,476]. Usually, an additional heat treatment is necessary for all samples to obtain the ordered $C1_b$ structure and to eliminate possible secondary phases that could occur during the melting process. For annealing, the ingots are sealed in evacuated quartz ampoules and heated to temperatures

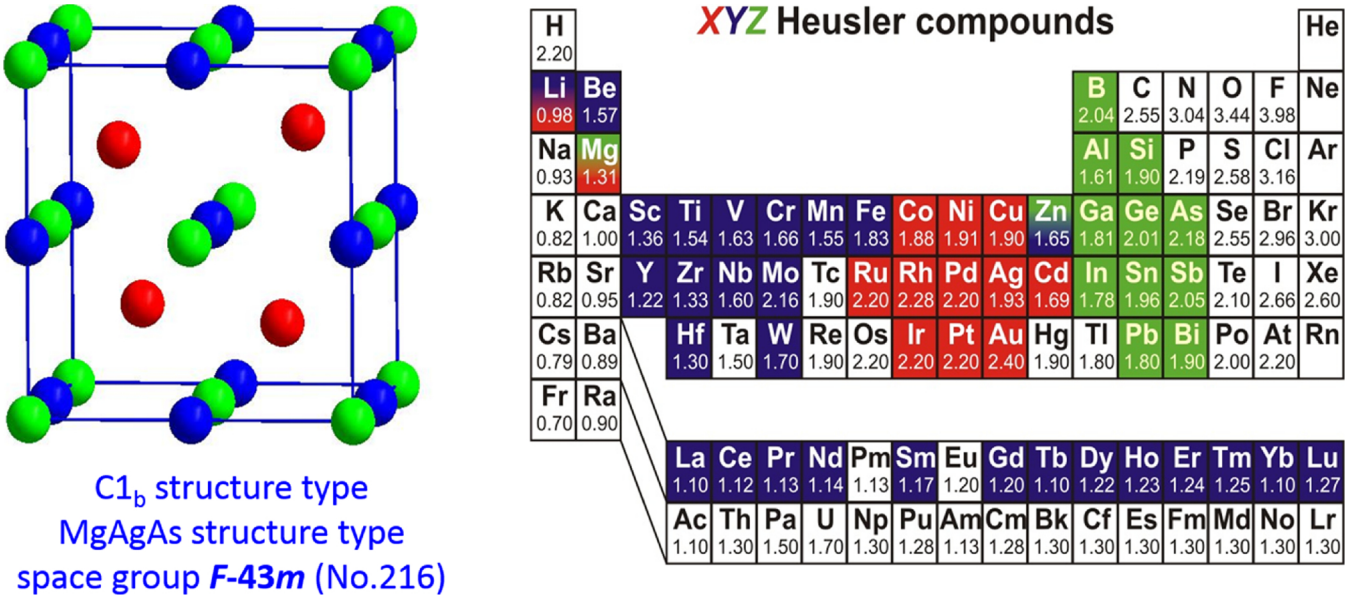

Fig. 22. Crystal structure of a HH compound (left). Periodic table of the elements. The huge number of HH materials can be formed by combination of the different elements according to the color scheme (right).

around 1173 K–1323 K for 3–7 days, with subsequent quenching into ice water. An important task for the ongoing thermoelectric research is to identify the minimum necessary annealing time while preserving a high figure of merit zT, in order to lower the production cost for potential industrial applications. Their mechanical and thermal stability is exceptional in comparison to the commonly used thermoelectric materials (Hardness ≈ 900 VH1), which is important for the robustness of the devices in most applications [477]. For more details about all the possibilities, opportunities, and challenges concerning the production of HH compounds the reader is referred to the Ref. [478]. A relatively new approach for synthesizing HH compounds is the energy and time-efficient process involving solid-state preparation in a commercial microwave oven [479].

A great advantage of HH compounds is the possibility to substitute different elements on each of the three occupied *fcc* sublattices individually in order to optimize the thermoelectric properties. For example, it is possible to alter the number of charge carriers by doping on the Z position, while simultaneously introducing disorder by doping on the X and Y position, which results in mass fluctuations that can decrease κ. The most attractive properties of Half-Heusler materials for thermoelectrics are their high α, up to ~ 300 μV K^{-1} at room temperature, and their high σ (~ 10^3 to 10^4 S cm^{-1}) [480–484]. The only drawback of HH compounds in respect to thermoelectrics is their relatively high κ, which can be as high as 10 W m^{-1} K^{-1}.

Among the possible HH compounds, *n*-type *M*NiSn and *p*-type *M*CoSb (M = Ti, Zr, Hf), *R*FeSb (R = V and Nb) and some $L2_1$ Heusler compounds have received attention for thermoelectric applications due to their high potentials for exceptional zT values. Research has therefore mainly focused on improvement of these ternary intermetallic compounds, which are reviewed in detail in the following sections.

2.6.1. MNiSn and MCoSb (M = Ti, Zr, Hf)

In the first experiments, Aliev et al. performed resistivity measurements on *M*NiSn (M = Ti, Zr, Hf) and classified the compounds as narrow-band-gap semiconductors with band gaps of 0.12 eV, 0.18 eV, and 0.22 eV, respectively [485]. Shortly after, it was recognized that the compounds also exhibit large Seebeck coefficients, making them promising candidates for thermoelectric applications [486]. In an effort to reduce the lattice thermal conductivity of the compounds, Hohl et al. investigated alloys of TiNiSn, ZrNiSn, and HfNiSn [487]. It was found that $Zr_{1-x}Hf_xNiSn$ alloys form solid solutions with a reduced thermal conductivity. The power factors were not affected in a negative manner upon alloying. An interesting study has been performed by Uher et al. [480] who showed that the transport properties of the materials are rather sensitive to annealing treatments. The impact of annealing is especially conspicuous in the lattice thermal conductivity. Uher et al also reported Sb to be an efficient dopant for the tin sites of $Zr_{1-x}Hf_xNiSn$ alloys.

As mentioned above, a general challenge in improving HH compounds is the comparatively high thermal conductivity, which is of the order of 10 W m^{-1} K^{-1}. A common approach to reduce κ is to increase phonon scattering. Hohl et al. [488] reduced κ by a factor of three for different temperatures by introducing disorder on the X-sites in $X_{0.5}X'_{0.5}NiSn$ (X, X' = Ti, Zr, Hf). Substitution of tin by antimony increases both κ and σ [468]. Substitution at the Ni position decreases κ [489]. The composition $Zr_{0.5}Hf_{0.5}Ni_{0.8}Pd_{0.2}Sn_{0.99}Sb_{0.01}$ possesses a figure of merit zT = 0.7 at 800 K [490] and the composition $Hf_{0.75}Zr_{0.25}NiSn_{0.975}Sb_{0.025}$ shows a figure of merit zT = 0.8 at T = 1073 K [491]. The Toyota company (Japan) measured a zT = 0.9 for $Hf_{0.5}Zr_{0.5}NiSn$ at 960 K [492]. Moreover, Toshiba (Japan) reported a maximum zT of 1.5 for $Zr_{0.25}Hf_{0.25}Ti_{0.5}NiSn_{0.998}Sb_{0.002}$ at 700 K [493]. However, these high zT values were never reproduced by any other group since the original publication in 2005.

Schwall and Balke managed to reach with a zT of 1.2 a similar high figure of merit as reported by Shutoh and Sakurada in 2005 by keeping the thermal conductivity low [494]. The origin of the exceptional low κ lies in a phase decomposition to Zr/Hf-rich and Ti-rich phases. This decomposition does not significantly influence σ because of semi-coherent interfaces between the three coexisting Heusler phases. These intrinsic properties of the $Ti_{0.5}Zr_{0.25}Hf_{0.25}NiSn_{(1-x)}$ Y_x | Y = Sb, Bi, Te; x = 0-0.006 system show that the Heusler compounds are competitive thermoelectric materials with respect to the transport properties.

Joshi et al. showed that by substituting titanium for hafnium in *n*-type HH compounds $Hf_{0.75-x}Ti_xZr_{0.25}NiSn_{0.99}Sb_{0.01}$ an enhancement of the thermoelectric figure of merit zT at low temperatures can be realized [495]. Another approach to improve the efficiency of thermoelectric materials and generators over a wide working temperature range is the segmentation of thermoelectric materials [496].

Wu et al. [497] reported an iron-doped TiCoSb with the elemental formula $TiFe_{0.3}Co_{0.7}Sb$, which reaches a maximum zT of 0.42 at 743 K. Sekimoto et al. [498] presented a tin- doped ZrCoSb with the composition $ZrCoSb_{0.9}Sn_{0.1}$ possessing a maximal zT = 0.45 at 958 K. The *p*-type semiconductors have κ that is 2–3 times higher than that of the *n*-type materials and therefore the reduction of κ of *p*-type materials to reach the level of the *n*-type semiconductors (≈ 3 W m^{-1} K^{-1}) seems a very attractive research target. For example, the reduction of κ of

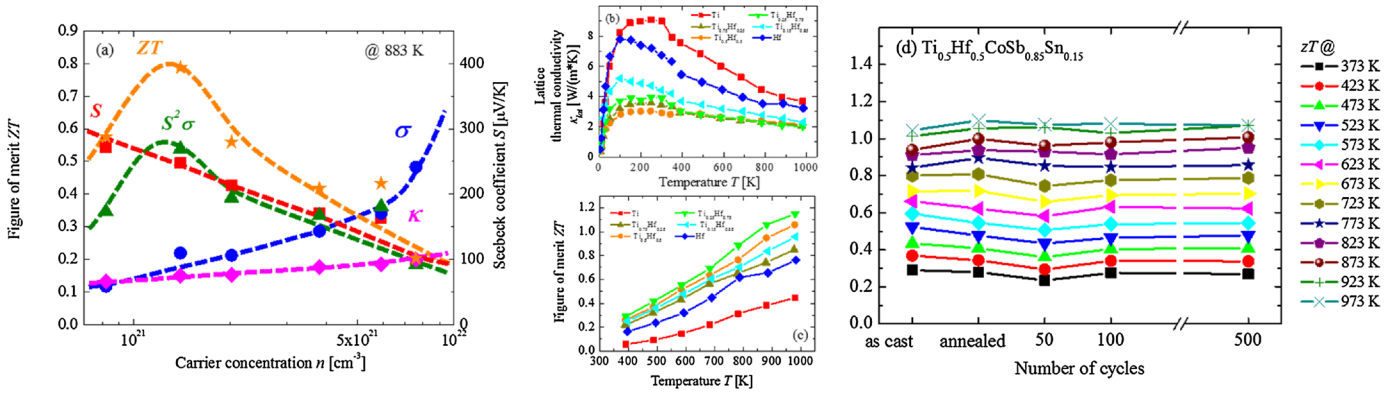

Fig. 23. (a) Thermoelectric properties of $Ti_{0.3}Zr_{0.35}Hf_{0.35}CoSb_{1-x}Sn_x$ as a function of the carrier concentration at 883 K. Plotted are Seebeck coefficients (filled red square in the range from 0 to 450 μV K − 1), electrical conductivity σ (filled blue circle, 0 − 18 × 10^{-4} S m^{-1}), power factors $\alpha^2\sigma$ (filled green triangle, 0–4.5 × 10^{-3} W m^{-1} K^{-1}), thermal conductivity κ (filled pink diamond, 0–18 W K^{-1} m^{-1}), and figure of merit zT (filled orange star, 0 − 0.9). (b) Lattice thermal conductivity k_{ph} as functions of temperature for $Ti_{1-x}Hf_xCoSb_{0.85}Sn_{0.15}$ for the indicated ratios of Ti to Hf. Data up to 350 K were obtained from TTO PPMS measurements, high-temperature data were calculated from LFA measurements. (c) Figure of merit zT as a function of temperature for $Ti_{1-x}Hf_xCoSb_{0.85}Sn_{0.15}$ for the indicated ratios of Ti to Hf. (d) Figure of merit zT as function of number of cycles of the long-term stability performance test - each line represents measurements at constant temperature after the various heat treatment steps (see legend) (for interpretation of the references to colour in this figure legend, the reader is referred to the web version of this article).

$ZrCoSb_{0.9}Sn_{0.1}$ by a factor of 3 without changing the other properties would give a zT as high as 1.2.

Atomic-scale substitution on the various lattice sites of the HH compounds is not the only mean to attain increased phonon scattering. Nanostructures at an appropriate scale can also be generated and fine-tuned by suitable thermal treatments, based on a thorough knowledge of the relevant phase diagrams. Disproportionation reactions, as recently shown in multicomponent chalcogenide compounds, while retaining the initial crystal structure of the components, can give rise to nanostructured composites with a reduced κ and hence enhanced zT [499]. Recently, Yan et al. were able to enhance the zT of *p*-Type HH compound via a nanostructuring approach [475]. They succeeded in achieving grain sizes smaller than 200 nm in *p*-type HH samples with a composition of $Zr_{0.5}Hf_{0.5}CoSb_{0.8}Sn_{0.2}$ by ball milling the alloyed ingot into nanopowders and then hot pressing them into dense bulk samples, resulting in a simultaneous increase in α and a significant decrease in κ, which led to a 60% improvement in peak zT from 0.5 to 0.8 at 973 K. For recent reviews about nanocomposite HH materials see references [478,500,501].

Using the approach of introducing stronger phonon scattering by larger differences in atomic mass and size, Yan et al. were able to increase zT to 0.9 at 973 K in *p*-type HH compounds $Hf_{1-x}Ti_xCoSb_{0.8}Sn_{0.2}$ [502]. Very recently, it has been shown that an intrinsic phase separation can also be introduced in the *p*-type Heusler systems (Ti/Zr/Hf) $CoSb_{0.8}Sn_{0.2}$ and (Ti/Zr/Hf) $CoSb_{0.85}Sn_{0.15}$, analogues to the *n*-type system [503]. Two concepts were successfully applied to improve the thermoelectric properties of the *p*-type TiCoSb system (see Fig. 23a). Starting from $Ti_{0.5}Hf_{0.5}CoSb_{0.8}Sn_{0.2}$, it was shown that phase separation (zT = 0.9 at 983 K [503]) results in thermoelectric properties that are similar to those obtained with a nanostructuring approach involving ball milling [502]. In the second step, the optimization of the carrier concentration led to an improvement of about 25% regarding the figure of merit in $Ti_{0.5}Hf_{0.5}CoSb_{0.85}Sn_{0.15}$, ($zT$ = 1.05) [504]. Based on these two concepts, a fine tuning of the Ti to Hf ratio for optimum phonon scattering in combination with optimum electronic properties, a record zT of 1.2 at 983 K for *p*-type Co-based HH compounds was achieved in a material with the composition $Ti_{0.25}Hf_{0.75}CoSb_{0.85}Sn_{0.15}$ (see Fig. 23b–c) [504]. Further, a successful approach to decrease the device cost performance ratio ($ per W) by fabricating Hafnium-free high zT half-Heusler materials was recently published [505]. A calculation done by B. Balke using world market price in the order of metric tons of the raw elements results in a decrease of about 90% for the Hf-free half-Heusler materials.

The recovery of industrial and automotive waste heat are possible fields of applications of thermoelectric devices based on half-Heusler compounds in the mid-temperature range. In both cases, the operation conditions impose thermal stress upon the material. For example, a thermoelectric generator integrated into an automotive exhaust pipe operates in the temperature range from 373 K to 973 K, while being heated and cooled multiple times during the driving process. Therefore, Rausch et al. investigated the long-term stability of three state-of-the-art HH *p*-type materials under thermal cycling conditions [506]. Structural investigations and measurements of the thermoelectric properties were performed on the as- cast and annealed samples as well as after 50, 100 and 500 heating and cooling cycles. The material $Ti_{0.5}Hf_{0.5}CoSb_{0.85}Sn_{0.15}$ showed the best and most stable performance under thermal cycling conditions (see Fig. 23d). The intrinsic phase separation, which is responsible for the outstanding thermoelectric properties, withstands the repeated heating and cooling cycles. $zT > 1$ at 973 K is reached reliably even after 500 heating and cooling cycles. Assuming an average 1 h of car usage per day, the 500 cycles correspond to three years of the car lifetime. In combination with the high mechanical strength of the material and the broad maximum of PF from 593 K to 973 K, this is very desirable for the fabrication of thermoelectric modules for applications in the mid- temperature range.

Fig. 24 shows zT values of *n*- and *p*-type state-of-the-art Half-Heusler materials discussed above and the with the element-specific EDX mappings of the five constituents of the phase separated $Ti_{0.5}Zr_{0.25}Hf_{0.25}NiSn$ compound the key to the low thermal conductivity and therefore the high zT values of several *n*-type and *p*-type half-Heusler materials.

2.6.2. *RFeSb (R = V and Nb)*

*R*FeSb (*R* = V and Nb) HH compounds, with abundantly available constituent elements, have been recently identified as a promising new class of high temperature TE materials [507–509]. VFeSb was initially studied as an *n*-type TE material possessing large α ($\cong -200\ \mu VK^{-1}$), and high PF ($\cong 4.5 \times 10^{-3}\ Wm^{-1}K^{-2}$) [510]. However, similar to *M*NiSn and *M*CoSb systems, *R*FeSb compounds have an intrinsically high κ_{ph} ($\cong 10\ W^{m-1}K^{-1}$ at 300 K) [510,511]. Earlier studies have focused on improving the TE performance of *n*-type VFeSb by alloying [511] or nanostructuring [512,513], but only a marginal improvement

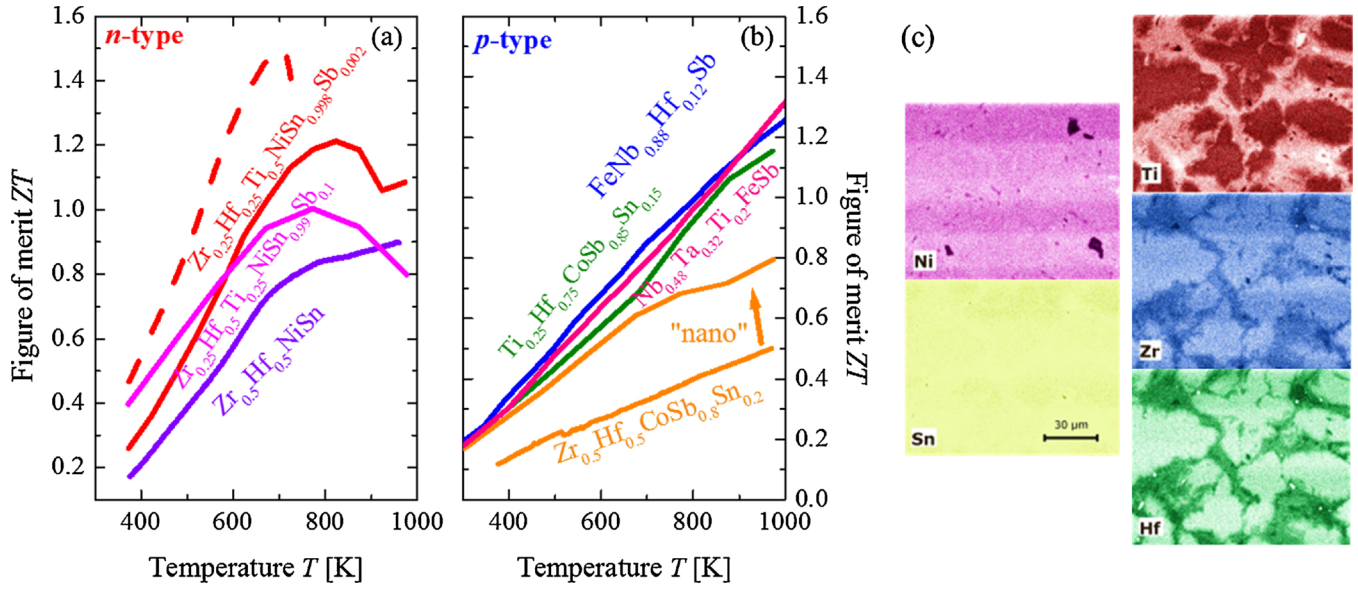

Fig. 24. (a) + (b) zT values of *n*- and *p*-type state-of-the-art Half-Heusler materials. (c) Element- specific EDX mappings of the five constituents of the phase separated $Ti_{0.5}Zr_{0.25}Hf_{0.25}NiSn$ compound with brightness proportional to the concentration. For more details see Ref. [484].

in peak zT was realized (≅0.33 at 650 K) [514]. Recently, *p*-type (V,Nb)FeSb solid solutions were experimentally found to exhibit high TE performance as *p*-type TE materials because of high band degeneracy in the valence band, and reached an impressive zT of ≅0.8 at 900 K using a high content of Ti as a dopant [515]. Subsequently, an even higher zT of ≅ 1.1 at 1100 K was achieved in Ti-doped NbFeSb HH compounds via a band engineering approach to reduce the band effective mass [516]. Furthermore, the doping of the more efficient and heavier Hf in NbFeSb achieved an exciting zT of ≅1.47 at 1200 K [517]. This improvement resulted not only from the enhancement of *PF* (weaker alloy scattering), but also from the reduction of κ_{ph} (stronger mass fluctuation). More recently, hierarchical phonon scattering was also demonstrated to be an effective way to improve the TE properties of the NbFeSb heavy band system with relatively low mobility [518]. Very recently, Yu et al. reported on the successful synthesis of Ta alloyed $(Nb_{1-x}Ta_x)_{0.8}Ti_{0.2}FeSb$ (x = 0–0.4) solid solutions with significantly reduced κ by levitation melting. Because of the similar atomic sizes and chemistry of Nb and Ta, the solid solutions exhibit almost unaltered electrical properties. As a result, an overall zT enhancement from 300 K to 1200 K is realized in the single phase Ta alloyed solid solutions, and the compounds with x = 0.36 and 0.4 reach a maximum zT of 1.6 at 1200 K [519].

2.6.3. $L2_1$ Heusler compounds

Among half-metallic Heusler compounds with the $L2_1$ structure, the family of $TiCo_2Z$ (Z = Al, Si, Ge, Sn) shows unusual transport properties [520,521]. For instance, α remains constant over a wide temperature range above the respective Curie temperature in these materials making them promising candidates for an application in thermocouples due to the linear dependency of the thermovoltage on temperature. Additionally, the working range of applications using these materials can be tuned by changing the valence electron number [522]. The $TiCo_2Z$ system exhibits high α in a metallic system and thus is regarded as a potential material for the combination of half-metallic ferromagnetism and thermoelectric effect in the new research field of spincalorics [523,524].

Another very promising family of $L2_1$ Heusler compounds for TE application is the Fe_2VAl system. Due to the large amount of studies within this system the reader is referred to Refs. [525] and [526] and references therein. For more than a decade now, Nishino and coworkers investigating the Fe_2VAl system for their TE properties because of the possession of a sharp pseudogap across the Fermi level, Fe_2VAl-based compounds have attracted a great deal of interest as a potential candidate for promising thermoelectric materials [527]. Since the DOS of Fe_2VAl sharply changes in both valence band and conduction band sides of the pseudogap, the Seebeck coefficient enhances significantly when the Fermi level shifts slightly due to doping. The doping was carried out into first one of the iron, vanadium, and aluminum sites in Fe_2VAl for the *n*-type materials, and into the iron or vanadium site for the *p*-type materials. More recent studies investigate the influence on co-doping, e.g. on the compounds $Fe_{2-x}V_{1+x}Al_{1-y}Si_y$ and $Fe_{2-x}V_{1+x-y}Ti_yAl$. It could be concluded that a larger Seebeck coefficient with a negative sign can be obtained for the V-rich alloys rather than the V-poor alloys, whilst good *p*-type materials are always derived from the V-poor alloys [525]. A significant enhancement in the Seebeck coefficient with both positive and negative sign can be achieved not only by the Fe/V off- stoichiometry combined with doping but also by the V/Al off-stoichiometry even without doping. For the latter alloys, the peak temperature of the Seebeck coefficient increases up to 600 K, and the maximum power factor is 4.3×10^{-3} $Wm^{-1}K^{-2}$ for *p*-type $Fe_2V_{0.97}Al_{1.03}$ and 6.8×10^{-3} $Wm^{-1}K^{-2}$ for *n*-type $Fe_2V_{1.05}Al_{0.95}$, both of which are higher than those of the half-Heusler compound ZrNiSn and Mg2Si compound [526]. Due to their high κ, only low zT values could be reached, but combining such high power factors with the concept of the phase separation (see above), this material class could become very interesting for the low temperature regime (up to 600 K) for the replacement of tellurium and/or lead containing TE materials in case of EU regulations banning the latter.

As a conclusion of this very lively research, including many different working groups around the world, it is worth noting that the HH compounds fulfill already most of the industrial demands for TE materials, i.e. environment-friendliness, low cost and availability of raw materials, long term stability, producibility in industrial quantity and chemical and mechanical resistance toward high temperatures.

2.7. Metal oxides

Metal oxides show lower thermoelectric performance than conventional thermoelectric materials. There is, however, more to a material than its thermoelectric performance. While the practical use of most traditional thermoelectrics is limited because they thermally decompose, melt, or are oxidized in air at high temperatures (T > 973 K), metal oxides are suitable for high-temperature applications, where most of the waste heat is generated, because of their thermal, structural and chemical stability. In addition, most metals are abundant and cheap, and metal oxides can easily be manufactured in large amounts from cheap precursors by solid state processing or direct synthesis/compaction using SPS.

Most metal oxides are characterized by narrow bands and therefore large effective masses m^*. This leads to carrier mobilities that are two to three orders of magnitude lower than those of chalcogenide homologues or pnictides. Furthermore, the small atomic mass of oxygen, and the strong bonding energy arising from the large electronegativity difference, are responsible for high values of κ. Therefore, they have been considered for long time not compatible with the guidelines governing the choice of a good thermoelectric material.

The discovery of a high *PF* in $NaCo_2O_4$ crystals, made by Terasaki

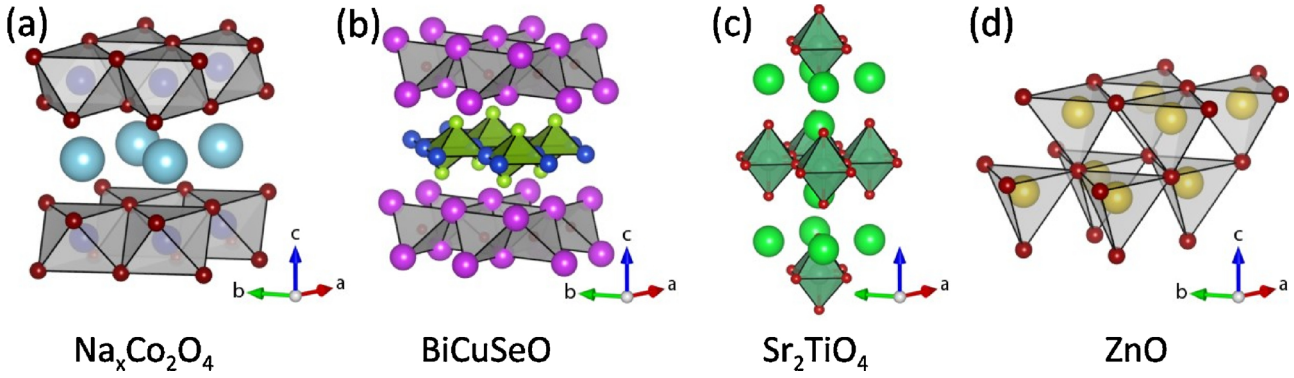

Fig. 25. Crystal structures of the main metal oxides discussed in this section. (a) Layered cobaltites, (b) BiCuSeO, a promising representative of the layered oxyselenides, (c) the strontium titanate, a representative of the Ruddlesden-Popper phases, (d) zinc oxide (wurtzite type). Adapted from ref. [537]. Reprinted with permission, Wiley-VCH, 2016.

et al. [528] in 1997, at 1323 K from Na_2CO_3 and Co_3O_4 in a NaCl flux, was the turning point for metal oxides in thermoelectrics. Ternary oxides A_xMO_2 (A = Na, K; M = Cr, Mn, Co, $0 < x < 1$) [529] have a layered structure consisting of CdI_2-type MO_2 layers and charge- balancing Na^+ or K^+ cations situated randomly in octahedral sites between the layers. Thus, electrons and phonons follow different paths in the layered $NaCo_2O_4$ structure. The electrical transport occurs in the ordered CoO_2 layers, while the disordered Na^+ cations between the layers serve as electronically insulating phonon-scattering regions associated with low thermal conductivity [530].

$NaCo_2O_4$ is the simplest representative of layered oxides [531]. The modular misfit layer structure provides possibilities for tuning the properties by modifying the individual components selectively. A large positive Seebeck coefficient ($\alpha \approx 100\ \mu V\ K^{-1}$) and a high electrical conductivity ($\sigma \approx 500\ S\ m^{-1}$), despite a low carrier mobility, together with a comparatively low κ of $4\ Wm^{-1}K^{-1}$) for $NaCo_2O_4$, lead to zT of 1, which makes $NaCo_2O_4$ and its multilayer congeners competitive with classic thermoelectric intermetallics. The lattice mismatch between the two sublayer systems imposes additional internal stress, which together with the charge reorganization between the CoO_2 and rock salt layers may improve the electronic properties from the thermoelectric perspective. After Terasaki´s report [528], research on oxide thermoelectrics with strongly correlated electron systems and spin fluctuation advanced dramatically, for both *p*- and *n*-type materials. Nevertheless, a gap between their thermoelectric efficiencies still exists, with the *p*-type materials performing better.

Fig. 25 shows the crystal structures of the most promising *p*- and *n*-type materials. Layered cobaltites [529–532] and oxyselenides [533–536] represent the state-of-the-art materials for *p*-type thermoelectric oxides, owing to the combination of building blocks with different composition and symmetry that allow an effective decoupling of the transport properties. The same principle can be somehow applied also to their *n*-type counterparts, where materials related to the Ruddlesden-Popper phase and zinc oxides show great potential. Accordingly, the research on thermoelectric oxides focused mainly on complex layered structures containing conductive sheets with metal-like electronic properties, and interfaces between layers contributing to enhance phonon scattering and thus reduce κ. In the following, these classes of materials are discussed separately.

2.7.1. Layered cobaltites

$NaCo_2O_4$ and $Ca_3Co_4O_9$ are the best performing compounds. The discovery of Terasaki et al. in 1997 [528] marked the starting point of a systematic research in cobaltites for thermoelectrics, which attracted attention because of their layered structures. The effective scattering of phonons ensures low κ ($\approx 2\ Wm^{-1}K^{-1}$). Moreover, cobaltites exhibit good electronic properties that translate in an overall zT exceeding 1. Their outstanding thermoelectric properties arise from the complex structure made of building blocks with different composition that allow a decoupling of the thermal and electrical transport properties. The best materials are alkali or alkaline-earth cobaltites with layered structures. They are characterized by high values of α due to the low spin state of Co^{3+} and Co^{4+}. Using the Hubbard model and applying Heikes' formula [538] to the cobalt oxides, the thermopower appears a function of the degeneracy ratio of Co^{3+} and Co^{4+} (g_3/g_4). The lower spin states of both cations are those that ensure the lowest values of g_3/g_4 and hence the highest values of α. $Na_xCo_2O_4$ is formed by layers of tilted edge-sharing CoO_6 octahedra which provide paths for the conduction of holes, while numerous interfaces, generated by alternating layers of Na, block the phonon transmission. The variation of the cation valence is another factor affecting the thermoelectric properties. This has been confirmed by measurements on the so-called *misfit-layered* alkaline earth cobaltite $Ca_3Co_4O_9$ [539], where a reduction of the oxygen content resulted in an enhanced performance. The crystal structure of $Ca_3Co_4O_9$ is similar to that of $Na_xCo_2O_4$, where CoO_2 layers (CdI_2-like) and rock salt-type Ca_2CoO_3 layers alternate perpendicular to the layer direction. Again, the CoO_2 layers are responsible for electronic conduction, while phonon transport is blocked by interfaces between the layers due to the mismatch of phonon group velocity. The undoped compounds show a power factor as high as $1.5 \times 10^{-4}\ Wm^{-1}\ K^{-2}$ at room temperature [540]. Improvements have been achieved by doping with transition metals (e.g. Fe, Mn) or with Bi, Ba, and Ga. P substitution of Ca or Co with these metals were beneficial for increasing the power factor, Fe doping being most effective. Here, Fe replaces Co in the CoO_2 layer, thereby modifying the electronic structure and increasing the electronic correlation, thereby enhancing both α and σ. The best zT was measured for a composition $Ca_{2.7}Bi_{0.3}Co_{3.9}Fe_{0.1}O_{9+}$, with 0.4 at 973 K [541]. Other alkaline earth cobaltites like Ca_xCoO_2, Ba_xCoO_2, or $Ca_3Co_2O_6$ were prepared, but their application is limited by ρ (up to about $2–3 \times 10^{-4}\ \Omega$*m at 850 K). Only recently, a record zT of 0.74 at 800 K was achieved by partially substituting Ca with the rare earth metal Tb ($Ca_{2.5}Tb_{0.5}Co_4O_9$) [542]. This result was achieved through an effective reduction of the charge carrier concentration combined with an increased phonon scattering arising from the big mass contrast generated by Tb.

2.7.2. Layered oxyselenides

Oxyselenides are a class of layer compounds containing both oxide and selenide anions (Fig. 1b). By modification of their cation composition, the electrical and thermal properties can vary significantly. The first representatives oxides adopting a layered ZrSiCuAs structure were reported more than 25 years ago [543]. Later, oxyselenides, and oxychalcogenides in general, were studied as potential superconductors [544], and semiconducting oxychalcogenides have been employed in optoelectronics [545]. The results achieved by Zhao et al. in 2010 [546] probably mark the beginning of the great interest in oxyselenides as thermoelectric materials. In more general terms, the zT of oxychalcogenides is restricted by the low σ ($\sim 10^3\ S\ m^{-1}$ at 850 K), arising from low charge carrier concentration ($10^{18}\ cm^{-3}$). However, α values as high as $-130\ \mu VK^{-1}$ at 100 K in LaFeAsO [547] are promising for low temperature thermoelectric cooling applications. A possible explanation for such behavior could be related to electron correlation or to 2D electron confinement in the FeAs layers. Pristine BiCuSeO shows a large α of about $350\ \mu VK^{-1}$ at room temperature, which rises to $425\ \mu VK^{-1}$ at 923 K [536]. Its *p*-type conduction is governed by cation vacancies. BiCuSeO overcomes the limitations of the most oxyselenides because of its outstandingly low κ of $0.6\ Wm^{-1}\ K^{-1}$ at room temperature, and drops to $0.3\ Wm^{-1}\ K^{-1}$ at 923 K. This leads eventually to a respectable zT value of 0.5 at 923 K. Structure modulation, obtained by combining two stable phases in one artificial superlattice (undoped BiCuSeO and heavily doped $Bi_{0.75}Ba_{0.25}CuSeO$), allows to increase σ at room temperature by one order of magnitude, while leaving κ unchanged. This leads to a record zT of 1.4 at 923 K [536].

2.7.3. Ruddlesden-Popper phases

Ruddlesden-Popper phases are layered perovskites containing two-dimensional slabs interleaved with cations (Fig. 1c). The general formula of Ruddlesden-Popper phases is $A_{n+1}B_nX_{3n+1}$, where A and B are cations, X is an anion (e.g., oxygen), and n is the number of the layers of octahedra. The first compounds belonging to this class (Sr3Ti2O7) were reported in 1958 [548]. The parent perovskite $SrTiO_3$ shows large thermopower values due to the large effective mass of the carriers resulting from its *d* band structure. $SrTiO_3$ is an electric insulator, but after cation substitution with La^{3+} or Nb^{5+}, it becomes semiconducting or even metallic [549]. Nevertheless, zT values of simple perovskites remained only moderate (0.27 at 1000 K for single crystals) because of their high κ. Structural changes have an impact on the electronic band structure and their electron transport properties. For example, a small distortion of the TiO_6 octahedra in the $SrO(SrTiO_3)_n$ breaks the spin-orbital degeneracy of the Ti t_{2g} orbitals at the bottom of the conduction band, leading to a decrease in the DOS and therefore to a reduction of the effective mass. These structural deformations are mainly

responsible for the observed changes of α. At higher temperatures, thermal vibrations reduce the distortion and lead to an increase of α. For $SrO(SrTiO_3)_2$ this translates only into a moderate zT of 0.27 at 1000 K [550], but surprisingly a 2D confinement of the electronic structure in a $SrTiO_3$ superlattice boosts their zT to a record value of 2.4 at room temperature [551].

Magnéli phases are related to the Ruddlesden- Popper phases *via* the ReO_3 parent structure block. Their first representatives were reported in the 1950s when a series of reduced titanium oxides were discovered by Magnéli [552]. Later, Magnéli phases of titanium, molybdenum and tungsten attracted much attention after charge density waves (CDW) were discovered in the low temperature regime [553]. Only recently they moved into the focus of thermoelectric research [554]. The structural key feature of the Magnéli phases is an intrinsic layered nanostructure defined by crystallographic shear (CS) planes which act as barrier for phonon transmission. The presence of these intrinsic defects allows approaching the problem of thermoelectric optimization from a totally different perspective that starts from a material with low κ. In the next step the power factor is increased by tailoring the charge carrier concentration by variation of the oxygen content (i.e. by filling the *d* band) of the material. This approach has been used already for WO_{3-x}, where an increase of the *d* electron count was achieved only by reduction, resulting in an increase of the overall figure of merit up to 0.24 at 1200 K [555]. Very recently, also a component of the Vanadium Magnéli phases (V_6O_{11}) was successfully synthesized and thermoelectrically characterized up to 600 K [556]. Measurements showed poor thermoelectric conversion properties, mainly due to very low values of σ. A similar architecture has been observed in several tetragonal tungsten bronzes (TTB), such as $Nb_{8-x}W_{9+x}O_{47}$ [557] or $Sr_xBa_{1-x}Nb_2O_{6-\delta}$ (SBN) [558]. These systems are structurally related to the Magnéli phases, and they are characterized by the possibility of changing the cation composition, and hence the electron density, without altering the crystal structure. In recent years promising results could be obtained for both the SBN and the fully substituted $Nb_{8-x}W_{9+x}O_{47}$, with a maximum zT above 0.2 at 1200 K [559,560].

2.7.4. Zinc oxides

The abundance (and costs) of Zn and O as well as its very high power factor at room temperature ($\approx$ 80 $\mu W m^{-1} K^{-2}$) make ZnO one of the most promising *n*-type oxide thermoelectrics. However, its large κ around room temperature ($\approx$ 40 $W m^{-1} K^{-1}$), associated with its high structural symmetry deriving from the wurtzite-like structure (Fig. 1d), makes it more suitable for high temperature applications, with κ dropping to $\approx$ 5 $W m^{-1} K^{-1}$ at 1000 K. This dramatic reduction of κ is explained by the large anisotropic thermal expansion with increasing temperature. In the last years, several approaches have been used in the attempt of reducing κ while maintaining the electronic properties, with the final goal of enhancing zT. One effective method is represented by the controlled introduction of a secondary phase that, upon precise thermal treatment, can be introduced as nano- precipitate. This is a complicated approach because the compatibility and the stability of the matrix and the selected secondary phase have to be thoroughly analyzed. Nevertheless, interesting results have been obtained using Al-nanocomposites, where the creation of plenty of defects and interfaces led to the reduction of κ to $\approx$ 2 $W m^{-1} K^{-1}$ at 1000 K. At the same time, the electronic properties remained basically unaltered and that translated in a final zT of 0.44 at 1000 K [561]. Similarly, a zT of 0.54 at 1173 K was achieved introducing polyparaphenylene (PPP) nanoparticles in the $Zn_{1-x}Ni_xO$ matrix, thanks to a combined increased power factor and a reduced κ [497]. In a more general sense, nanostructuring for both undoped and doped ZnO reduces κ, decreasing it to values of 3 $W m^{-1} K^{-1}$ at room temperature for nanograined ZnO [562]. Nevertheless, it is still characterized by low σ that limits the improvements in zT. By nanostructuring, combined with selective doping or co-doping, zT values up to 0.65 at 1247 K could be achieved [563].

In summary, oxides with adaptive structures (Fig. 26a) are promising candidates for thermoelectric applications because of (i) their low intrinsic thermal conductivity, (ii) metallic electrical conductivity and the possibility of (iii) tuning charge carrier concentration and (iv) thermal conductivity. Current state of the art oxides may reach thermoelectric zT values close or even above 1 (Fig. 26b), although not all intrinsic properties of oxides are conform to the guidelines for good thermoelectrics. Still, the low manufacturing costs and their high stability make them highly interesting candidates.

3. Organic semiconductors

Ever since Heeger and co-workers reported a high conductivity for iodine doped polyacetylene in 1977 [564], organic semiconductors have attracted a great deal of attention, as they combine (semi)conducting properties with the attributes of soft matter, which paves the way to the fabrication of flexible, light and bio-compatible electronic devices via cost-efficient processing from melt or solution. As the term *organic* denotes, this class of semiconductors is predominantly composed of carbon and hydrogen, along with nitrogen, sulfur and oxygen. These elements are abundant in nature and, even though the state-of-the-art research employs petroleum based molecules, organic semiconductors could potentially be synthesized from renewable resources [565,566]. The broad toolbox of polymer chemistry allows to synthesize a wide range of functional materials (see Fig. 27), which can then be processed into diverse architectures, from thin films, to bulk materials and foams, using either solution deposition, solid-state or melt processing techniques.

The electronic properties of (semi)conducting polymers are closely linked to their molecular structure. All organic semiconductors are based on a system of conjugated carbon-carbon bonds, which enables charge transport via delocalized electrons. In such conjugated systems, the *p* orbitals of neighboring atoms overlap, which results in the

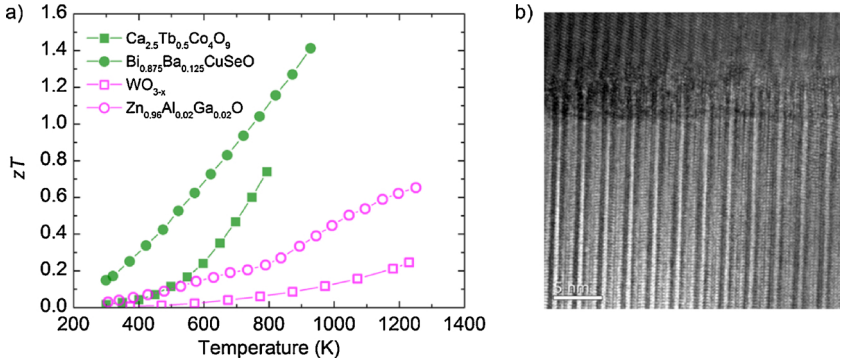

Fig. 26. Plot of zT vs. temperature of some of the most representative *p-type* ($Ca_3Co_{3.9}Fe_{0.1}O_{9+}\delta$; BiCuSeO) and *n-type* ($SrTiO_3$; WO_{3-x}; ZnO) oxide thermoelectrics. b) TEM image of CS (crystallographic shear) planes, a kind of intrinsic defect that characterize the Magnéli phases and in general the oxides with adaptive structures.

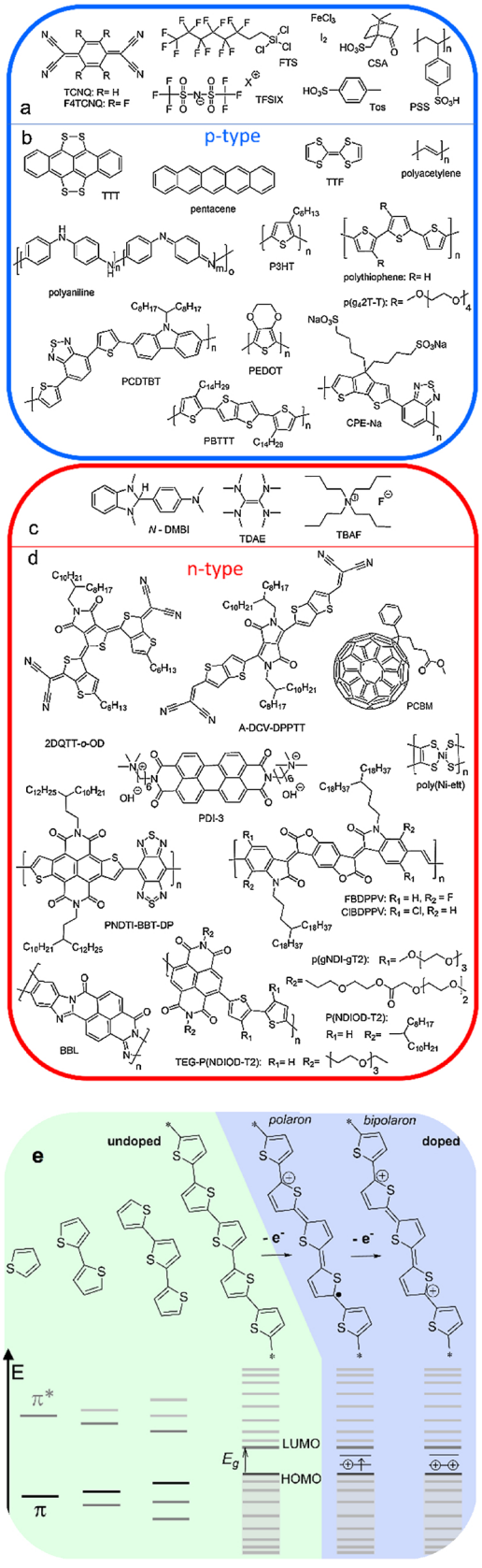

Fig. 27. Chemical structure of a) *p*-type dopants, b) *p*-type semiconducting small molecules/polymers, c) *n*-type dopants, and d) *n*-type semiconducting small molecules/polymers and e) scheme illustrating the emergence of HOMO and LUMO frontier orbitals upon increasing conjugation length and the formation of polarons and bipolarons upon *p*-type doping of polythiophene.

delocalization of the π electrons and the formation of a fully occupied bonding molecular orbital π and an empty antibonding molecular orbital π* (see Fig. 27). With increasing conjugation length, the π and π* orbitals form quasi continuous energy bands, which are delimited by the highest occupied molecular orbital (HOMO) and the lowest unoccupied molecular orbital (LUMO). The energy gap between the HOMO and the LUMO is called *band gap* E_g and is typically in the range of 1.5–3.0 eV.

In analogy to inorganic semiconductors, σ of organic semiconductors depends on the charge carrier density and can be tuned via doping (see Fig. 27). At low doping levels radical cations (in case of *p*-doping and radical anions in case of *n*- doping), so called polarons, are formed, which represent localized states in the band gap. Upon further doping, di-cations (di-anions), or so called bipolarons, are created and at high doping levels the bipolaronic states evolve into bipolaronic bands within the band gap [567]. In organic semiconductors doping can be achieved by either an electron or an ion transfer between a dopant molecule and the semiconductor [568]. A decisive driving force for the doping reaction is the energy levels of the frontier orbitals of the semiconductor and the dopant molecule. Moreover, it has been demonstrated that good miscibility, which ensures that the dopant and semiconductor are in molecular contact, is essential in order to obtain efficient and stable doping [569]. Thus, the choice of a suitable dopant-semiconductor couple is crucial.

Upon efficient doping, σ of an organic semiconductor can be enhanced by several orders of magnitude and for many materials, it is found that *PF* increases with the conductivity. Hence, current research predominately focuses on increasing σ by optimizing doping processes. Only for a few examples, such as the highly conducting PEDOT:Tos [570], it has been found that the highest power factor is obtained for intermediate doping levels. For the calculation of zT of a highly doped organic semiconductor ($\sigma > 100$ S cm^{-1}) it must be taken into account that, according to the Wiedemann-Franz law, an increase of σ concurs with an increase of κ [571–573].

Apart from the doping level, also the nano- and microstructure have a considerable influence on the thermoelectric properties. Recent studies suggest that, by increasing the degree of crystallinity of a material, which in some cases is accompanied by alignment of the semiconductor or *vice versa*, not only μ, and therefore σ can be greatly enhanced, but in many cases also α is improved [574–580]. This insight renders the control over the nano- and micro-structure an important tool to augment the *PF* of organic semiconductors. However, an increase in structural order also tends to enhance κ [572] and introduces anisotropy to the electrical and thermal conduction [581,582], which has to be considered for the measurement of the electronic properties and the calculation of zT.

One of the key assets of many organic (semi)conductors, and in particular of conducting polymers, is their excellent mechanical robustness and flexibility. Deposited onto flexible substrates, they have been shown to maintain their thermoelectric properties upon bending [583,584]. Thus, (semi)conducting polymers are promising candidates for flexible thermoelectric modules, e.g. for wearable devices [583].

Another important advantage of organic semiconductors for thermoelectric applications is their low κ. In case of polymers that display low $\sigma < 10$ S cm^{-1}, for instance, κ_{ph} amounts to 0.1 to 0.5 W m^{-1} K^{-1} and κ_{el} is negligible. Therefore, the main strategy for improving zT of organic thermoelectrics is to maximize the power factor $\sigma\alpha^2$ and in many studies κ and zT are estimated or not discussed. Moreover, the thermoelectric properties of organic semiconductors are commonly reported at room temperature, as the temperature range for operation is limited due to melting or degradation of the material above 500 K, as well as potential sublimation of the molecular dopant.

Already in the 1970s first studies on the thermoelectric properties of *p*-type organic small molecule semiconductors (see Fig. 27b) achieved high conductivities of 1200 S cm^{-1} and power factors of up to 147 μW m^{-1} K^{-2} for iodine doped TTT crystals [585]. Thin films of iodine doped

pentacene displayed similar Seebeck coefficients (α = 50 μV K^{-1}), but much lower conductivities of 60 S cm^{-1}, resulting in a *PF* of 13 μW m^{-1} K^{-2} [586]. The stability of both systems was found to be very limited due to rapid sublimation of the iodine dopant. Early studies on tetrathiafulvalene (TTF) derivatives reported a *PF* of 1.7 μW m^{-1} K^{-2} for $CuCl_2$ doped TTF powder [587] and only recently it was revealed that by using different solvents and the dopant TCNQ, TTF nanofiber networks with improved conductivity and a power factor 6 μWm^{-1} K^{-2} can be obtained [588].

The thermoelectric properties of *p*-type semiconducting polymers (see Fig. 27b) were first investigated in the 1980s and early studies were focused on linear polyacetylene [589]. Upon stretch alignment, highly ordered polyacetylene was obtained that could be doped with iodine - albeit limited by the poor environmental stability of the polymer - to attain an extremely high σ of 60000 S cm^{-1} and *PF*s up to 1350 μW m^{-1} K^{-2} (α = 15 μV K^{-1}). Much lower conductivities of approximately 100 S cm^{-1} were obtained for CSA doped polyaniline and PF_6- doped polythiophene, resulting in low power factors of 2 to 5 μW m^{-1} K^{-2} [590].

Important progress towards air stable, high performance organic *p*-type polymers was made in the 2010s. Mai et al. presented highly air stable films of self-doped conjugated polyelectrolytes, which displayed a high α of 195 μV^{-1} and a low thermal conductivity in the range of 0.2 W m^{-1} K^{-1}. However, their *PF* was limited to 0.84 μWm^{-1} K^{-2}, due to a low conductivity of 0.22 S cm^{-1} [591]. Higher, air stable *PF* of up to 19 μW m^{-1} K^{-2} were first published by Leclerc and co- workers in 2009 for $FeCl_3$ doped polycarbazoles such as PCDTBT [592].

The most promising properties for air stable organic *p*-type thermoelectrics to date were reported for polythiophene derivatives. The extensively studied P3HT, for instance, displays a *PF* of 20 μW m^{-1} K^{-2} upon sequential doping with the acid TFSI [593]. By increasing the degree of crystallinity in P3HT via small molecule epitaxy, the thermoelectric performance of TFSI doped P3HT films could be decisively increased (σ = 320 S cm^{-1}, α = 269 μV K^{-1} and *PF* = 62 μW m^{-1} K^{-2}) [21]. Furthermore, it was shown by Kroon et al. that the processability as well as the doping efficiency and stability can be enhanced by introducing polar oligo ethylene glycol side chains to the polythiophene backbone [594].

The importance of the processing method and microstructure for the thermoelectric properties was also clearly demonstrated for other polythiophene derivatives such as PBTTT and PEDOT. PBTTT films, for instance, displayed 100 times higher conductivities upon vapor doping with F4TCNQ as compared to solution doped samples and a power factor of up to 120 μW m^{-1} K^{-2} was obtained due to an increase in the doping level [578,595]. PEDOT, which has been studied in combination with various dopants and processing routes, is the current champion material among *p*-type organic polymers. When electropolymerized with TFSI counter ions it displays a σ of 1100 S cm^{-1} together with α = 40 μV K^{-1}, which amounts to a *PF* of 147 μW m^{-1} K^{-2} [596]. By optimizing the doping level of in-situ polymerized PEDOT:Tos films, Bubnova et al. obtained power factors of 324 μW m^{-1} K^{-2} and zT = 0.25 [570], which could be further improved to 454 μW m^{-1} K^{-2} (σ = 1500 S cm^{-1}, α = 55μV K^{-1}) [575] for highly crystalline PEDOT:Tos, obtained by vapor polymerization of EDOT onto a co-polymer template. For the sake of easy processing PEDOT is often used in the form of the PEDOT:dopant complex PEDOT:PSS, which is commercially available as an aqueous dispersion. The thermoelectric properties of pristine PEDOT:PSS films cast from commercial inks are typically on the order of σ = 0.1 S cm^{-1} and α = 30 μV K^{-1}. However, it has been shown that its thermoelectric properties can be greatly enhanced by optimization of the doping level [597] or upon treatment with high boiling point solvents or acids, which can be attributed to a change in the film nanostructure and results in power factors of up to 80 μWm^{-1} K^{-2} (σ = 1900 S cm^{-1}) and a zT of 0.32 [598]. The κ of PEDOT:PSS is commonly low (0.2 - 0.3 W m^{-1} K^{-1}). This can be explained by the nanostructure of PEDOT:PSS films, which consist of sub micrometer-sized grains, that lead to phonon scattering at the grain boundaries. In highly conducting PEDOT:PSS, however, κ was found to be highly anisotropic. In the direction of high electrical conductivity κ was reported to reach 1.0 W m^{-1} K^{-1} due to an increase of κ_{el} [573]. PEDOT:PSS is a very promising organic *p*-type material, which allows the design of flexible, light and printable thermoelectric generators and thermoelectric textiles.

The development of organic *n*-type materials, however, turns out to be more challenging, due a high sensitivity to air and moisture of *n*-doped organic semiconductors. One possible approach is the development of *n*-type materials based on organic small molecule semiconductors (see Fig. 27d) and carbonaceous nanostructures (see also Chapter IV). Vapor doped fullerenes and their derivatives [599–602], which have been studied since the 1990s, show power factors of up 28 μWm^{-1} K^{-2}, depending on the doping conditions [601] and the obtained nanostructure [600]. Only recently comparable electronic properties were obtained for the solution processable PCBM (α = -840 μVK^{-1}, σ = 40 S cm^{-1}, *PF* =35 μW m^{-1} K^{-2}) [603] and it was demonstrated that the miscibility, stability and thermoelectric performance of N- DMBI doped fullerenes can be significantly improved by modification of the butyric acid ester group with more polar oligo ethylene glycol [604].

Another type of small molecule *n*-type semiconductor, which has been widely studied are derivatives of naphthalene and perylene diimides [605–608]. Upon functionalization with trimethylammonium bearing groups perylene diimides (PDIs) were found to form self-doped, electrochemically stable and water-soluble *n*-type thermoelectric materials. Upon optimization of the length of the pendant group, a *PF* of up to 1.4 μWm^{-1} K^{-2} was reached. More recently Russ et al. [607] suggested that the ability of self-doing via functionalization with trimethylamine bearing side groups can be transferred to other small molecule systems such as fullerenes. This approach is of interest as it allows the design of *n*-type materials that consist of only one component, which facilitates processing and prevents issues related to inhomogeneous doping and phase separation. The latest studies on thiophene based small molecules, such as 2DQTT-o-OD [609] and DPPTT [610], demonstrated that these molecules can be efficiently doped with DMBI derivatives via co- processing from solution. Under N_2 atmosphere N-DMBI doped DPPTT displayed σ = 3.1 S cm^{-1}, α = −568 μV K^{-1} and κ = 0.25 W m^{-1} K^{-1}, resulting in a record high power factor of 105 μW m^{-1} K^{-2} and zT = 0.11 at room temperature [610].

One of the most studied *n*-type polymers (see Fig. 27d) is the solution processable naphtalenedicarboximide bithiophene copolymer P(NDIOD)T2. Upon *n*-doping with DMBI derivatives [611,612], TDAE or Na-silica gel particles [613], a σ in the range of 10^{-4} to 10^{-2} S cm^{-1} with an α of -500 to -850 μV K^{-1} were obtained. More polar naphtalenedicarboximide bithiophene derivatives, such as p(gNDI-gT2) [614] and TEG-P(NDIOD)T2 [615], displayed an improved miscibility with the dopant N-DMBI, leading to a higher doping efficiency and conductivity (σ = 0.1-0.2 S cm^{-1}, *PF* = 0.4 μW m^{-1} K^{-2}), which was stable for up to 20 min in air in the case of p(gNDI-gT2) [614]. Very recently Takimiya and co- workers presented a structurally similar co-polymer, PNDTI-BBT-DP, that showed higher crystallinity and a significantly improved conductivity and power factor (σ = 5 S cm^{-1}, *PF* = 14 μW m^{-1} K^{-2}) upon doping with N-DMBI [616].

Bao and co-workers proposed that the conductivity of distorted donor-acceptor polymers is intrinsically limited due to a strong localization of the polarons on the polymer backbone [617]. Consequently, torsion free, linear ladder type polymers, which allow a strong polaron delocalization, are promising candidates for high performing *n*-type thermoelectrics. *n*- doping of the ladder polymer BBL with TDAE resulted in a *PF* of only 0.43 μW m^{-1} K^{-2} (Seebeck coefficient of -60 μV K^{-1}) [618].

Considerably higher *PF*s of up to 28 μW m^{-1} K^{-2} under N_2 [619] and of 0.63 μW m^{-1} K^{-2} in air [620] were obtained for the halogenated

derivatives of benzodifurandione poly(p-phenylene vinylene) FBDPPV and ClBDPPV upon doping with nDMBI and TBAF, respectively. A very different family of *n*-type materials, which were reported by Sun et al., are insoluble organometallic compounds such as poly(Ni 1,1,2,2-ethenetetrathiolate) (poly[K_x(Ni-ett)]) [621,622]. Thin films of poly[K_x(Ni-ett)] prepared via electrochemical deposition on flexible, insulating polymer substrates were recently reported to display a σ of up to 220 S cm^{-1} together with an α of -134 μV K^{-1} (PF = 453 μW m^{-1} K^{-2}) and κ of 0.5 W m^{-1} K^{-1}, resulting in an outstanding zT of 0.2 W m^{-1} K^{-1} [622].

An extensive graphical summary of the thermoelectric performance of organic *p*- and *n*- type materials is shown in Fig. 28. It becomes clear that σ and α depend on each other. Chabinyc and co-workers [581] suggested the empirical relation $\alpha \propto \sigma^{-1/4}$ ($\sigma\alpha^2 \propto \sigma^{1/2}$) for *p*-type materials, which was recently confirmed by Kemerink and co-workers for organic *n*-type thermoelectrics [603]. However, in some cases it seems that another exponent would result in a better fit of the experimental data. Lines representing a constant figure of merit zT, by taking into account the increase of κ with increasing σ according to the Wiedemann-Franz law, suggest, that a $zT > 1$ is more likely for *n*- type than *p*-type materials, provided that σ can be increased further. However, a possible strategy to bypass these limitations is the decoupling of the electronic and the thermal conductivity, for instance, by creating heterogeneous materials such as nanocomposites with carbon nanotubes, graphene (see Chapter IV) or inorganic nanowires [623,624] with interfaces that enhance phonon scattering.

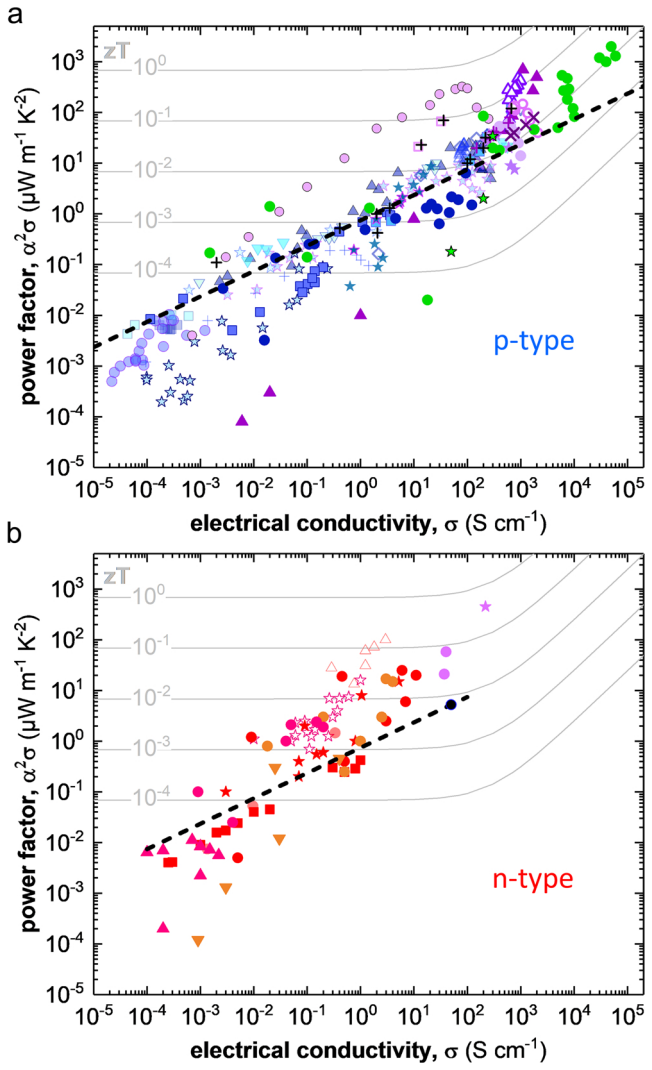

Fig. 28. Thermoelectric PF as a function of σ for various organic a) *p*-type (blue: polythiophene derivatives [15], purple: PEDOT [5,10,29–31], green: polyacetylene [22,23]) and b) *n*-type materials [43–46,51,53,54,56,57] extracted from literature. The dashed lines represent the relation $\alpha \propto \sigma^{-1/4}$, as suggested by Chabinyc and coworkers [581] and by Kemerink and co-workers [603]. The gray lines represent lines of a constant figure of merit zT. The zT was estimated assuming i) a phonon contribution to the thermal conductivity of k_{ph} = 0.2 W m^{-1} K^{-1}, and ii) that the Wiedemann-Franz law is obeyed so that $PF = (k_{ph} / T + \sigma L)$ zT, with L being the Lorentz number (for interpretation of the references to colour in this figure legend, the reader is referred to the web version of this article).

4. Composites

Most of the work devoted to enhancing the thermoelectric properties of organic materials focuses on increasing the electrical conductivity while, in the case of inorganic materials, strong efforts are directed towards reducing the thermal conductivity of optimally doped systems. One key difficulty is the fact that for most systems, α, σ, and κ, are strongly correlated. The production of nanocomposites is a strategy aimed, precisely, at partially decoupling the thermoelectric variables. The synergistic effects that can be obtained by bringing together two or more components in terms of structure and electronic properties, combined with the role of the large amount of interfaces, have produced a stream of promising results [623,625–627]. The nanoscopic dimensions of at least one of the components may offer additional thermoelectric advantages, as discussed in the panel “On the theory of thermoelectric transport in the solid state”. Interestingly, these observations contradict early theoretical predictions, which stated that zT of a composite cannot exceed the zT of the constituents [628], probably due to the fact that synergistic and interfacial effects were not properly accounted for in these predictions.

In most cases, the constituents of a nanocomposite are chosen to exhibit complementary strengths. For example, low-dimensional structures with favorable electronic properties, such as two-dimensional sheets, or one-dimensional tubes or wires embedded in a disordered matrix with low κ, as sketched in Fig. 29. The inclusions can be nanostructured inorganic thermoelectric materials, such as for example Te- nanowires, metal nanowires, or carbon-based fillers, such as graphene and carbon nanotubes (CNTs). In these composites, the matrix material serves to bind the filler together, while also conferring additional benefits, such as a lowered κ [629,630], a tunable doping level [631], solution processability [623], reduction of overall cost or flexibility compared to bulk films of neat filler [632]. Due to their versatility, polymers are often the matrix of choice. The fillers on the other hand may provide an increased α, as is the case for semiconducting inorganic fillers [623], or increased σ and mechanical stability for CNTs [633]. This is advantageous, because dopant concentrations in highly doped organic thermoelectric materials can reach tens of mol%, and films typically lose some of their inherent flexibility, even becoming brittle.

Polymer-based TE composites are typically processed from solution and deposited by coating methods or by vacuum filtration, which results in thin films of several micrometers or less. Due to the intrinsic high aspect ratio of polymers and nanofillers, some degree of preferential orientation of the long conductive fillers is expected alongside polymer alignment in these solution processed films. While this complexity may offer potential venues to further decouple thermoelectric variables in the future, it currently introduces a significant measurement hurdle, because most standard measurement techniques provide in-plane σ and α values, yet out-of-plane κ. Recently, there have been more reports in which σ and κ were measured in the same direction [627,630,634–636], yet few use the same sample for all measurements [636]. Indeed, thermal conductivity is often not reported, especially in the early literature. Therefore, this section will mainly focus on the PF when comparing results.

The following subsections will briefly summarize the different types of composites, including polymer-inorganic and carbon-based

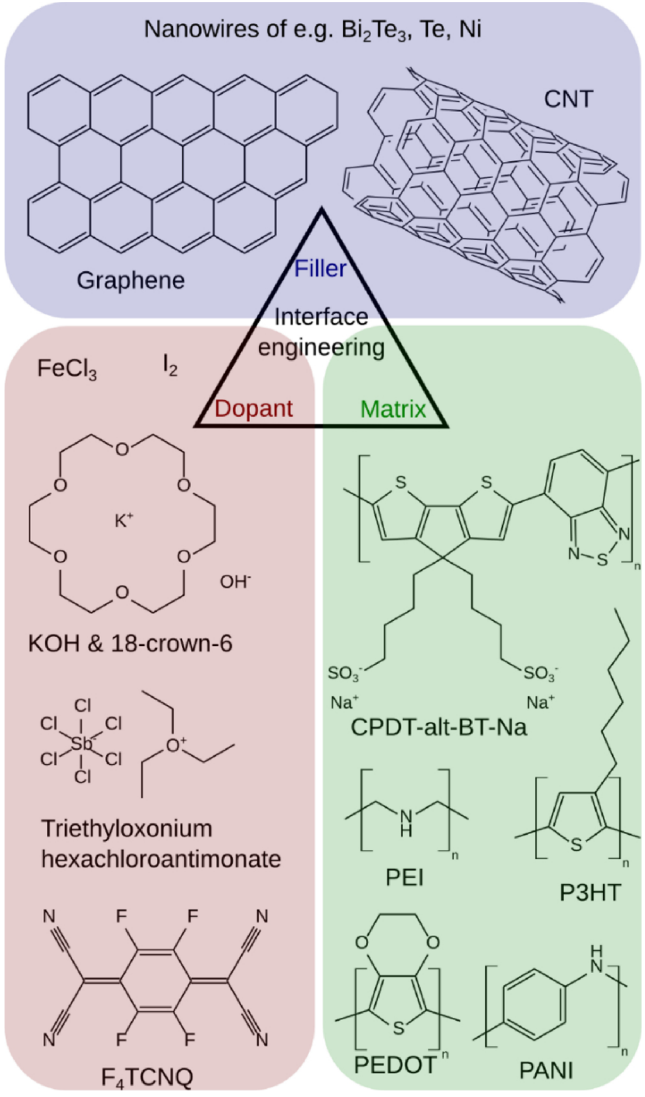

Fig. 29. Components of a composite. The low-dimensional filler material is introduced into a polymer matrix. Carrier concentration is optimized with an additional dopant. Increased performance of composites is attributed to the internal interfaces.

composites, highlighting some of their possible advantages over single-component materials. Since the available literature on CNT composites is more extensive than on other thermoelectric composites, that specific subsection analyzes them more extensively, detailing several qualitatively different approaches towards nanocomposites.

4.1. Polymer-inorganic composites

The main rationale for research into polymer-inorganic composites for thermoelectrics is to improve the performance of an already well-known inorganic material even further by lowering its thermal conductivity without significantly affecting other properties. Polymer matrices may also provide some degree of flexibility and lower volumetric cost. On the other hand, using a polymer as matrix limits the maximum operational temperature to values typically lower than 500 K.

In an early unsuccessful attempt, the voids in an array of vertical silicon nanowires, which were grown by the vapor-liquid-solid method, were filled with an insulating polymer, in the hope of lowering only κ, while benefiting from an increase in α due to the reduced dimensionality of the nanowires [637]. However, σ strongly decreased as well. By using electrically conductive PEDOT:PSS, this decrease in σ could be largely averted, as reported for composites of ball-milled Bi_2Te_3 mixed with PEDOT:PSS, which reached power factors of 131 and 80 $\mu W m^{-1} K^{-2}$ for *p*-type and *n*-type composites respectively [638]. While this was an improvement over neat PEDOT:PSS, it remained below the performance of bulk Bi_2Te_3, which was attributed to the contact resistance between the components.

Synthesizing Te nanowires from Na_2TeO_3 with ascorbic acid as a reducing agent and PEDOT:PSS as structure directing agent, results in a water-soluble composite of polymer-covered crystalline nanowires. The power factor of the composite reached 71 $\mu W m^{-1} K^{-2}$ and $zT \approx 0.1$, which are higher than those of either component [623]. Additional investigation of parameters such as nanowire length and loading, allowed to increase the power factor further, above 100 $\mu W m^{-1} K^{-2}$ [639]. Electrical conduction in these composites was argued to proceed mainly along a layer of highly conductive polymer which covers the nanowires [640], demonstrating the important influence of interfacial effects on thermoelectric properties.

One recurring explanation for the increased thermoelectric performance of polymer-inorganic composites is energy-filtering at the numerous internal interfaces. By blocking low energy charge-carriers, which decreases σ, the average energy carried per charge can be increased, strongly increasing α. However, this effect is hard to measure in isolation, without also changing other parameters such as morphology or composition, which is why few conclusive reports exist. One work on composites of P3HT and Bi_2Te_3 nanowires cited a doping dependent scattering of carriers as the reason for an improved power factor of 13.6 $\mu W m^{-1} K^{-2}$ [641]. Similarly, α of composites of PEDOT:PSS and Te-nanowires containing a $Cu_{1.75}Te$ sub-phase was observed to be higher than that of the pure components. This increase in α at low Cu loading was accompanied by a slight decrease in σ, which was rationalized by the appearance of an additional energy-dependent carrier scattering mechanism [642]. Even more complex materials, such as composites of Te- nanowires, PEDOT:PSS and reduced graphene oxide were investigated. In these ternary composites energy filtering is thought to occur at both of the distinct barriers, with a reported power factor of 143 $\mu W m^{-1} K^{-2}$ [643].

While the mentioned reports hint at the existence of an energy-filtering effect, another study argues that such an effect is not necessarily present. In the latter experiments, the energy barrier between P3HT and Te-nanoparticles was tuned by nearly 1 eV by controlling the concentration of $FeCl_3$ dopant. Even though this change in the barrier was expected to produce some effect, nothing of the sort was observed. Instead, α of the composite never rose above that of the pure components and it was concluded that energy filtering is not required to explain the observed results. A simple linear combination of parallel and series transport was sufficient [644].

Another, comparably straightforward, approach to increase the thermoelectric performance uses metal nanostructures embedded in a polymer matrix to achieve high σ. For example, by introducing silver nanowires into a PEDOT:PSS matrix, σ was reported to increase fivefold with respect to the bare matrix, without affecting α or κ [645].

Even examples that do not require any semiconducting material at all exist, such as a report on nanowires made of nickel, a metal with a moderately negative α, which were embedded in an insulating matrix of poly(vinylidene fluoride). The reported power factor of 220 $\mu W m^{-1} K^{-2}$ for a composite that contains 80 wt% nickel is significantly less than that of pure nickel. Yet, combined with the extraordinarily low thermal conductivity of $\kappa = 0.55 W m^{-1} K^{\&\ \#8722;1}$, this corresponds to a zT of 0.15 [629]. The corresponding temperature dependent performance as well as microstructure of this system is shown in Fig. 30.

4.2. Organic composites

The favorable interactions due to π-π-stacking and the resulting conformational changes among organic composites allowed to reach

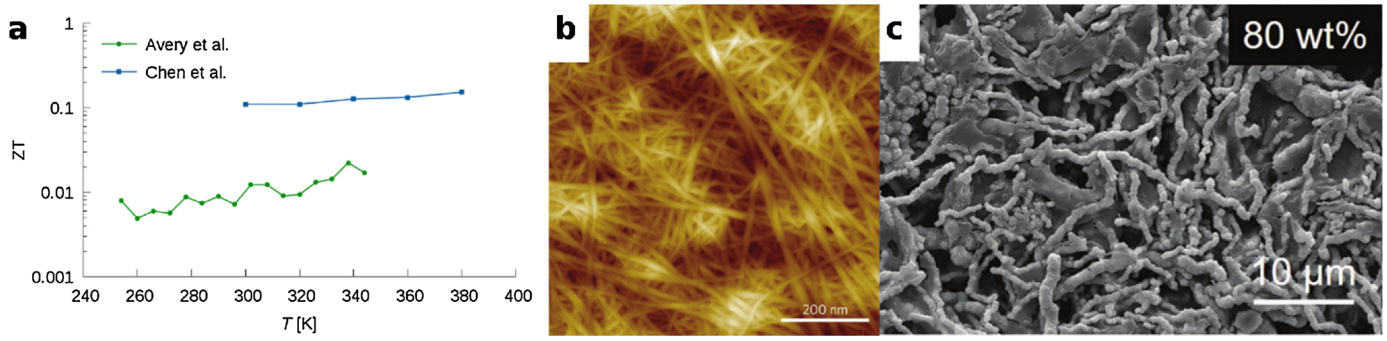

Fig. 30. Two representative composites. zT (a), and morphology for semiconducting CNTs with residual sorting polymer (b), and Ni nanowires in PVDF (c). Adapted with permission from Refs. [627] and [629]. Copyright 2016 Nature Publishing Group and 2017 Wiley-VCH respectively.

particularly large gains in *PF* compared to single-component materials. Moreover, purely organic nanocomposites are based on raw materials that are abundant, compared to most other inorganic thermoelectric materials, with the notable exceptions of silicon, silicides and some oxides. While the synthesis of the organic constituents may require significant amounts of energy, further processing does not, since it is done from solution, close to room temperature. Due to their nature, they are not stable at elevated temperatures, but the hope is that they can be mass-produced cheaply, allowing to occupy the hitherto unprofitable niche of near room-temperature thermoelectric applications.

4.2.1. Polymer-polymer composites

By blending two semiconducting polymers with slightly different HOMO levels, like P3HT and P3HTT, the density of states can be engineered, for example, by adding a peak close to the Fermi level. This introduces an energy barrier which decreases σ, yet acts as a larger effective derivative of the density of states with respect to energy, leading to an increase in α [646].

More recently, a similar study improved upon this method by using blends of P3HT and PTB7 or TQ1, reaching record values of α of more than $1\,mV\,K^{-1}$ even after doping, and confirming the proposed mechanism by simulations [647]. The same mechanism was demonstrated in *n*-type blends of PCBM, when mixed with another small molecule with a slightly offset LUMO level [603].

Another possible way to increase the thermoelectric performance is interfacial carrier scattering, a process known to increase performance in inorganic thermoelectric materials. In organic materials, such as composites of PEDOT:PSS with PEDOT nanowires, this process was observed to result in a significant improvement of α, though only if the mobility of the host material was above a threshold value of about $1\,cm^2\,V^{-1}\,s^{-1}$ [648].

Yet one does not have to go to such great lengths to find possible advantages of polymer-polymer composites. Doped P3HT maintained its thermoelectric performance even when up to 60 wt% of it was replaced by insulating poly(ethylene oxide). Besides saving on expensive material, this allowed to prepare more mechanically robust, and thicker freestanding films [632].

4.2.2. Polymer-graphene composites

Among the low-dimensional carbon allotropes, graphene may not be an obvious first choice as a thermoelectric material, due to its symmetric density of states without band gap, and its high κ. Still, some promising reports of composites with conducting polymers exist.

By varying the mixing ratio of PANI and graphene nanosheets, a concurrent increase of σ and α was observed, resulting in a *PF* of 5.6 $\mu Wm^{-1}K^{-2}$ in pellets with a 1:1 ratio, [649] which was rationalized by a higher μ of the composite. It was observed, however, that the thermoelectric performance of graphene composites strongly depends on the quality of the graphene, in particular the amount of oxygen impurities [650].

Composites of graphene with C_{60} and PEDOT:PSS reached *PF* of 32 $\mu Wm^{-1}K^{-2}$ and a figure of merit of $zT = 0.067$ thanks in part to the low κ of fullerenes [651].

For an exhaustive summary of the literature on the thermoelectricity of graphene or carbon nanotubes and their composites, the reader is referred to recent reviews [652,653].

4.2.3. Polymer-carbon nanotube composites

While there is some discussion over when they were first observed [654], interest into carbon nanotubes rose strongly after a report in 1991 [655]. Their excellent electrical and thermal properties promised many possible applications. Among them was the idea to increase κ of polymers by adding small quantities of CNTs. Results were uncertain, however, and κ of most types of composites remained comparably low [656,657]. This, in turn, proved to be an encouraging result for the potential use of CNTs in thermoelectric composites.

Several different approaches to organic thermoelectric CNT composites exist. The basic principles include electronic percolation, secondary doping (through charge carrier mobility modifications), energy filtering, interface engineering, improved CNT dispersion and chirality selection, and multiple strategies for varying charge carrier concentration, i.e. doping.

Early on, experiments with simple composites of CNTs and gum arabic showed that σ can be at least partially decoupled from κ, allowing for favorable thermoelectric properties [658]. The underlying mechanism for this is the fact that electrons are transported through percolative paths, while heat flows in parallel between the insulating matrix and minute amounts of the conductive filler. The interfaces between both materials also have a strong influence, as we will see below. The gum arabic not only decreased κ of the final film, but also stabilized the CNTs in solution, providing solution-processability.

Building on low-κ CNT composites, the gum arabic has been substituted with conducting and semiconducting polymers. Both strategies have led to improvements in the thermoelectric transport properties of the composites, yet due to different reasons. On the one hand, by replacing the electrically insulating gum arabic by conductive PEDOT:PSS and polyaniline (PANI), a similar approach produced promising early results, with measured *PF* up to 160 $\mu Wm^{-1}K^{-2}$ [625,659] and 220 $\mu Wm^{-1}K^{-2}$, respectively [660,661]. As opposed to insulating or semiconducting matrices, in conducting polymer composites, charge transport through networks of percolating CNTs may not necessarily dominate. Instead, for instance, σ of PEDOT:PSS can be raised to that of CNTs by utilizing well documented procedures, such as the removal of excess PSS by cosolvent treatments. In this case, the addition of nearly percolating amounts of CNTs raised both α and σ, with a reported *PF* of 464 $\mu Wm^{-1}K^{-2}$. This was rationalized by energy- filtering, that is, the selective scattering of low energy carriers at interfaces between polymer- covered CNTs [662].

More generally, in composites of CNTs with conducting polymers like PEDOT:PSS [625,659,662] or PANI [626,660,661,663],

morphological or secondary doping plays an important role. The polymer chains are thought to partially align along the CNT axis [660], resulting in a more stretched and planar chain with increased conjugation length and higher μ compared to the otherwise folded or twisted conformations [626,663]. This secondary doping is typically observed as a concurrent increase of both α and σ. Unlike during regular doping, this decoupling of α and σ is made possible by increasing μ instead of the charge carrier density.

On the other hand, by replacing the insulating gum arabic with semiconducting polymers, like P3HT, the high mobility CNTs dominate σ, which is evidenced by the percolative behavior observed with increasing CNT content [631,633]. P3HT, while not significantly contributing to charge transport by itself, influences both σ and α by doping the CNTs [631].

P3HT-based composites have reached promising *PF* [633,664,665]. Early work reported composites doped with iron chloride by immersion in a nitromethane solution, which resulted in *PF* of 95 $\mu Wm^{-1}K^{-2}$ [633]. By spin-coating the dopant onto thin composite films, this could be increased to 267 $\mu Wm^{-1}K^{-2}$ [664]. Spray-coated composites of P3HT and CNTs have shown *PF* of 325 $\mu Wm^{-1}K^{-2}$ [665].

In addition to doping the CNTs in the final film, many polymers also act as a surfactant, which allows for an improved dispersion of CNTs during solution processing. While there are many non-conjugated surfactants available that could be used, their presence is normally not desired in the final film since their insulating nature negatively influences σ, and thus they should be removed after deposition. On the other hand, conjugated polymers do not necessarily have to be removed, since CNTs are well-dispersed in the (semi-)conducting matrix, mostly maintaining their high σ, while κ is considerably lowered.

Moreover, polymers may even exhibit selectivity towards a specific chiral angle and/or nanotube radius, allowing to prepare films of CNTs of a single chiral vector. This is of great importance, because it was shown that semiconducting or chirally pure CNTs can exhibit α that is nearly two orders of magnitude higher than that of metallic CNTs, if their doping level is precisely controlled [627,666–669].

By separating them from the metallic species, semiconducting CNTs that contain residual sorting polymer have shown *PF* of 340 $\mu Wm^{-1}K^{-2}$ [627]. The temperature dependent performance as well as microstructure of this system is shown in Fig. 30 . Using cleavable polymers allowed to remove this residual polymer from the final film, after it served its function of selecting CNTs of a specific chiral vector, further increasing the *PF* to 398 $\mu Wm^{-1}K^{-2}$ for *p*-doped films [670], and even further to > 700 $\mu Wm^{-1}K^{-2}$ for both *p*- and *n*- doped films, corresponding to $zT \approx 0.12$ [634].

In this set of studies, the highest *PF* was obtained not for a composite, but for neat CNTs [627,634,670]. However, it was observed that to achieve best results, the nanotubes should be as dispersed as possible. In order to achieve this, the surfactant properties of the polymer are required during deposition to minimize aggregation and bundling. It should only be removed after film formation is complete and the final morphology is locked in [670]. Because these films contain little to no residual polymer, one would expect κ to be significantly higher compared to composites. Yet it was shown that the introduction of a small-molecule dopant has a similar, yet less pronounced effect, lowering κ to values intermediate those of neat CNTs and their composites [627].

Decreasing bundle size is not the only way to higher performance. Similar *PF* have been reached by disregarding effects of dispersion and bundle size, and instead focusing on the ionic interactions of CNTs doped with in situ polymerized polyelectrolytes. This approach allowed to increase the power factor of neat buckypaper by more than four times, reaching values greater than 460 $\mu Wm^{-1}K^{-2}$ [671].

So far, the performance of *n*-type composites has lagged behind that of their *p*-type counterparts, mainly because they are inherently less stable towards oxidation.

A large selection of *n*-type dopants has been investigated [635,671], including small molecules [672,673], dye nanoparticles [674], salts [635], and electron-rich nonconjugated polymers like polyethylenimine (PEI) [675–683]. While the stability of *n*-type composites somewhat varies among reports, some general trends have become apparent. Larger counterions yield a more effective and stable doping of the delocalized π-electron system of CNTs [635,671]. This increased stability may at least in part be due to an increased coverage of the CNT surface, physically blocking oxygen from accessing and dedoping the CNTs. It was further shown that the effect of *n*-type dopants can be maximized by first removing already adsorbed oxygen from the surface of the CNTs by thermal annealing [673]. This allowed to reach a staggering *n*- type *PF* of 3103 $\mu Wm^{-1}K^{-2}$, corresponding to $zT = 0.19$, starting from already impressive as- spun CNT webs with a *PF* of approximately 1400 $\mu Wm^{-1}K^{-2}$. An organic thermoelectric generator that used these materials was able to harvest 123 μW from body heat alone [673].

By using CNTs together with combinations of multiple *n*-type dopants like PEI and $NaBH_4$, an *n*-type *PF* of 38 $\mu Wm^{-1}K^{-2}$ was achieved [678]. Adding diethylenetriamine as a third dopant, further improved performance and allowed to demonstrate a simple glucose sensor powered by a TEG composed of 72 thermocouple pairs [681]. A combination of a higher *n*-type *PF* of 172 $\mu Wm^{-1}K^{-2}$ and stability of σ in air for at least one month was demonstrated by doping CNTs with nanoparticles of malachite green [674]. A much larger *n*-type *PF* was instead claimed for a hybrid material based on EDOT monomers polymerized in the presence of CNTs and doped with tetrakis(dimethylamino)ethylene: in this case an extraordinarily large, albeit controversial, negative α of $\sim -1\,mV\,K^{-1}$ was reported, resulting in a claimed *PF* of 1050 $\mu Wm^{-1}K^{-2}$ [684].

Another promising approach for the preparation of both *p*- and *n*-type materials are composites of CNTs and water-soluble conjugated polyelectrolytes [630,685]. These conjugated polymers have ionic groups covalently attached to their side chains. Depending on the specific counterion, these polyelectrolytes may self-dope either *p*- or *n*-type. The polyelectrolytes serve as surfactant as well as dopant, and the resulting CNT composites are processable from aqueous solution. It was shown that the anisotropy of κ in these composites is about one order of magnitude [630], highlighting that σ and κ have to be measured in the same direction when determining zT of organic composites.

Interface engineering in multilayer structures has proven particularly promising. The layer-by-layer assembly of CNTs and graphene which are stabilized in solution by PEDOT:PSS, and polyaniline, has demonstrated exceptional *PF* of 1825 $\mu Wm^{-1}K^{-2}$ [663], and 2710 $\mu Wm^{-1}K^{-2}$ [626]. Remarkably, these structures exhibit *PF* that increase with an increasing number of deposition cycles, again demonstrating the pronounced role of interfaces. The high *PF* is rationalized by the increased μ and the highly interconnected components of these multilayers. Using different polymers, the same layer-by-layer assembly allowed to achieve *n*-type *PF* of 190 $\mu Wm^{-1}K^{-2}$ [675].

5. Summary and Perspectives

The debate between Galvani and Volta, at the end of the XVIII century, on the nature of electrical phenomena in animals, ultimately led to Volta's conclusion that the electromotive force producing dead frogs muscles response originated from the temperature difference between the junctions of two dissimilar conducting materials in contact with them: it was at this point in time that he unveiled the thermoelectric effect, although Volta's name is not directly linked today to any thermoelectric phenomenon. The generation of electromotive force across a temperature gradient is instead linked to Seebeck, who independently observed, at the beginning of the XIX century, the deflection of a compass magnet under the influence of an electric circuit made by two dissimilar metals having the two junctions at different temperatures, erroneously claiming the observation of thermomagnetism. Yet his observations were crucial, as the scientific community in the first half of the XIX century correctly interpreted them, strongly contributing to the development of thermoelectricity, name

proposed by Ørsted shortly thereafter. Almost at the same time Peltier made his observations on the release and absorption of heat by junctions made of dissimilar conductors when a current is forced across them, which we now know as the Peltier effect, the explanation of which saw the decisive contribution of Lenz. The third thermoelectric effect, describing the release or absorption of heat in a homogeneous material subjected to a temperature gradient when a current flows through it, is known as the Thomson effect, who correctly predicted it in the middle of the XIX century. Thomson also proposed the first complete thermodynamic explanation of the thermoelectric effects and showed they are all related, spurring a fast advancement in the field of thermal to electrical energy conversion through generators. Regarding the efficiency of the latter, it was Altenkirch at the beginning of the XX century who authored its first satisfactory derivation, indicating the general guidelines for optimal thermocouples, *i.e.* thermocouples had to be made with large relative Seebeck coefficients, low electrical resistance and low thermal conductance. Further insight into thermoelectricity came with the advent of non-equilibrium thermodynamics, and the application of Onsager's methodology for non-equilibrium transport phenomena that allowed to generalize the Thomson coefficients for anisotropic non-time-reversal-symmetric media. The following great boost to the field came along with the modern theory of semiconductor physics, thanks to Ioffe, who around the mid of the XX century identified heavily doped semiconductors as the best thermoelectric materials. He also introduced both the dimensionless material (zT) and thermocouple (ZT) figures of merit, as used today to compare different materials and to express the efficiency of generators and coolers, respectively. Later advancements in the field of semiconductors and in their understanding led to the fundamental Slack's phonon-glass electron-crystal concept, still leading thermoelectrics development. Towards the end of the XX century new hopes for thermoelectric energy conversion came by the prediction of zT improvement upon nanostructuration by Hicks and Dresselhaus, allowing to reconsider a widespread application of thermoelectric technology.

In parallel, the history of thermoelectric devices show periods of excitement following new discoveries, and more static periods waiting for the next breakthrough to come. Ørsted, with the help of Fourier, was the first to produce, at the beginning of the XIX century, a thermoelectric pile based on Bi and Sb, shortly after improved by Nobili and Melloni. At this time the device was used as a sensor of temperature and infra- red radiation. It was thanks to the work of Rayleigh in the second half of the XIX century that thermoelectric power generation started to be considered, exploiting hot gases or liquid sources. Notable was the Clammond's pile, made of 3000 thermocouples and converting heat from a coke fireplace. The next evolution was only possible thanks to semiconductor technology of the XX century: after the World War II, Telkes fabricated a PbS/ZnSb TEG with a 5% efficiency, and TEGs made of ZnSb/Constantan thermocouples were introduced in the Soviet Union to power radios by converting heat produced by kerosene lamps in rural, not electrified, areas, anticipating distributed energy generation. In the middle of the XX century also Peltier cells for cooling started to be considered, with Goldsmid's demonstration of cooling down to 0 °C with a Bi_2Te_3 based device. Such progresses were not sufficient to keep the field expanding, because of the limited efficiency which did not promise anything that could possibly compete with conventional engines. Nevertheless, TEGs continued to be developed since they found their niche applications where high reliability and limited or no need of maintenance were the dominant factors, such as generators for deep space missions. In this case TEGs have been employed starting from the late 60 s, on board the US spacecraft Navy Transit 4 A, to convert the heat generated by a decaying radioactive material in RTGs. In the 70 s TEGs were also adopted for biomedical applications, introduced for a limited period in small nuclear batteries in cardiac pacemakers.

Nanostructuration in the 90 s has strongly renewed the interest and allowed the field to regain momentum, spurring a wider community to look also for new and complex materials, which has largely enriched the technology, potentially allowing to more effectively tackle one of the goals of the present society towards environmental sustainability, i.e. energy efficiency. In this context, thermoelectrics is a solid and reliable technology that allows to increase the efficiency of a variety of processes characterized by the production of waste heat, by directly converting it into electricity. Among these processes are those involved in the heavy industry and the automotive sectors, to name a few. Not only, thanks to the downscaling of electronics, small devices now consume power in the range of μW and mW, and can thus be operated with batteries. In this framework, micro thermoelectric technology is a complementary solution to photovoltaics that allows to charge batteries exploiting small temperature differences. All applications require a further development of materials and devices at different temperature ranges, depending on applications, specifically targeting higher-performance, with non-toxic and sustainable thermoelectric materials.

With an historical approach, this review has discussed and compared the most studied classes of materials, underlining how they are positioned with respect to new challenges. Such classes comprise chalcogenides, silicides, skutterudites, Zintls, clathrates, Heusler, oxides, and more recently organics and composites. Below a comparative graph is presented (Fig. 31a–b), showing zT as a function of temperature for representative *p*- and *n*-type compounds of each different class. In Fig. 31c–d, for the same classes, the evolution of the record zT over time is displayed. Since the thermoelectric materials are designed and optimized to serve different applications and thus temperature ranges, the thermoelectric community roughly distinguishes among materials designed for low (below 450 K), medium (450–850 K) and high temperatures (above 850 K), even though the distinction is not neat, as different compounds belonging to the same class may achieve better thermoelectric performances in different temperature intervals. In the following, perspectives for the thermoelectric materials discussed within the framework of this review are presented according to the temperature range in which they best perform.

- **Low temperatures (below 450 K)**. The chalcogenides of bismuth, organic semiconductor and composites, and more recently silicon, are studied for thermoelectric applications in the low temperatures range. The chalcogenides of bismuth, which have played an important role in the history of thermoelectrics, continue to be a cornerstone in commercial technologies, with a record zT of 1.9 at 323 K for the compound $Bi_{0.5}Sb_{1.5}Te_3$ [161], achieved by incorporating grain boundary dislocations. One drawback of bismuth telluride-based materials is the scarcity of tellurium and the relative toxicity of both tellurium and bismuth, which poses a serious limitation to their mass production in the light of societies moving towards environmental sustainability. In the same temperature range, the relatively novel class of organic semiconductors is under investigation after a series of recent results reported very promising yet highly debated zT values [690]. Despite their generally lower performances with respect to other materials, they provide a number of alternative properties, such as flexibility and the possibility to process them from solution or melt, which represents significant potential for the design of flexible and light weight devices that can be cost-efficiently fabricated on large scales. In addition organic semiconducting molecules consist of abundant, non-toxic elements, and could be synthesized from renewable resources. All these properties make organic semiconductors and composites of interest for innovative niche applications, such as energy scavenging from irregular surfaces and/or wearables. However, while *p*- types have experienced significant progress in the last years, *n*-type materials are still lacking, mainly for environmental stability reasons. Composites of organic and/or inorganic materials are being explored for the same temperature range. While they provide similar characteristics to organic semiconductors when it comes to fabrication and sustainability, and little to no use of inorganic rare materials justifies its implementation, much effort should be put to

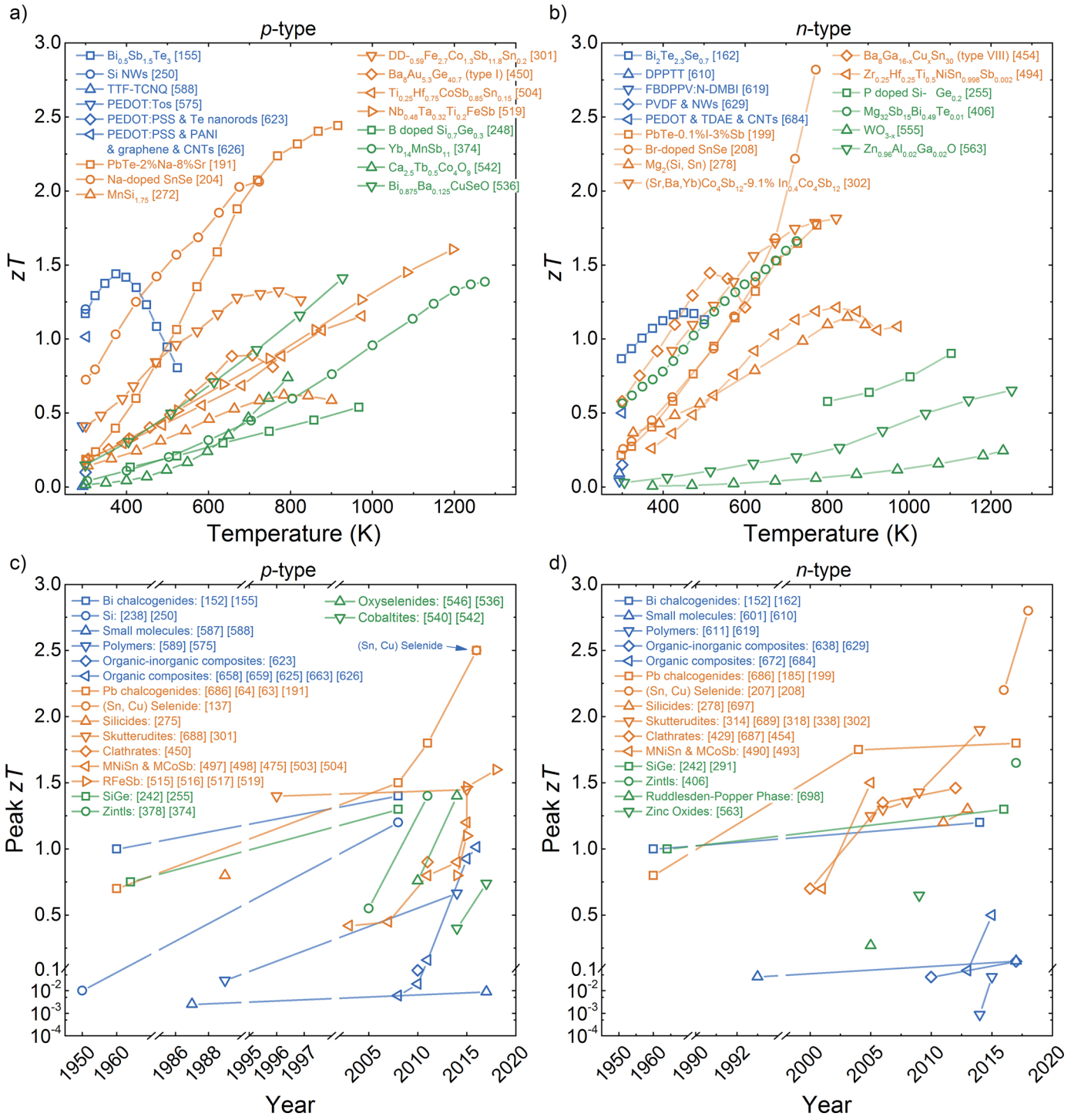

Fig. 31. zT versus temperature of p-type (a) and n-type (b) representative chalcogenides, silicides, skutterudites, Zintls, clathrates, Heusler, oxides, organic and composites. Evolution of zT for p-type (c) and n-type (d) chalcogenides, silicides, skutterudites, Zintls, clathrates, Heusler, oxides, organic and composites. The materials shown are grouped by temperature range in which they best perform. Materials for low, medium and high temperatures are shown in blue, brown and green, respectively. Since most of the early characterizations of organic materials were limited to the PF, the zT was calculated assuming $\kappa = 0.2\,\mathrm{W\,m^{-1}\,K^{-1}}$. This procedure is justified by the fact that the first organic materials were showing low σ. Some early measurements of the zT of chalcogenides are inaccurate due to poor measurements of κ. The peak zTs of those chalcogenides were extracted from Ref. [686]. Additional references used to build the figure and not reported elsewhere are [687–689,697,698] (for interpretation of the references to colour in this figure legend, the reader is referred to the web version of this article).

understand the role played by the interfaces inherent to these materials. Developing a better understanding and control over their type and number will surely result in further improvements. In this context, while energy-filtering has often been argued to justify observed performance increases, it continues to prove difficult to measure directly and without concurrently influencing other parameters. More recently, silicon has also been considered for room temperature applications. Its use in integrated thermoelectric generators was reported since 2002 [240] and was motivated by the obvious advantage of silicon full compatibility with planar technologies. This was considered prevalent over the well-assessed Si low zT. Recent results showing the possibility of increasing its

conversion efficiency [265,266,269] are further raising the interest on nanocrystalline silicon as a low-temperature thermoelectric material, coupling the advantages of materials integrability and technology low costs with more acceptable thermoelectric efficiencies.

- **Medium temperatures (450 K–850 K)**. The chalcogenides of lead, complex ternary chalcogenides, tin selenide and copper selenide, skutterudites, clathrates, half-heusler and silicides compounds are under extensive research for application in the mid temperature range. Lead chalcogenides were among the first materials to be used in commercial generators and have been exploited in the RTGs used by NASA since the 1960s. Lead telluride and its alloys continue to be top performing materials in the mid-temperature range, with Na-doped $Pb_{0.92}Sr_{0.08}Te$ displaying a remarkable average zT of 1.7 between 300 and 900 K (maximum zT of 2.5 at 923 K) [191]. These systems have isotropic transport properties due to their cubic crystal structure and can be sintered into mechanically stable pellets, which is an advantage in device fabrication. The toxicity of lead and scarcity of tellurium are potential impediments to using PbTe in wide-scale applications. SnSe has recently emerged as a new mid-temperature thermoelectric material that is composed of non-toxic, earth-abundant elements. Na-doped SnSe (*p*-type) exhibits a device zT of 1.34 between 300 and 773 K, while Br-doped SnSe (*n*-type) has a maximum zT of 2.8 at 773 K [208]. The remarkable performance in these materials is attributed to their anisotropic crystal structure and complex transport properties, but single crystal samples are typically needed for optimal performance. State of the art skutterudites currently achieve zT of 1.7 at 800 K, with the *n*-type performing better than the *p*-type. The scientific community is now exploring a variety of potential solutions to increase the zT of skutterudites even further. These include grain boundaries nanoengineering to increase phonon scattering and thus reducing the lattice thermal conductivity, to generate more disorder in the pnictogen rings, to study novel compositions with new elements for both filling and doping, together with a new theory that will help to focus that research, and to explore new synthesis methods to generate nanomaterials and/or nanoinclusions. Skutterudites are starting to be produced with high zT in large quantities by industrially scalable methods [691]. However, more research is still required on module/system optimization, including mechanical stability at high temperatures and thermal expansion mismatch between *p*- and *n*-type legs, in order to increase the final efficiency of the thermoelectric module, and reduce the final price per Watt. Inorganic clathrates have intrinsically low thermal conductivities owing to their unique guest-host crystal structures and influence of loosely bound guest atoms on the lattice dynamics. Since κ_{ph} of clathrates approaches the theoretical minimum value, high zTs are generally achieved by tuning the power factor, by judicious choice of framework substitution to reduce the carrier density [692] or tuning the band gap [448], while novel compositions with favorable electronic structure could yield higher power factors. New compositions are still being synthesized at an average rate of more than 10 new compositions per year (Fig. 21a), and novel compositions that might not have been predicted from simple chemical intuition have also been prepared [693,694]. It is therefore not unreasonable to expect that clathrate compositions with even better thermoelectric performance, perhaps at temperatures of interest for power generation, might be identified, provided current research efforts to improve the power factor continue. Bartholomé et al. have built thermoelectric modules based on Half-Heusler compounds from material synthesized in kg-batches [472]. The material performance is in line with the published values for comparable material compositions and exhibits peak zT values of 0.7 for *n*-type and 0.5 for *p*-type samples. The modules built from these materials have a total area of 25×25 mm^2 and generate a maximum power output of 2.8 W under a temperature difference of 527 K, which correspond to the highest power density ever reported for Half-Heusler modules, that is 3.2 W cm^{-2}. The long-term stability and reproducibility of these modules could be verified by the authors. One big issue that still needs to be resolved before HH materials could go to device production is the long-term stability as well as the chemical and mechanical resistance toward higher temperatures. Several groups are already focusing on this challenge. The results strongly underline the importance of phase separations as an important tool in the design of highly efficient thermoelectric materials [699]. For achieving the goal of a greater fundamental understanding and later on for the sophisticated design of phase separated HH compounds with thermoelectric properties beyond the state of the art, one has to clearly separate general effects of nanostructuring from material specific influences and work on a very detailed fundamental investigation of the crystallographic, mechanical, and thermoelectric properties of HH compounds. The relatively newer class of silicides, in particular Mg_2Si and HMSs, reach their highest zT between 625 and 850 K. The largest figure of merit of 1.4 at 800 K in Mg_2Si:Bi [290], along with the steady increase of zT over the last years, suggest that silicides could contribute to the manufacturing of segmented TEGs collecting waste heat from engines and industrial plants. However, especially for Mg_2Si, stability under practical conditions of use has to be further improved, and contact technology remains an issue [695].
- **High temperatures (above 850 K)**. Silicon-germanium alloys, oxides, and the recent Zinlt compounds are driving the research. SiGe preserve their records at very high temperature, with zTs values exceeding 1 between 1073 and 1273 K [291]. This prompted its extensive use in RTG, starting with the Multi-Hundred Watt Radioisotope Thermoelectric Generator developed by JPL to power the Voyager missions in 1977 [696]. Current state of the art bulk oxide thermoelectrics have zT approaching or even exceeding 1. The limitations to their breakthrough come from their characteristically low charge carrier mobility. Nevertheless, several studies have shown their potential [536,542,559,563]. Starting from compounds with layered or complex structures, characterized by a low κ, it is possible to tailor the charge carrier concentration by manipulating the anion oxygen content, and by decoupling the optimization of thermal and electrical properties. Nanostructuring and doping (or co-doping) on both cation and anion sites, can boost their thermoelectric efficiencies. Finally, the future of Zintl phases in thermoelectric applications will depend on several factors. Although many *p*-type Zintl phases perform quite well and have niche applications at high temperatures, recent first-principles calculations predict favorable *n*-type electronic properties in many different Zintl structure types. With the advent of new strategies for *n*-type doping, we may see significant improvements in this area. Further, there are many Zintl phases that have not yet been studied or optimized for thermoelectric applications, presenting many additional opportunities.

Overall, many efforts are ongoing towards more efficient and more easily implementable thermoelectrics. It appears plausible that beyond the niche, yet very exciting, field of space missions, thermoelectrics has now the potential to embrace a wider range of heat recovery applications. To make this possible, it is critically important to find new materials systems that have high figure of merit and are also composed of inexpensive, earth- abundant elements, in order to address the requirements imposed by sustainability criteria.

Clearly, constraints towards commercialization change depending on the target temperature range: at high temperatures, where a substantial amount of energy can be converted, the TEG has to produce energy savings larger than their energetic and monetary costs; at room temperature, they have to be able to convert a small amount of energy to operate, for example, a sensor at an almost negligible additional cost. Therefore different thermoelectric technologies will have to clearly address the corresponding challenges. In each case, however, a series of common criticalities have to be faced. These are not limited to the

materials used to fabricate the thermocouples, but involve the thermoelectric module as a whole, including electrical contacts: in fact, the module has to satisfy specific mechanical and thermal requirements, and it must preserve its thermal, electrical and mechanical properties over long periods and a large number of thermal cycles. Slightly different thermal expansions and/or mechanical response to thermal gradients in either the thermocouples, the electrical interconnections, the electrical insulators or the heat exchangers, may cause directional expansion with consequent fracture of the module over the mid-long term operation.

While in most cases general good guidance and successful architectural solutions have already been proposed, in some other cases, for example for solution processed materials or for textile-integrated thermoelectrics, the TEG architecture should be still, or further, developed in order to devise the best compromise between low-cost and energy conversion.

In the light of these considerations, it has to be clear that while zT represents a fundamental parameter that can be used for preliminary evaluations of the thermoelectric character of matter, it cannot be considered the only parameter when debating about applications. A more comprehensive evaluation that includes the thermoelectric performances of materials and modules as a whole in specific contexts, together with cost-benefit analysis, must be carried out case by case. In order for this to happen, it is becoming more and more important to further develop an intimate relationship between the fundamental research on materials and the applied research on the thermoelectric technology, as neither one of those can reach a breakthrough alone without the support of the other.

References

[1] L. Galvani, De viribus electricitatis in motu musculari: Commentarius, Bologna, Tip. Istituto delle Scienze, Bologna, 1791.
[2] A. Volta, Le Opere Di Alessandro Volta, Edizione Nazionale, Volume Primo, Ulrico Hoepli, Milan, (1918).
[3] M. Piccolino, Trends Neurosci. 20 (1997) 443–448.
[4] M. Piccolino, Brain Res. Bull. 46 (1998) 381–407.
[5] T.J. Seebeck, Ann. Phys. 82 (1826) 253–286.
[6] H.C. Oersted, Ann. Philos. 16 (1820) 273–277.
[7] P.M. Roget, Electricity, Galvanism, Magnetism, and Electro-Magnetism, Baldwin and Cradock of Paternoster-Row, London, 1832.
[8] L.I. Anatychuk, J. Thermoelectr. 2004–2 (2004) 5–11.
[9] http://thermoelectrics.matsci.northwestern.edu/thermoelectrics/history.html, last access 9/4/2018.
[10] H. Oersted, Ann. Phys. Chem. (1823) 430–432.
[11] J. Fourier, H. Oersted, Ann. Chim. Phys. 24 (1823) 375–389.
[12] J.C.A. Peltier, Ann. Chim. Phys. 56 (1834) 371–386.
[13] E. Lenz, Analen der Physik 120 (1838) 342–349.
[14] G. Magnus, Ann. Der Phys. Und Chemie 83 (1851) 469–504.
[15] W. Thomson, Math. Phys. Pap. 1 (1851) 175–183.
[16] W. Thomson, Proc. R. Soc. Edinburgh (1851).
[17] D.M. Rowe, Thermoelectrics Handbook: Macro to Nano, CRC/Taylor & Francis, Boca Raton, 2006.
[18] Lord Rayleigh, London, Edinburgh, Dublin Philos. Mag. J. Sci. 20 (1885) 361–363.
[19] K. Rankin, Electrical Installations of Electric Light, Power, Traction and Industrial Electrical Machinery, The Caxton Publisher CO, London, 1903.
[20] E. Altenkirch, Phys. Zeitschrift 12 (1911) 920–924.
[21] L. Onsager, Phys. Rev. 37 (1931) 405–426.
[22] L. Onsager, Phys. Rev. 38 (1931) 2265–2279.
[23] C.A. Domenicali, Rev. Mod. Phys. 26 (1954) 237–275.
[24] T.C. Harman, J.M. Honig, Thermoelectric and Thermomagnetic Effects and Applications, McGraw-Hill, New York, 1967.
[25] A.F. Ioffe, Semiconductor Thermoelements, and Thermoelectric Cooling, Infosearch, London, 1957.
[26] M. Telkes, J. Appl. Phys. 18 (1947) 1116–1127.
[27] H.J. Goldsmid, R.W. Douglas, Br. J. Appl. Phys. 5 (1954) 386.
[28] M.V. Vedernikov, E.K. Iordanishvili, Seventeenth International Conference on Thermoelectrics, Proceedings ICT98, (1998), pp. 37–42.
[29] R.P. Chasmar, R. Stratton, J. Electron. Control 7 (1959) 52–72.
[30] B.C. Blanke, J.H. Birden, K.C. Jordan, E.L. Murphy, Nuclear Battery-Thermocouple Type Summary Report, U.S. Atomic Energy Commission, 1960.
[31] V. Parsonnet, A.D. Berstein, G.Y. Perry, Am. J. Cardiol. 66 (1990) 837–842.
[32] https://www.orau.org/ptp/collection/Miscellaneous/pacemaker.html, last access 9/4/2018.
[33] J.D. Ryan, A. Lund, A.I. Hofmann, R. Kroon, R. Sarabia-Riquelme, M.C. Weisenberger, C. Müller, ACS Appl. Energy Mater. 1 (2018) 2934–2941.
[34] L.D. Hicks, M.S. Dresselhaus, Phys. Rev. B 47 (1993) 16631.
[35] L.D. Hicks, M.S. Dresselhaus, Phys. Rev. B 47 (1993) 727–731.
[36] L.D. Hicks, T.C. Harman, X. Sun, M.S. Dresselhaus, Phys. Rev. B 53 (1996) R10493.
[37] J.P. Heremans, C.M. Thrush, D.T. Morelli, M.-C. Wu, Phys. Rev. Lett. 88 (2002) 216801.
[38] M.S. Dresselhaus, G. Chen, M.Y. Tang, R.G. Yang, H. Lee, D.Z. Wang, Z.F. Ren, J.-P. Fleurial, P. Gogna, Adv. Mater. 19 (2007) 1043–1053.
[39] D.M. Rowe, CRC Handbook of Thermoelectrics, CRC/Taylor & Francis, Boca Raton, 1995.
[40] D.H. Meadows, J. Randers, D.L. Meadows, The Limits to Growth: The 30-Year Update, Chelsea Green Publishing, 2004.
[41] C.B. Vining, Nat. Mater. 8 (2009) 83–85.
[42] A. Shakouri, Mater. Res. 41 (2011) 399.
[43] International Energy Agency, IEA Publ. (2017), 1–71.
[44] REGULATION (EC) No 443/2009 OF THE EUROPEAN PARLIAMENT AND OF THE COUNCIL, Setting Emission Performance Standards for New Passenger Cars As Part of the Community's Integrated Approach to Reduce CO2 Emissions From Light-duty Vehicles, (2009).
[45] REGULATION OF THE EUROPEAN PARLIAMENT AND OF THE COUNCIL, Setting Emission Performance Standards for New Passenger Cars and for New Light Commercial Vehicles As Part of the Union's Integrated Approach to Reduce CO2 Emissions From Light-duty Vehicles and Amending Regulation (EC) No 715/2007 (Recast), (2017).
[46] H. Bottner, J. Nurnus, A. Schubert, F. Volkert, 26th Int. Conf. Thermoelectr., IEEE, (2007), (2007), pp. 306–309.
[47] D. Beretta, M. Massetti, G. Lanzani, M. Caironi, Rev. Sci. Instrum. 88 (2017) 015103.
[48] J.A. Lee, A.E. Aliev, J.S. Bykova, M.J. de Andrade, D. Kim, H.J. Sim, X. Lepró, A.A. Zakhidov, J.-B. Lee, G.M. Spinks, S. Roth, S.J. Kim, R.H. Baughman, Adv. Mater. 28 (2016) 5038–5044.
[49] D. Beretta, A. Perego, G. Lanzani, M. Caironi, Sustain. Energy Fuels 1 (2017) 174–190.
[50] G.J. Snyder, E.S. Toberer, Nature Publishing Group (2011), 101-110.
[51] G.J. Snyder, Appl. Phys. Lett. 84 (2004) 2436–2438.
[52] T. Caillat, J.-P. Fleurial, G.J. Snyder, A. Borshchevsky, Proceedings ICT2001. 20 International Conference on Thermoelectrics, (2002), pp. 282–285.
[53] G.J. Snyder, T.S. Ursell, Phys. Rev. Lett. 91 (2003) 148301.
[54] D.R. Lide, CRC Handbook of Chemistry and Physics, 85th ed., CRC/Taylor & Francis, Boca Raton, 2004.
[55] G.B. Haxel, J.B. Hedrick, G.J. Orris, U. S. Geol. Surv. Fact Sheet 087 (2002) 4.
[56] S. Leblanc, S.K. Yee, M.L. Scullin, C. Dames, K.E. Goodson, Renew. Sustain. Energy Rev. 32 (2014) 313–327.
[57] X. Shi, J. Yang, L. Wu, J.R. Salvador, C. Zhang, W.L. Villaire, D. Haddad, J. Yang, Y. Zhu, Q. Li, Sci. Rep. 5 (2015) 14641.
[58] X. Lu, W. Yao, G. Wang, X. Zhou, D. Morelli, Y. Zhang, H. Chi, S. Hui, C. Uher, J. Mater. Chem. A (2016) 17096–17103.
[59] X. Lu, D.T. Morelli, Y. Wang, W. Lai, Y. Xia, V. Ozolins, Chem. Mater. 28 (2016) 1781–1786.
[60] X. Lu, D.T. Morelli, Y. Xia, V. Ozolins, Chem. Mater. 27 (2015) 408–413.
[61] D. Connétable, V. Timoshevskii, E. Artacho, X. Blase, Phys. Rev. Lett. 87 (2001) 206405-1-206405–4.
[62] W. Lai, Y. Wang, D.T. Morelli, X. Lu, Adv. Funct. Mater. 25 (2015) 3648–3657.
[63] Y. Pei, X. Shi, A. LaLonde, H. Wang, L. Chen, G.J. Snyder, Nature 473 (2011) 66–69.
[64] J.P. Heremans, V. Jovovic, E.S. Toberer, A. Saramat, K. Kurosaki, A. Charoenphakdee, S. Yamanaka, G.J. Snyder, Science 321 (2008) 554–557.
[65] A. Page, C. Uher, P.F. Poudeu, A. Van Der Ven, Phys. Rev. B 92 (2015) 174102.
[66] K. Hattori, H. Miyazaki, K. Yoshida, M. Inukai, Y. Nishino, J. Appl. Phys. 117 (2015) 205102.
[67] K. Biswas, J. He, I.D. Blum, C.-I. Wu, T.P. Hogan, D.N. Seidman, V.P. Dravid, M.G. Kanatzidis, Nature 489 (2012) 414–418.
[68] S. Lee, P. Von Allmen, Appl. Phys. Lett. 88 (2006) 1–3.
[69] T. Yokobori, M. Okawa, K. Konishi, R. Takei, K. Katayama, S. Oozono, T. Shinmura, T. Okuda, H. Wadati, E. Sakai, K. Ono, H. Kumigashira, M. Oshima, T. Sugiyama, E. Ikenaga, N. Hamada, T. Saitoh, Phys. Rev. B 87 (2013) 195124.
[70] L. Xi, Y.B. Zhang, X.Y. Shi, J. Yang, X. Shi, L.D. Chen, W. Zhang, J. Yang, D.J. Singh, Phys. Rev. B 86 (2012) 155201.
[71] E. Flage-Larsen, Ø. Prytz, E.S. Toberer, A.F. May, Phys. Rev. B 81 (2010) 1–7.
[72] M. Van Schilfgaarde, T. Kotani, S. Faleev, Phys. Rev. Lett. 96 (2006) 226402.
[73] L. Cheng, H.J. Liu, J. Zhang, J. Wei, J.H. Liang, P.H. Jiang, D.D. Fan, L. Sun, J. Shi, Phys. Chem. Chem. Phys. 18 (2016) 17373–17379.
[74] G. Kresse, J. Furthmüller, J. Hafner, EPL 32 (1995) 729–734.
[75] K. Parlinski, Z.Q. Li, Y. Kawazoe, Phys. Rev. Lett. 81 (1998) 3298.
[76] P. Giannozzi, S. De Gironcoli, P. Pavone, S. Baroni, Phys. Rev. B 43 (1991) 7231–7242.
[77] X. Gonze, J.M. Beuken, R. Caracas, F. Detraux, M. Fuchs, G.M. Rignanese, L. Sindic, M. Verstraete, G. Zerah, F. Jollet, M. Torrent, A. Roy, M. Mikami, P. Ghosez, J.Y. Raty, D.C. Allan, Comput. Mater. Sci. 25 (2002) 478–492.
[78] L.T. Kong, Comput. Phys. Commun. 182 (2011) 2201–2207.
[79] J. Kang, L.W. Wang, Phys. Rev. B 96 (2017).
[80] D.R. Bowler, T. Miyazaki, J. Phys. Condens. Matter 22 (2010) 074207.
[81] C.K. Skylaris, P.D. Haynes, A.A. Mostofi, M.C. Payne, J. Chem. Phys. 122 (2005) 084119.
[82] S. Poncé, E.R. Margine, C. Verdi, F. Giustino, Comput. Phys. Commun. 209 (2016) 116–133.

[83] O. Hellman, D.A. Broido, Phys. Rev. B 90 (2014) 134309.
[84] V. Chiloyan, S. Huberman, Z. Ding, J. Mendoza, A.A. Maznev, K.A. Nelson, G. Chen, arXiv preprint arXiv:1711.07151 (2017).
[85] D.A. Broido, M. Malorny, G. Birner, N. Mingo, D.A. Stewart, Appl. Phys. Lett. 91 (2007) 231922.
[86] A.O. Oliynyk, E. Antono, T.D. Sparks, L. Ghadbeigi, M.W. Gaultois, B. Meredig, A. Mar, Chem. Mater. 28 (2016) 7324–7331.
[87] J. Carrete, W. Li, N. Mingo, S. Wang, S. Curtarolo, Phys. Rev. X 4 (2014) 011019.
[88] H. Zhu, G. Hautier, U. Aydemir, Z.M. Gibbs, G. Li, S. Bajaj, J.-H. Pöhls, D. Broberg, W. Chen, A. Jain, M.A. White, M. Asta, G.J. Snyder, K. Persson, G. Ceder, J. Mater. Chem. C 3 (2015) 10554–10565.
[89] G. Xing, J. Sun, Y. Li, X. Fan, W. Zheng, D.J. Singh, Phys. Rev. Mater. 1 (2017) 065405.
[90] X. Chen, D. Parker, D.J. Singh, Sci. Rep. 3 (2013) 3168.
[91] G.D. Mahan, J.O. Sofo, Proc. Natl. Acad. Sci. 93 (1996) 7436–7439.
[92] R. Kim, S. Datta, M.S. Lundstrom, J. Appl. Phys. 105 (2009) 034506.
[93] N. Neophytou, H. Kosina, Phys. Rev. B 83 (2011) 245305.
[94] N. Neophytou, H. Kosina, J. Appl. Phys. 112 (2012) 024305.
[95] S. Foster, M. Thesberg, N. Neophytou, Phys. Rev. B 96 (2017) 195425.
[96] J.E. Cornett, O. Rabin, Appl. Phys. Lett. 98 (2011) 182104.
[97] R. Kim, M.S. Lundstrom, J. Appl. Phys. 111 (2012) 024508.
[98] M. Thesberg, M. Pourfath, H. Kosina, N. Neophytou, J. Appl. Phys. 118 (2015) 224301.
[99] M. Zebarjadi, G. Joshi, G. Zhu, B. Yu, A. Minnich, Y. Lan, X. Wang, M. Dresselhaus, Z. Ren, G. Chen, Nano Lett. 11 (2011) 2225–2230.
[100] N. Neophytou, X. Zianni, H. Kosina, S. Frabboni, B. Lorenzi, D. Narducci, Nanotechnology 24 (2013) 205402.
[101] C. Jeong, S. Datta, M. Lundstrom, J. Appl. Phys. 111 (2012) 093708.
[102] Y.S. Ju, K.E. Goodson, Appl. Phys. Lett. 74 (1999) 3005–3007.
[103] J.A. Perez-Taborda, M. Muñoz Rojo, J. Maiz, N. Neophytou, M. Martin-Gonzalez, Sci. Rep. 6 (2016) 32778.
[104] J. Tang, H.-T. Wang, D.H. Lee, M. Fardy, Z. Huo, T.P. Russell, P. Yang, Nano Lett. 10 (2010) 4279–4283.
[105] B. Lorenzi, D. Narducci, R. Tonini, S. Frabboni, G.C. Gazzadi, G. Ottaviani, N. Neophytou, X. Zianni, J. Electron. Mater. 43 (2014) 3812–3816.
[106] J.M. Ziman, Endeavour 20 (1960) 555.
[107] T.J. Scheidemantel, C. Ambrosch-Draxl, T. Thonhauser, J.V. Badding, J.O. Sofo, Phys. Rev. B 68 (2003) 125210.
[108] J.M. Ziman, Principles of the Theory of Solids, Cambridge University Press, Cambridge, 1972.
[109] A. Matthiessen, C. Vogt, Philos. Trans. R. Soc. London 154 (1864) 167–200.
[110] Z. Aksamija, May 25-29, 2015, Rutgers Univ. New Brunswick, NJ, USA, Begellhouse, ConnecticutProceeding Proc. CHT-15. 6th Int. Symp. Adv. Comput. HEAT Transf.2015, Proceeding Proc. CHT-15. 6th Int. Symp. Adv. Comput. HEAT Transf. (2015) 6.
[111] S. Mazumder, A. Majumdar, J. Heat Transfer 123 (2001) 749.
[112] D. Lacroix, K. Joulain, D. Lemonnier, Phys. Rev. B 72 (2005) 064305.
[113] S. Wolf, N. Neophytou, H. Kosina, J. Appl. Phys. 115 (2014) 204306.
[114] S. Datta, Electronic Transport in Mesoscopic Systems, Cambridge university press, Cambridge, 1997.
[115] S.O. Koswatta, S. Hasan, M.S. Lundstrom, M.P. Anantram, D.E. Nikonov, IEEE Trans. Electron Devices 54 (2007) 2339–2351.
[116] P.K. Schelling, S.R. Phillpot, P. Keblinski, Phys. Rev. B 65 (2002) 144306.
[117] D. Donadio, G. Galli, Phys. Rev. Lett. 102 (2009) 195901.
[118] A.S. Henry, G. Chen, J. Comput. Theor. Nanosci. 5 (2008) 141–152.
[119] D.T. Morelli, V. Jovovic, J.P. Heremans, Phys. Rev. Lett. 101 (2008) 035901.
[120] A.J.H. McGaughey, M. Kaviany, Adv. Heat Transf. 39 (2006) 169–255.
[121] K. Termentzidis, T. Barreteau, Y. Ni, S. Merabia, X. Zianni, Y. Chalopin, P. Chantrenne, S. Volz, Phys. Rev. B 87 (2013) 125410.
[122] J. Meller, ELS, (2001), pp. 1–8.
[123] R. LeSar, Introduction to Computational Materials Science: Fundamentals to Applications, Cambridge University Press, Cambridge, 2013.
[124] Z. Tian, S. Lee, G. Chen, Annu. Rev. Heat Transf. (2014) 1–64.
[125] M.S. Green, J. Chem. Phys. 22 (1954) 398–413.
[126] R. Kubo, J. Phys. Soc. Japan 12 (1957) 570–586.
[127] F. Müller-Plathe, J. Chem. Phys. 106 (1997) 6082.
[128] S. Lee, K. Esfarjani, T. Luo, J. Zhou, Z. Tian, G. Chen, Nat. Commun. 5 (2014) 3525.
[129] J.R. Sootsman, D.Y. Chung, M.G. Kanatzidis, Angew. Chemie Int. Ed. 48 (2009) 8616–8639.
[130] M.D. Nielsen, V. Ozolins, J.P. Heremans, Energy Environ. Sci. 6 (2013) 570–578.
[131] F.J. DiSalvo, Science 285 (1999) 703–706.
[132] H.J. Goldsmid, Introduction to Thermoelectricity, Springer, Berlin Heidelberg, Berlin, Heidelberg, 2016.
[133] A.D. LaLonde, Y. Pei, H. Wang, G. Jeffrey Snyder, Mater. Today 14 (2011) 526–532.
[134] C. Wood, Rep. Prog. Phys. 51 (1988) 459–539.
[135] O. Delaire, A.F. May, M.A. McGuire, W.D. Porter, M.S. Lucas, M.B. Stone, D.L. Abernathy, V.A. Ravi, S.A. Firdosy, G.J. Snyder, Phys. Rev. B 80 (2009) 184302.
[136] A.F. May, D.J. Singh, G.J. Snyder, Phys. Rev. B 79 (2009) 153101.
[137] L.-D. Zhao, S.-H. Lo, Y. Zhang, H. Sun, G. Tan, C. Uher, C. Wolverton, V.P. Dravid, M.G. Kanatzidis, Nature 508 (2014) 373–377.
[138] H. Lin, G. Tan, J.-N. Shen, S. Hao, L.-M. Wu, N. Calta, C. Malliakas, S. Wang, C. Uher, C. Wolverton, M.G. Kanatzidis, Angew. Chemie Int. Ed. 55 (2016) 11431–11436.
[139] G. Tan, S. Hao, J. Zhao, C. Wolverton, M.G. Kanatzidis, J. Am. Chem. Soc. 139 (2017) 6467–6473.
[140] Y. Pei, C. Chang, Z. Wang, M. Yin, M. Wu, G. Tan, H. Wu, Y. Chen, L. Zheng, S. Gong, T. Zhu, X. Zhao, L. Huang, J. He, M.G. Kanatzidis, L.-D. Zhao, J. Am. Chem. Soc. 138 (2016) 16364–16371.
[141] L.-D. Zhao, C. Chang, G. Tan, M.G. Kanatzidis, Energy Environ. Sci. 9 (2016) 3044–3060.
[142] C. Han, Q. Sun, Z. Li, S.X. Dou, Adv. Energy Mater. 6 (2016) 1600498.
[143] G. Tan, L.-D. Zhao, M.G. Kanatzidis, Chem. Rev. 116 (2016) 12123–12149.
[144] H.J. Goldsmid, A.R. Sheard, D.A. Wright, Br. J. Appl. Phys. 9 (1958) 365–370.
[145] H.J. Goldsmid, J. Appl. Phys. 32 (1961) 2198–2202.
[146] ESMARK, Trans. Geol. Soc. London s1-3 (1816) 413–414.
[147] S.J. Youn, A.J. Freeman, Phys. Rev. B 63 (2001) 085112.
[148] H. Köhler, Phys. Status Solidi B 74 (1976) 591.
[149] G. Wang, T. Cagin, Phys. Rev. B 76 (2007) 075201.
[150] J.E.E.A. Hoffmann, Kirk-Othmer Encycl. Chem. Technol. 16 (2011) 1–30.
[151] J. Jiang, L. Chen, S. Bai, Q. Yao, Q. Wang, Scr. Mater. 52 (2005) 347–351.
[152] H.J. Goldsmid, Materials (Basel) 7 (2014) 2577–2592.
[153] H.-S. Kim, N.A. Heinz, Z.M. Gibbs, Y. Tang, S.D. Kang, G.J. Snyder, Mater. Today 20 (2017) 452–459.
[154] W. Xie, X. Tang, Y. Yan, Q. Zhang, T.M. Tritt, Appl. Phys. Lett. 94 (2009) 102111.
[155] B. Poudel, Q. Hao, Y. Ma, Y. Lan, A. Minnich, B. Yu, X. Yan, D. Wang, A. Muto, D. Vashaee, X. Chen, J. Liu, M.S. Dresselhaus, G. Chen, Z. Ren, Science 320 (2008) 634–638.
[156] A. Soni, Z. Yanyuan, Y. Ligen, M.K.K. Aik, M.S. Dresselhaus, Q. Xiong, Nano Lett. 12 (2012) 1203–1209.
[157] S. Wang, H. Li, R. Lu, G. Zheng, X. Tang, Nanotechnology 24 (2013) 285702.
[158] L. Yang, Z.G. Chen, M.S. Dargusch, J. Zou, Adv. Energy Mater. (2017) 1701797.
[159] G. Zheng, X. Su, H. Xie, Y. Shu, T. Liang, X. She, W. Liu, Y. Yan, Q. Zhang, C. Uher, M.G. Kanatzidis, X. Tang, Energy Environ. Sci. 10 (2017) 2638–2652.
[160] J.-J. Shen, T.-J. Zhu, X.-B. Zhao, S.-N. Zhang, S.-H. Yang, Z.-Z. Yin, Energy Environ. Sci. 3 (2010) 1519.
[161] S. Il Kim, K.H. Lee, H.A. Mun, H.S. Kim, S.W. Hwang, J.W. Roh, D.J. Yang, W.H. Shin, X.S. Li, Y.H. Lee, G.J. Snyder, S.W. Kim, Science 348 (2015) 109–114.
[162] L. Hu, T. Zhu, X. Liu, X. Zhao, Adv. Funct. Mater. 24 (2014) 5211–5218.
[163] J. He, L.D. Zhao, J.C. Zheng, J.W. Doak, H. Wu, H.Q. Wang, Y. Lee, C. Wolverton, M.G. Kanatzidis, V.P. Dravid, J. Am. Chem. Soc. 135 (2013) 4624–4627.
[164] Y. Pei, H. Wang, G.J. Snyder, Adv. Mater. 24 (2012) 6125–6135.
[165] L.-D. Zhao, J. He, S. Hao, C.-I. Wu, T.P. Hogan, C. Wolverton, V.P. Dravid, M.G. Kanatzidis, J. Am. Chem. Soc. 134 (2012) 16327–16336.
[166] The American Journal of Science., J.D. & E.S. Dana, New-Haven, 1880.
[167] W.G. Zeier, A. Zevalkink, Z.M. Gibbs, G. Hautier, M.G. Kanatzidis, G.J. Snyder, Angew. Chemie Int. Ed. 55 (2016) 6826–6841.
[168] Z.M. Gibbs, H. Kim, H. Wang, R.L. White, F. Drymiotis, M. Kaviany, G. Jeffrey Snyder, Appl. Phys. Lett. 103 (2013) 262109.
[169] G. Li, U. Aydemir, B. Duan, M.T. Agne, H. Wang, M. Wood, Q. Zhang, P. Zhai, W.A. Goddard, G.J. Snyder, ACS Appl. Mater. Interfaces 9 (2017) 40488–40496.
[170] J.E. Petersen, L.M. Scolfaro, T.H. Myers, Mater. Chem. Phys. 146 (2014) 472–477.
[171] J.R. Sootsman, J. He, V.P. Dravid, S. Ballikaya, D. Vermeulen, C. Uher, M.G. Kanatzidis, Chem. Mater. 22 (2010) 869–875.
[172] J.R. Sootsman, J. He, V.P. Dravid, C.-P. Li, C. Uher, M.G. Kanatzidis, J. Appl. Phys. 105 (2009) 083718.
[173] Y.I. Ravich, B.A. Efimova, I.A. Smirnov, Semiconducting Lead Chalcogenides, Springer, Boston, 1970.
[174] A.F. Ioffe, L.S. Stil'bans, E.K. Iordanishvili, T.S. Stavitskaya, A. Gelbtuch, G. Vineyard, Phys. Today 12 (1959) 42–42.
[175] Y. Pei, A. LaLonde, S. Iwanaga, G.J. Snyder, Energy Environ. Sci. 4 (2011) 2085.
[176] A.D. LaLonde, Y. Pei, G.J. Snyder, Energy Environ. Sci. 4 (2011) 2090.
[177] H. Wang, Y. Pei, A.D. LaLonde, G.J. Snyder, Proc. Natl. Acad. Sci. U. S. A. 109 (2012) 9705–9709.
[178] H. Wang, Y. Pei, A.D. LaLonde, G.J. Snyder, Adv. Mater. 23 (2011) 1366–1370.
[179] L.-D. Zhao, S.-H. Lo, J. He, H. Li, K. Biswas, J. Androulakis, C.-I. Wu, T.P. Hogan, D.-Y. Chung, V.P. Dravid, M.G. Kanatzidis, J. Am. Chem. Soc. 133 (2011) 20476–20487.
[180] H. Wang, E. Schechtel, Y. Pei, G.J. Snyder, Adv. Energy Mater. 3 (2013) 488–495.
[181] L.-D. Zhao, S. Hao, S.-H. Lo, C.-I. Wu, X. Zhou, Y. Lee, H. Li, K. Biswas, T.P. Hogan, C. Uher, C. Wolverton, V.P. Dravid, M.G. Kanatzidis, J. Am. Chem. Soc. 135 (2013) 7364–7370.
[182] M.G. Kanatzidis, Chem. Mater. 22 (2010) 648–659.
[183] M.G. Kanatzidis, MRS Bull. 40 (2015) 687–695.
[184] C.J. Vineis, A. Shakouri, A. Majumdar, M.G. Kanatzidis, Adv. Mater. 22 (2010) 3970–3980.
[185] K.F. Hsu, S. Loo, F. Guo, W. Chen, J.S. Dyck, C. Uher, T. Hogan, E.K. Polychroniadis, M.G. Kanatzidis, Science 303 (2004) 818–821.
[186] P.F.P. Poudeu, J. D'Angelo, A.D. Downey, J.L. Short, T.P. Hogan, M.G. Kanatzidis, Angew. Chemie Int. Ed. 45 (2006) 3835–3839.
[187] Z. Chen, Z. Jian, W. Li, Y. Chang, B. Ge, R. Hanus, J. Yang, Y. Chen, M. Huang, G.J. Snyder, Y. Pei, Adv. Mater. 29 (2017) 1606768.
[188] L. Zheng, W. Li, S. Lin, J. Li, Z. Chen, Y. Pei, ACS Energy Lett. 2 (2017) 563–568.
[189] H. Wang, Z.M. Gibbs, Y. Takagiwa, G.J. Snyder, Energy Environ. Sci. 7 (2014) 804–811.
[190] K. Biswas, J. He, Q. Zhang, G. Wang, C. Uher, V.P. Dravid, M.G. Kanatzidis, Nat. Chem. 3 (2011) 160–166.
[191] G. Tan, F. Shi, S. Hao, L.-D. Zhao, H. Chi, X. Zhang, C. Uher, C. Wolverton, V.P. Dravid, M.G. Kanatzidis, Nat. Commun. 7 (2016) 12167.
[192] Y. Xiao, H. Wu, W. Li, M. Yin, Y. Pei, Y. Zhang, L. Fu, Y. Chen, S.J. Pennycook,

L. Huang, J. He, L.-D. Zhao, J. Am. Chem. Soc. (2017) 18732–18738.
[193] L.D. Zhao, H.J. Wu, S.Q. Hao, C.I. Wu, X.Y. Zhou, K. Biswas, J.Q. He, T.P. Hogan, C. Uher, C. Wolverton, V.P. Dravid, M.G. Kanatzidis, Energy Environ. Sci. 6 (2013) 3346.
[194] Y. Pei, G. Tan, D. Feng, L. Zheng, Q. Tan, X. Xie, S. Gong, Y. Chen, J.-F. Li, J. He, M.G. Kanatzidis, L.-D. Zhao, Adv. Energy Mater. 7 (2017) 1601450.
[195] L.-D. Zhao, V.P. Dravid, M.G. Kanatzidis, Energy Environ. Sci. 7 (2014) 251–268.
[196] L.-D. Zhao, J. He, C.-I. Wu, T.P. Hogan, X. Zhou, C. Uher, V.P. Dravid, M.G. Kanatzidis, J. Am. Chem. Soc. 134 (2012) 7902–7912.
[197] J. Zhang, D. Wu, D. He, D. Feng, M. Yin, X. Qin, J. He, Adv. Mater. 29 (2017) 1703148.
[198] Y. Lee, S.-H. Lo, C. Chen, H. Sun, D.-Y. Chung, T.C. Chasapis, C. Uher, V.P. Dravid, M.G. Kanatzidis, Nat. Commun. 5 (2014) 3640.
[199] L. Fu, M. Yin, D. Wu, W. Li, D. Feng, L. Huang, J. He, Energy Environ. Sci. 10 (2017) 2030–2040.
[200] M. Zhou, G.J. Snyder, L. Li, L.-D. Zhao, Inorg. Chem. Front. 3 (2016) 1449–1463.
[201] G. Shi, E. Kioupakis, J. Appl. Phys. 117 (2015) 065103.
[202] C.W. Wang, Y.Y.Y. Xia, Z. Tian, J. Jiang, B.H. Li, S.T. Cui, H.F. Yang, A.J. Liang, X.Y. Zhan, G.H. Hong, S. Liu, C. Chen, M.X. Wang, L.X. Yang, Z. Liu, Q.X. Mi, G. Li, J.M. Xue, Z.K. Liu, Y.L. Chen, Phys. Rev. B 96 (2017) 165118.
[203] Q. Tan, L.-D. Zhao, J.-F. Li, C.-F. Wu, T.-R. Wei, Z.-B. Xing, M.G. Kanatzidis, J. Mater. Chem. A 2 (2014) 17302–17306.
[204] L.-D. Zhao, G. Tan, S. Hao, J. He, Y. Pei, H. Chi, H. Wang, S. Gong, H. Xu, V.P. Dravid, C. Uher, G.J. Snyder, C. Wolverton, M.G. Kanatzidis, Science 351 (2016) 141–144.
[205] K. Peng, X. Lu, H. Zhan, S. Hui, X. Tang, G. Wang, J. Dai, C. Uher, G. Wang, X. Zhou, Energy Environ. Sci. Energy Environ. Sci. 454 (2016) 454–460.
[206] X. Wang, J. Xu, G.-Q. Liu, X. Tan, D. Li, H. Shao, T. Tan, J. Jiang, NPG Asia Mater. 9 (2017) e426.
[207] A.T. Duong, V.Q. Nguyen, G. Duvjir, V.T. Duong, S. Kwon, J.Y. Song, J.K. Lee, J.E. Lee, S. Park, T. Min, J. Lee, J. Kim, S. Cho, Nat. Commun. 7 (2016) 1–6.
[208] C. Chang, M. Wu, D. He, Y. Pei, C.-F. Wu, X. Wu, H. Yu, F. Zhu, K. Wang, Y. Chen, L. Huang, J.-F. Li, J. He, L.-D. Zhao, Science 360 (2018) 778–783.
[209] T.-R. Wei, G. Tan, C.-F. Wu, C. Chang, L.-D. Zhao, J.-F. Li, G.J. Snyder, M.G. Kanatzidis, Appl. Phys. Lett. 110 (2017) 053901.
[210] T.-R. Wei, G. Tan, X. Zhang, C.-F. Wu, J.-F. Li, V.P. Dravid, G.J. Snyder, M.G. Kanatzidis, J. Am. Chem. Soc. 138 (2016) 8875–8882.
[211] C.-L. Chen, H. Wang, Y.-Y. Chen, T. Day, G.J. Snyder, J. Mater. Chem. A 2 (2014) 11171–11176.
[212] Y.K. Lee, K. Ahn, J. Cha, C. Zhou, H.S. Kim, G. Choi, S.I. Chae, J.-H. Park, S.-P. Cho, S.H. Park, Y.-E. Sung, W.B. Lee, T. Hyeon, I. Chung, J. Am. Chem. Soc. 139 (2017) 10887–10896.
[213] H. Liu, X. Yuan, P. Lu, X. Shi, F. Xu, Y. He, Y. Tang, S. Bai, W. Zhang, L. Chen, Y. Lin, L. Shi, H. Lin, X. Gao, X. Zhang, H. Chi, C. Uher, Adv. Mater. 25 (2013) 6607–6612.
[214] B. Zhong, Y. Zhang, W. Li, Z. Chen, J. Cui, W. Li, Y. Xie, Q. Hao, Q. He, Appl. Phys. Lett. 105 (2014) 123902.
[215] B. Yu, W. Liu, S. Chen, H. Wang, H. Wang, G. Chen, Z. Ren, Nano Energy 1 (2012) 472–478.
[216] Y. He, T. Day, T. Zhang, H. Liu, X. Shi, L. Chen, G.J. Snyder, Adv. Mater. 26 (2014) 3974–3978.
[217] Z.-H. Ge, B.-P. Zhang, Y.-X. Chen, Z.-X. Yu, Y. Liu, J.-F. Li, Chem. Commun. 47 (2011) 12697.
[218] D.R. Brown, T. Day, T. Caillat, G.J. Snyder, J. Electron. Mater. 42 (2013) 2014–2019.
[219] G. Dennler, R. Chmielowski, S. Jacob, F. Capet, P. Roussel, S. Zastrow, K. Nielsch, I. Opahle, G.K.H. Madsen, Adv. Energy Mater. 4 (2014) 1301581.
[220] H. Liu, X. Shi, F. Xu, L. Zhang, W. Zhang, L. Chen, Q. Li, C. Uher, T. Day, G.J. Snyder, Nat. Mater. 11 (2012) 422–425.
[221] A.A. Olvera, N.A. Moroz, P. Sahoo, P. Ren, T.P. Bailey, A.A. Page, C. Uher, P.F.P. Poudeu, Energy Environ. Sci. 10 (2017) 1668–1676.
[222] X. Lu, D.T. Morelli, Y. Xia, F. Zhou, V. Ozolins, H. Chi, X. Zhou, C. Uher, Adv. Energy Mater. 3 (2013) 342–348.
[223] E.J. Skoug, D.T. Morelli, Phys. Rev. Lett. 107 (2011) 235901.
[224] D.I. Bilc, S.D. Mahanti, T. Kyratsi, D.Y. Chung, M.G. Kanatzidis, P. Larson, Phys. Rev. B 71 (2005) 085116.
[225] J. Gui, M. Ji, J. Liu, M. Xu, J. Zhang, H. Zhu, Angew. Chemie 127 (2015) 3754–3758.
[226] A. Assoud, S. Thomas, B. Sutherland, H. Zhang, T.M. Tritt, H. Kleinke, Chem. Mater. 18 (2006) 3866–3872.
[227] M.G. Kanatzidis, Semicond. Semimetals 69 (2001) 51–100.
[228] D.-Y. Chung, T. Hogan, P. Brazis, M. Rocci- Lane, C. Kannewurf, M. Bastea, C. Uher, M.G. Kanatzidis, Science 287 (2000) 1024–1027.
[229] J. Schilz, V.N. Romanenko, J. Mater. Sci. Mater. Electron. 6 (1995) 265–279.
[230] D.R. Lide, CRC Handbook of Chemistry and Physics, 85th ed., CRC/Taylor & Francis, Boca Raton, 2004.
[231] W. Liu, K. Yin, Q. Zhang, C. Uher, X. Tang, Natl. Sci. Rev. 4 (2017) 611–626.
[232] A. Nozariasbmarz, A. Agarwal, Z.A. Coutant, M.J. Hall, J. Liu, R. Liu, A. Malhotra, P. Norouzzadeh, M.C. Öztürk, V.P. Ramesh, Y. Sargolzaeiaval, F. Suarez, D. Vashaee, J. Appl. Phys. 56 (2017) 05DA04.
[233] G. Mueller, Cryst. Res. Technol. 42 (2007) 1150–1161.
[234] R.A. Lefever, G.L. McVay, R.J. Baughman, Mater. Res. Bull. 9 (1974) 863–872.
[235] F.A. Padovani, M.B. Miller, J.A. Moore, J.H. Fowler, M.N. June, J.D. Matthews, T. R. Morton, N.A. Stotko, L.B. Palmer, US Patent 4,092,446 (1978).
[236] V. Domnich, Y. Aratyn, W.M. Kriven, Y. Gogotsi, Rev. Adv. Mater. Sci 17 (2008) 33–41.
[237] Y. Miyazaki, D. Igarashi, K. Hayashi, T. Kajitani, K. Yubuta, Phys. Rev. B - Condens. Matter Mater. Phys. 78 (2008) 1–8.
[238] T. Geballe, G. Hull, Phys. Rev. 98 (1955) 940–947.
[239] A. Stranz, J. Kaehler, A. Waag, E. Peiner, J. Electron. Mater. 42 (2013) 2381–2387.
[240] M. Strasser, R. Aigner, M. Franosch, G. Wachutka, Sensors Actuators, A Phys. 97–98 (2002) 535–542.
[241] Z. Yuan, K. Ziouche, Z. Bougrioua, P. Lejeune, T. Lasri, D. Leclercq, Sens. Actuators, A 221 (2015) 67–76.
[242] J.P. Dismukes, L. Ekstrom, E.F. Steigmeier, I. Kudman, D.S. Beers, J. Appl. Phys. 35 (1964) 2899–2907.
[243] D.M. Rowe, V.S. Shukla, N. Savvides, Nature 290 (1981) 765–766.
[244] C.B. Vining, W. Laskow, J.O. Hanson, R.R. Van der Beck, P.D. Gorsuch, J. Appl. Phys. 69 (1991) 4333–4340.
[245] C.B. Vining, The Thermoelectric Properties of Boron-doped Silicon and Silicon-germanium in the As-Hot Pressed Conditions, JPL/Calif. Inst. Of Tech. Technical Report, (1988).
[246] S. Loughin, D.X. Centurioni, A.G. Robison, J.J. Maley, J.P. Fleurial, AIP Conf. Proc. 271 (1993) 747–752.
[247] X.W. Wang, H. Lee, Y.C. Lan, G.H. Zhu, G. Joshi, D.Z. Wang, J. Yang, A.J. Muto, M.Y. Tang, J. Klatsky, S. Song, M.S. Dresselhaus, G. Chen, Z.F. Ren, Appl. Phys. Lett. 93 (2008) 19–21.
[248] A.J. Minnich, H. Lee, X.W. Wang, G. Joshi, M.S. Dresselhaus, Z.F. Ren, G. Chen, D. Vashaee, Phys. Rev. B 80 (2009) 155327.
[249] M.S. El-Genk, H.H. Saber, Energy Convers. Manage. 44 (2003) 1069–1088.
[250] A.I. Boukai, Y. Bunimovich, J. Tahir- Kheli, J.-K.K. Yu, W.A. Goddard, J.R. Heath, Nature 451 (2008) 168–171.
[251] A. Hochbaum, R. Chen, R. Delgado, Nature 451 (2008) 163–167.
[252] R. Cheaito, J.C. Duda, T.E. Beechem, K. Hattar, J.F. Ihlefeld, D.L. Medlin, M.A. Rodriguez, M.J. Campion, E.S. Piekos, P.E. Hopkins, Phys. Rev. Lett. 109 (2012) 195901.
[253] J.A. Martinez, P.P. Provencio, S.T. Picraux, J.P. Sullivan, B.S. Swartzentruber, J. Appl. Phys. 110 (2011) 074317.
[254] E.K. Lee, L. Yin, Y. Lee, J.W. Lee, S.J. Lee, J. Lee, S.N. Cha, D. Whang, G.S. Hwang, K. Hippalgaonkar, A. Majumdar, C. Yu, B.L. Choi, J.M. Kim, K. Kim, Nano Lett. 12 (2012) 2918–2923.
[255] X.W. Wang, H. Lee, Y.C. Lan, G.H. Zhu, G. Joshi, D.Z. Wang, J. Yang, A.J. Muto, M.Y. Tang, J. Klatsky, S. Song, M.S. Dresselhaus, G. Chen, Z.F. Ren, Appl. Phys. Lett. 93 (2008) 193121.
[256] K.-Q. Peng, X. Wang, L. Li, Y. Hu, S.-T. Lee, Nano Today 8 (2013) 75–97.
[257] D. Dávila, A. Tarancón, C. Calaza, M. Salleras, M. Fernández-Regúlez, A. San Paulo, L. Fonseca, Nano Energy 1 (2012) 812–819.
[258] J. Choi, K. Cho, S. Kim, Adv. Energy Mater. 7 (2017) 1602138.
[259] J. Lim, K. Hippalgaonkar, S.C. Andrews, A. Majumdar, Nano Lett. 12 (2012) 2475–2482.
[260] S. Neogi, J.S. Reparaz, L.F.C. Pereira, B. Graczykowski, M.R. Wagner, M. Sledzinska, A. Shchepetov, M. Prunnila, J. Ahopelto, C.M. Sotomayor- Torres, D. Donadio, ACS Nano 9 (2015) 3820–3828.
[261] S. Neogi, D. Donadio, Eur. Phys. J. B 88 (2015) 73.
[262] J. Lee, J. Lim, P. Yang, Nano Lett. 15 (2015) 3273–3279.
[263] D. Narducci, S. Frabboni, X. Zianni, J. Mater. Chem. C 3 (2015) 12176–12185.
[264] V. Kessler, D. Gautam, T. Huelser, M. Spree, R. Theissmann, M. Winterer, H. Wiggers, G. Schierning, R. Schmechel, Adv. Energy Mater. 15 (2013) 379–385.
[265] G.F. Cerofolini, M. Ferri, E. Romano, A. Roncaglia, E. Selezneva, A. Arcari, F. Suriano, G.P. Veronese, S. Solmi, D. Narducci, 8th Conf. Thermoelectr. (2010), pp. 147–151.
[266] D. Narducci, E. Selezneva, G. Cerofolini, S. Frabboni, G. Ottaviani, J. Solid State Chem. 193 (2012) 19–25.
[267] D. Narducci, B. Lorenzi, X. Zianni, N. Neophytou, S. Frabboni, G.C. Gazzadi, A. Roncaglia, F. Suriano, Phys. Status Solidi 1258 (2014) 1255–1258.
[268] A. Yusufu, K. Kurosaki, Y. Miyazaki, M. Ishimaru, A. Kosuga, Y. Ohishi, H. Muta, S. Yamanaka, Nanoscale 6 (2014) 13921–13927.
[269] N.S. Bennett, N.M. Wight, S.R. Popuri, J.-W.G. Bos, Nano Energy 16 (2015) 350–356.
[270] B. Yu, M. Zebarjadi, H. Wang, K. Lukas, H. Wang, D. Wang, C. Opeil, M. Dresselhaus, G. Chen, Z. Ren, Nano Lett. 12 (2012) 2077–2082.
[271] K. Favier, G. Bernard-Granger, C. Navone, M. Soulier, M. Boidot, J. Leforestier, J. Simon, J.-C. Tedenac, D. Ravot, Acta Mater. 64 (2014) 429–442.
[272] W. Luo, H. Li, Y. Yan, Z. Lin, X. Tang, Q. Zhang, C. Uher, Intermetallics 19 (2011) 404–408.
[273] K. Kondoh, H. Oginuma, E. Yuasa, T. Aizawa, Mater. Trans. 42 (2001) 1293–1300.
[274] E.N. Nikitin, Sov. Phys. Tech. Phys. 3 (1958) 20.
[275] N.D. Marchuck, V.K. Zaitsev, M.I. Fedorov, A.E. Kaliazin, 8th Int. Conf. Thermoelectr. Energy Convers., Nancy, (1989), p. 210.
[276] E. Groβ, M. Riffel, U. Stöhrer, J. Mater. Res. 10 (1995) 34–40.
[277] A.J. Zhou, T.J. Zhu, X.B. Zhao, S.H. Yang, T. Dasgupta, C. Stiewe, R. Hassdorf, E. Mueller, J. Electron. Mater. 39 (2010) 2002–2007.
[278] M.I. Fedorov, V.K. Zaitsev, G.N. Isachenko, Solid State Phenom. 170 (2011) 286–292.
[279] N. Mingo, D. Hauser, N.P. Kobayashi, M. Plissonnier, a Shakouri, Nano Lett. 9 (2009) 711–715.
[280] Q.R. Hou, Z.M. Wang, Y.J. He, Appl. Phys. A Mater. Sci. Process. 80 (2005) 1807–1811.
[281] I. Aoyama, H. Kaibe, L. Rauscher, T. Kanda, M. Mukoujima, S. Sano, T. Tsuji, Jpn. J. Appl. Phys., Part 1 Regul. Pap. Short Notes Rev. Pap. 44 (2005) 4275–4281.
[282] J.M. Higgins, A.L. Schmitt, I.A. Guzei, S. Jin, J. Am. Chem. Soc. 130 (2008) 16086–16094.

[283] T. Itoh, M. Yamada, J. Electron. Mater. 38 (2009) 925–929.
[284] A.J. Zhou, X.B. Zhao, T.J. Zhu, S.H. Yang, T. Dasgupta, C. Stiewe, R. Hassdorf, E. Mueller, Mater. Chem. Phys. 124 (2010) 1001–1005.
[285] W. Luo, H. Li, F. Fu, W. Hao, X. Tang, J. Electron. Mater. 40 (2011) 1233–1237.
[286] W. Li, L. Lindsay, D.A. Broido, D.A. Stewart, N. Mingo, Phys. Rev. B 86 (2012) 174307.
[287] S.-W. You, K.-H. Park, I.-H. Kim, S.-M. Choi, W.-S. Seo, S.-U. Kim, J. Electron. Mater. 41 (2012) 1675–1679.
[288] M. Ioannou, G. Polymeris, E. Hatzikraniotis, A.U. Khan, K.M. Paraskevopoulos, T. Kyratsi, J. Electron. Mater. 42 (2013) 1827–1834.
[289] S. Battiston, S. Fiameni, M. Saleemi, S. Boldrini, A. Famengo, F. Agresti, M. Stingaciu, M.S. Toprak, M. Fabrizio, S. Barison, J. Electron. Mater. 42 (2013) 1956–1959.
[290] R.D. Schmidt, E.D. Case, J. Giles III, J.E. Ni, T.P. Hogan, J. Electron. Mater. 41 (2012) 1210–1216.
[291] A. Nozariasbmarz, P. Roy, Z. Zamanipour, J.H. Dycus, M.J. Cabral, J.M. LeBeau, J.S. Krasinski, D. Vashaee, APL Mater. 4 (2016) 104814.
[292] Y. Gelbstein, J. Tunbridge, R. Dixon, M.J. Reece, H. Ning, R. Gilchrist, R. Summers, I. Agote, M.A. Lagos, K. Simpson, C. Rouaud, P. Feulner, S. Rivera, R. Torrecillas, M. Husband, J. Crossley, I. Robinson, J. Electron. Mater. 43 (2014) 1703–1711.
[293] Z. Li, J.-F. Dong, F.-H. Sun, S. Hirono, J.-F. Li, Chem. Mater. 29 (2017) 7378–7389.
[294] I. Oftedal, Nor. Geol. Tidsskr. 8 (1926) 250–257.
[295] I. Oftedal, Zeitschrift Für Krist. - Cryst. Mater. 66 (1928) 517–546.
[296] T.M." Tritt, Recent Trends Thermoelectr. Mater. Res. 71 (2000).
[297] A. Kjekshus, T. Rakke, Acta Chem. Scand. A 28 (1974).
[298] M. Rull-Bravo, A. Moure, J.F. Fernández, M. Martín-González, RSC Adv. 5 (2015) 41653–41667.
[299] D.J. Singh, W.E. Pickett, Phys. Rev. B 50 (1994) 11235–11238.
[300] T. Caillat, J. Fleurial, a Borshchevsky, J. Cryst. Growth 166 (1996) 722–726.
[301] G. Rogl, A. Grytsiv, P. Heinrich, E. Bauer, P. Kumar, N. Peranio, O. Eibl, J. Horky, M. Zehetbauer, P. Rogl, Acta Mater. 91 (2015) 227–238.
[302] G. Rogl, A. Grytsiv, K. Yubuta, S. Puchegger, E. Bauer, C. Raju, R.C. Mallik, P. Rogl, Acta Mater. 95 (2015) 201–211.
[303] G. Rogl, P. Rogl, Curr. Opin. Green Sustain. Chem. 4 (2017) 50–57.
[304] Fitriani, R. Ovik, B.D. Long, M.C. Barma, M. Riaz, M.F.M. Sabri, S.M. Said, R. Saidur, Renew. Sustain. Energy Rev. 64 (2016) 635–659.
[305] X. Shi, L. Chen, C. Uher, Int. Mater. Rev. 61 (2016) 379–415.
[306] T. Tomida, A. Sumiyoshi, G. Nie, T. Ochi, S. Suzuki, M. Kikuchi, K. Mukaiyama, J.Q. Guo, J. Electron. Mater. 46 (2017) 2944–2949.
[307] W.-S. Liu, B.-P. Zhang, L.-D. Zhao, J.-F. Li, Chem. Mater. 20 (2008) 7526–7531.
[308] X. Zhang, Q.M. Lu, J.X. Zhang, Q. Wei, D.M. Liu, Y.Q. Liu, J. Alloys. Compd. 457 (2008) 368–371.
[309] H. Tashiro, Y. Notohara, T. Sakakibara, H. Anno, K. Matsubara, XVI ICT' 97. Proc. ICT'97. 16th Int. Conf. Thermoelectr. (Cat. No.97TH8291), IEEE, (1997), pp. 326–329.
[310] B. Duan, P. Zhai, L. Liu, Q. Zhang, X. Ruan, J. Mater. Sci.: Mater. Electron. 23 (2012) 1817–1822.
[311] X. Su, H. Li, G. Wang, H. Chi, X. Zhou, X. Tang, Q. Zhang, C. Uher, Chem. Mater. 23 (2011) 2948–2955.
[312] A.U. Khan, K. Kobayashi, D.-M. Tang, Y. Yamauchi, K. Hasegawa, M. Mitome, Y. Xue, B. Jiang, K. Tsuchiya, D. Golberg, Y. Bando, T. Mori, Nano Energy 31 (2017) 152–159.
[313] C. Xu, B. Duan, S. Ding, P. Zhai, Q. Zhang, J. Electron. Mater. 43 (2014) 2224–2228.
[314] J.S. Dyck, W. Chen, C. Uher, L. Chen, X. Tang, T. Hirai, J. Appl. Phys. 91 (2002) 3698–3705.
[315] M. Puyet, A. Dauscher, B. Lenoir, C. Bellouard, C. Stiewe, E. Müller, J. Hejtmanek, J. Tobola, Phys. Rev. B 75 (2007) 245110.
[316] J. Yang, W. Zhang, S.Q. Bai, Z. Mei, L.D. Chen, Appl. Phys. Lett. 90 (2007) 192111.
[317] Q.M. Lu, J.X. Zhang, X. Zhang, Y.Q. Liu, D.M. Liu, M.L. Zhou, J. Appl. Phys. 98 (2005) 106107.
[318] X. Shi, H. Kong, C.-P. Li, C. Uher, J. Yang, J.R. Salvador, H. Wang, L. Chen, W. Zhang, Appl. Phys. Lett. 92 (2008) 182101.
[319] W. Zhao, P. Wei, Q. Zhang, C. Dong, L. Liu, X. Tang, J. Am. Chem. Soc. 131 (2009) 3713–3720.
[320] S.Q. Bai, Y.Z. Pei, L.D. Chen, W.Q. Zhang, X.Y. Zhao, J. Yang, Acta Mater. 57 (2009) 3135–3139.
[321] X. Shi, J.J. Yang, J.R. Salvador, M. Chi, J.Y. Cho, H. Wang, S. Bai, J.J. Yang, W. Zhang, L. Chen, J. Am. Chem. Soc. 133 (2011) 7837–7846.
[322] D.T. Morelli, G.P. Meisner, J. Appl. Phys. 77 (1995) 3777–3781.
[323] X. Shi, S. Bai, L. Xi, J. Yang, W. Zhang, L. Chen, J. Yang, J. Mater. Res. (Focus Issue: Adv. Thermoelectric Mater.) 26 (2011) 1745–1754.
[324] D.-K. Shin, I.-H. Kim, J. Korean Phys. Soc. 69 (2016) 798–805.
[325] P.F. Qiu, J. Yang, R.H. Liu, X. Shi, X.Y. Huang, G.J. Snyder, W. Zhang, L.D. Chen, J. Appl. Phys. 109 (2011) 063713.
[326] J. Prado-Gonjal, P. Vaqueiro, C. Nuttall, R. Potter, A.V. Powell, J. Alloys. Compd. 695 (2017) 3598–3604.
[327] C. Sekine, Y. Mori, J. Appl. Phys. 56 (2017) 05FA09.
[328] Y. Liu, X. Li, Q. Zhang, C. Chen, J. Li, L. Zhang, D. Yu, Y. Tian, B. Xu, J. Mater. Sci. Mater. Electron. 27 (2016) 6433–6437.
[329] Y. Liu, X. Li, Q. Zhang, L. Zhang, D. Yu, B. Xu, Y. Tian, Materials (Basel) 9 (2016) 257.
[330] Y. Li, P. Qiu, H. Duan, J. Chen, G.J. Snyder, X. Shi, B.B. Iversen, L. Chen, J. Mater. Chem. C 4 (2016) 4374–4379.
[331] X. Li, Q. Zhang, Y. Kang, C. Chen, L. Zhang, D. Yu, Y. Tian, B. Xu, J. Alloys. Compd. 677 (2016) 61–65.
[332] H. Fukuoka, S. Yamanaka, Chem. Mater. 22 (2010) 47–51.
[333] H. Takizawa, K. Miura, M. Ito, T. Suzuki, T. Endo, J. Alloys. Compd. 282 (1999) 79–83.
[334] G.S. Nolas, H. Takizawa, T. Endo, H. Sellinschegg, D.C. Johnson, Appl. Phys. Lett. 77 (2000) 52–54.
[335] F. Serrano-Sánchez, J. Prado-Gonjal, N.M. Nemes, N. Biskup, M. Varela, O.J. Dura, J.L. Martínez, M.T. Fernández-Díaz, F. Fauth, J.A. Alonso, J. Mater. Chem. A 6 (2018) 118–126.
[336] L.B. Wang, J. Ni, X.P. Jia, J.M. Qin, X. Guo, L. Deng, J. Alloys. Compd. 691 (2017) 452–456.
[337] L. Fu, J. Yang, J. Peng, Q. Jiang, Y. Xiao, Y. Luo, D. Zhang, Z. Zhou, M. Zhang, Y. Cheng, F. Cheng, J. Mater. Chem. A 3 (2015) 1010–1016.
[338] H. Li, X. Tang, Q. Zhang, C. Uher, Appl. Phys. Lett. 94 (2009) 102114.
[339] Z. Xiong, X. Chen, X. Huang, S. Bai, L. Chen, Acta Mater. 58 (2010) 3995–4002.
[340] L. Zhang, F. Duan, X. Li, X. Yan, W. Hu, L. Wang, Z. Liu, Y. Tian, B. Xu, J. Appl. Phys. 114 (2013) 083715.
[341] T. Liang, X. Su, Y. Yan, G. Zheng, X. She, Y. You, C. Uher, M.G. Kanatzidis, X. Tang, NPG Asia Mater. 9 (2017) e352.
[342] A. Moure, M. Rull-Bravo, B. Abad, A. Del Campo, M.M. Rojo, M.H. Aguirre, A. Jacquot, J.F. Fernandez, M. Martin-Gonzalez, Nano Energy 31 (2017) 393–402.
[343] Q. Zhang, Z. Zhou, M. Dylla, M.T. Agne, Y. Pei, L. Wang, Y. Tang, J. Liao, J. Li, S. Bai, W. Jiang, L. Chen, G. Jeffrey Snyder, Nano Energy 41 (2017) 501–510.
[344] P. Zong, R. Hanus, M. Dylla, Y. Tang, J. Liao, Q. Zhang, G.J. Snyder, L. Chen, Energy Environ. Sci. 10 (2017) 183–191.
[345] X. Tang, Q. Zhang, L. Chen, T. Goto, T. Hirai, J. Appl. Phys. 97 (2005) 093712.
[346] Q. Jie, H. Wang, W. Liu, H. Wang, G. Chen, Z. Ren, Phys. Chem. Chem. Phys. 15 (2013) 6809.
[347] V.V. Khovaylo, T.A. Korolkov, A.I. Voronin, M.V. Gorshenkov, A.T. Burkov, J. Mater. Chem. A 5 (2017) 3541–3546.
[348] S. Wang, J.R. Salvador, J. Yang, P. Wei, B. Duan, J. Yang, NPG Asia Mater. 8 (2016) e285–e285.
[349] T.C. Holgate, Y. Song, D. Shi, R. Utz, T. Chung, R. Bennett, S. Keyser, T.E. Hammel, R. Sievers, T. Caillat, J.-P. Fleurial, Reston, Virginia14th Int. Energy Convers. Eng. Conf., American Institute of Aeronautics and Astronautics2016, 14th Int. Energy Convers. Eng. Conf., American Institute of Aeronautics and Astronautics (2016).
[350] K.L. Smith, B.C. Li, S. Firdosy, S. Sujittosakul, M. Errico, G. Nakatsukasa, J.-P. Fleurial, R. Ewell, Reston, Virginia14th Int. Energy Convers. Eng. Conf., American Institute of Aeronautics and Astronautics2016, 14th Int. Energy Convers. Eng. Conf., American Institute of Aeronautics and Astronautics (2016).
[351] Y. Sun, G. Chen, G. Bai, X. Yang, P. Li, P. Zhai, J. Electron. Mater. 46 (2017) 2832–2838.
[352] Y.-S. Park, T. Thompson, Y. Kim, J.R. Salvador, J.S. Sakamoto, J. Mater. Sci. 50 (2015) 1500–1512.
[353] S.M. Kauzlarich, S.R. Brown, G.J. Snyder, Dalton Trans. 21 (2007) 2099–2107.
[354] S. Kauzlarich, A. Zevalkink, E.S. Toberer, G.J. Snyder, I. Nandhakumar, N.M. White, S. Beeby (Eds.), Thermoelectr. Mater. Devices, Royal Soc. Chem. 2016.
[355] H. Schaefer, Ann. Rev. Mater. Sci. 15 (1985) 1–41.
[356] J.Y. Chan, M.M. Olmstead, S.M. Kauzlarich, Chem. Mater. 10 (1998) 3583–3588.
[357] O.Y. Zelinska, A.V. Tkachuk, A.P. Grosvenor, A. Mar, Chem. Met. Alloy. 1 (2008) 204–209.
[358] G. Cordier, H. Schaefer, M. Stelter, Z. Naturforsch. 39b (1984) 727–732.
[359] S.-J. Kim, M.G. Kanatzidis, Inorg. Chem. 40 (2001) 3781–3785.
[360] A.V. Shevelkov, K. Kovnir, T.F. Fässler (Ed.), Zintl Phases Princ. Recent Dev. Springer Berlin Heidelberg, Berlin, Heidelberg, 2011, pp. 97–142.
[361] D. Bende, Y. Grin, F.R. Wagner, Chemistry (Easton) 20 (2014) 9702–9708.
[362] W.G. Zeier, J. Schmitt, G. Hautier, U. Aydemir, Z.M. Gibbs, C. Felser, G.J. Snyder, Nat. Rev. Mater. 1 (2016) 1–10.
[363] E.S. Toberer, C.A. Catherine, S.R. Brown, T. Ikeda, A.F. May, S.M. Kauzlarich, G.J. Snyder, Adv. Funct. Mater. 18 (2008) 2795–2800.
[364] S. Xia, S. Bobev, J. Am. Chem. Soc. 129 (2007) 10011–10018.
[365] A. Zevalkink, W.G. Zeier, E. Cheng, G.J. Snyder, J.-P. Fleurial, S. Bux, Chem. Mater. 26 (2014) 5710–5717.
[366] W. Peng, S. Chanakian, A. Zevalkink, Inorg. Chem. Front. 5 (2018) 1744–1759.
[367] A. Zevalkink, D.M. Smiadak, J.L. Blackburn, A.J. Ferguson, M.L. Chabinyc, O. Delaire, J. Wang, K. Kovnir, J. Martin, L.T. Schelhas, T.D. Sparks, S.D. Kang, M.T. Dylla, G.J. Snyder, B. Ortiz, E. Toberer, Appl. Phys. Rev. 5 (2018) 021303.
[368] P.C. Canfield, Z. Fisk, Philos. Mag. 6 (1992) 1117–1123.
[369] M.G. Kanatzidis, R.P. ttgen, W. Jeitschko, Angew. Chem. Int. Ed. Engl. 44 (2005) 6996–7023.
[370] R.A. Ribeiro, M.A. Avila, Philos. Mag. 92 (2012) 2492–2507.
[371] S.R. Brown, S. Kauzlarich, F. Gascoin, G.J. Snyder, Chem. Mater. 18 (2006) 1873–1877.
[372] A.F. May, M.A. McGuire, J. Ma, O. Delaire, A. Huq, R. Custelcean, J. Appl. Phys. 111 (2012) 33708.
[373] A.F. May, M.A. McGuire, D.J. Singh, R. Custelcean, G.E. Jellison Jr, Inorg. Chem. 50 (2011) 11127–11133.
[374] J.-A. Paik, E. Brandon, T. Caillat, R. Ewell, J.-P. Fleurial, Proc. Nucl. Emerg. Tech. Sp. (2011).
[375] E.S. Toberer, A. Zevalkink, N. Crisosto, G.J. Snyder, Adv. Funct. Mater. 20 (2010) 4375–4380.
[376] A. Zevalkink, E.S. Toberer, W.G. Zeier, E. Flage- Larsen, G.J. Snyder, Energy Environ. Sci. 4 (2011) 510–518.
[377] A. Zevalkink, W.G. Zeier, G. Pomrehn, E. Schechtel, W. Tremel, G.J. Snyder, Energy Environ. Sci. 5 (2012) 9121.

[378] F. Gascoin, S. Ottensmann, D. Stark, S.M. Haile, G.J. Snyder, Adv. Funct. Mater. 15 (2005) 1860–1864.
[379] C.A. Cox, S.R. Brown, G.J. Snyder, S.M. Kauzlarich, J. Electron. Mater. 39 (2010) 1373–1375.
[380] C. Yu, Y. Chen, H. Xie, G.J. Snyder, C. Fu, J. Xu, X. Zhao, T. Zhu, Appl. Phys. Express 5 (2012) 31801.
[381] C.A. Uvarov, F. Ortega-Alvarez, S.M. Kauzlarich, Inorg. Chem. 51 (2012) 7617–7624.
[382] H. Zhang, J.T. Zhao, Y. Grin, X.J. Wang, M.B. Tang, Z.Y. Man, H.H. Chen, X.X. Yang, J. Chem. Phys. 129 (2008) 164713.
[383] X.-J. Wang, M.-B. Tang, H.-H. Chen, X.-X. Yang, J.-T. Zhao, U. Burkhardt, Y. Grin, Appl. Phys. Lett. 94 (2009) 92106.
[384] H. Zhang, L. Fang, M.-B. Tang, H.-H. Chen, X.-X. Yang, X. Guo, J.-T. Zhao, Y. Grin, Intermetallics 18 (2010) 193–198.
[385] H. Zhang, M. Baitinger, M.B. Tang, Z.Y. Man, H.H. Chen, X.X. Yang, Y. Liu, L. Chen, Y. Grin, J.T. Zhao, Dalton Trans. 39 (2010) 1101–1104.
[386] A. Zevalkink, U. Aydemir, G.J. Snyder, C. Uher (Ed.), CRC Handb. Thermoelectr. 2016.
[387] S. Bux, A. Zevalkink, O. Janka, D. Uhl, S. Kauzlarich, G.J. Snyder, J.P. Fleurial, J. Mater. Chem. A 2 (2013) 215–220.
[388] S. Ohno, U. Aydemir, M. Amsler, J.-H. Pöhls, S. Chanakian, A. Zevalkink, M.A. White, S.K. Bux, C. Wolverton, G.J. Snyder, Adv. Funct. Mater. 27 (2017) 1606361.
[389] J. Shuai, H. Geng, Y. Lan, Z. Zhu, C. Wang, Z. Liu, J. Bao, C.W. Chu, J. Sui, Z. Ren, Proc. Natl. Acad. Sci. U. S. A. 113 (2016) E4125–32.
[390] A.F. May, E.S. Toberer, G.J. Snyder, J. Appl. Phys. 106 (2009) 13706.
[391] U. Aydemir, A. Zevalkink, A. Ormeci, S. Bux, G.J. Snyder, J. Mater. Chem. 4 (2016) 1867–1875.
[392] B.R. Ortiz, P. Gorai, V. Stevanović, E.S. Toberer, Chem. Mater. 29 (2017) 4523–4534.
[393] T. Yi, C.A. Cox, E.S. Toberer, G.J. Snyder, S.M. Kauzlarich, Chem. Mater. 22 (2010) 935–941.
[394] E.S. Toberer, A. Zevalkink, G.J. Snyder, J. Mater. Chem. 21 (2011) 15843.
[395] H. Tamaki, H.K. Sato, T. Kanno, Adv. Mater. 28 (2016) 10182–10187.
[396] W. Peng, G. Petretto, G.-M. Rignanese, G. Hautier, A. Zevalkink, Joule 2 (2018) 021303.
[397] J.J. Kuo, S.D. Kang, K. Imasato, H. Tamaki, S. Ohno, T. Kannoc, G.J. Snyder, Energy Environ. Sci. 11 (2018) 429–434.
[398] S. Ohno, K. Imasato, S. Anand, H. Tamaki, S.D. Kang, P. Gorai, H.K. Sato, E.S. Toberer, T. Kanno, G.J. Snyder, Joule 2 (2018) 1–14.
[399] A. Zevalkink, J. Swallow, G.J. Snyder, Dalton Trans. 42 (2013) 9713–9719.
[400] G.S. Pomrehn, A. Zevalkink, W.G. Zeier, A. van de Walle, G.J. Snyder, Angew. Chem. Int. Ed. Engl. 53 (2014) 3422–3426.
[401] Q.-G. Cao, H. Zhang, M.-B. Tang, H.-H. Chen, X.-X. Yang, Y. Grin, J.-T. Zhao, J. Appl. Phys. 107 (2010) 53714.
[402] H. Zhang, L. Fang, M.B. Tang, Z.Y. Man, H.H. Chen, X.X. Yang, M. Baitinger, Y. Grin, J.T. Zhao, J. Chem. Phys. 133 (2010) 194701.
[403] C. Yu, T.J. Zhu, S.N. Zhang, X.B. Zhao, J. He, Z. Su, T.M. Tritt, J. Appl. Phys. 104 (2008) 13705.
[404] J. Shuai, Y. Wang, Z. Liu, H.S. Kim, J. Mao, J. Sui, Z. Ren, Nano Energy 25 (2016) 136–144.
[405] W.G. Zeier, A. Zevalkink, E. Schechtel, W. Tremel, G.J. Snyder, J. Mater. Chem. 22 (2012) 9826.
[406] J. Zhang, L. Song, S.H. Pedersen, H. Yin, L.T. Hung, B.B. Iversen, Nat. Comm. 8 (2016) 13901.
[407] J. Shuai, J. Mao, S. Song, Q. Zhang, G. Chen, Z. Ren, Mater. Today Phys. 1 (2017) 74–95.
[408] S. Ohno, A. Zevalkink, Y. Takagiwa, S.K. Bux, G.J. Snyder, J. Mater. Chem. A 2 (2014) 7478.
[409] B.R. Ortiz, P. Gorai, L. Krishna, R. Mow, A. Lopez, R. McKinney, V. Stevanović, E.S. Toberer, J. Mater. Chem. A 5 (2017) 4036–4046.
[410] J. Yan, P. Gorai, B. Ortiz, S. Miller, S. Barnett, T. Mason, V. Stevanovic, E.S. Toberer, Energy Environ. Sci. 8 (2015) 983–994.
[411] L. jerg, G.K.H. Madsen, B.B. Iversen, Chem. Mater. 24 (2012) 2111–2116.
[412] in:, IUPAC Compend. Chem. Terminol., IUPAC, Research Triagle Park, NC, n.d.
[413] G.S. Nolas, G.A. Slack, S.B. Schujman, Semicond. Semimetals 69 (2001) 255–300.
[414] K.A. Kovnir, A.V. Shevelkov, Russ. Chem. Rev. 73 (2004) 923–938.
[415] M. Beekman, G.S. Nolas, J. Mater. Chem. 18 (2008) 842–851.
[416] M. Beekman, G.S. Nolas, G.S. Nolas (Ed.), The Physics and Chemistry of Inorganic Clathrates (Springer Series in Materials Science Vol. 199), Springer- Verlag, 2014.
[417] J.-A. Dolyniuk, B. Owens-Baird, J. Wang, J.V. Zaikina, K. Kovnir, Mater. Sci. Eng. R Rep. 108 (2016) 1–46.
[418] J.S. Kasper, P. Hagenmuller, M. Pouchard, C. Cros, Science 150 (1965) 1713–1714.
[419] K.W. Allen, J. Chem. Soc. (1959) 4131–4132.
[420] C. Cros, M. Pouchard, P. Hagenmuller, J. Solid State Chem. 2 (1970) 570–581.
[421] S. Stefanoski, M. Beekman, G.S. Nolas, Inorganic Clathrates for Thermoelectric Applications, Springer, Dordrecht, 2014, pp. 169–191.
[422] H. Kawaji, H. Horie, S. Yamanaka, M. Ishikawa, Phys. Rev. Lett. 74 (1995) 1427–1429.
[423] M. Beekman, D.T. Morelli, G.S. Nolas, Nat. Mater. 14 (2015) 1182–1185.
[424] D.G. Cahill, S.K. Watson, R.O. Pohl, Phys. Rev. B 46 (1992) 6131–6140.
[425] M. Beekman, D.G. Cahill, Cryst. Res. Technol. 52 (2017) 1700114.
[426] G.A. Slack, Mater. Res. Soc. Symp. Proc. 478 (1997).
[427] G.S. Nolas, J.L. Cohn, G.A. Slack, S.B. Schujman, Appl. Phys. Lett. 73 (1998) 178.
[428] J.L. Cohn, G.S. Nolas, V. Fessatidis, T.H. Metcalf, G.A. Slack, Phys. Rev. Lett. 82 (1999) 779–782.
[429] V.L. Kuznetsov, L.A. Kuznetsova, A.E. Kaliazin, D.M. Rowe, J. Appl. Phys. 87 (2000) 7871.
[430] M. Christensen, S. Johnsen, B.B. Iversen, Dalton Trans. 39 (2010) 978–992.
[431] T. Takabatake, K. Suekuni, T. Nakayama, E. Kaneshita, Rev. Mod. Phys. 86 (2014) 669–716.
[432] J. Dong, O.F. Sankey, C.W. Myles, Phys. Rev. Lett. 86 (2001) 2361–2364.
[433] M. Christensen, A.B. Abrahamsen, N.B. Christensen, F. Juranyi, N.H. Andersen, K. Lefmann, J. Andreasson, C.R.H. Bahl, B.B. Iversen, Nat. Mater. 7 (2008) 811–815.
[434] H. Euchner, S. Pailhès, L.T.K.K. Nguyen, W. Assmus, F. Ritter, A. Haghighirad, Y. Grin, S. Paschen, M. De Boissieu, Phys. Rev. B - Condens. Matter Mater. Phys. 86 (2012) 224303.
[435] P.-F. Lory, S. Pailhès, V.M. Giordano, H. Euchner, H.D. Nguyen, R. Ramlau, H. Borrmann, M. Schmidt, M. Baitinger, M. Ikeda, P. Tomeš, M. Mihalkovič, C. Allio, M.R. Johnson, H. Schober, Y. Sidis, F. Bourdarot, L.P. Regnault, J. Ollivier, S. Paschen, Y. Grin, M. de Boissieu, Nat. Commun. 8 (2017) 491.
[436] P. Norouzzadeh, C.W. Myles, D. Vashaee, Phys. Rev. B 95 (2017) 195206.
[437] H. Euchner, S. Pailhès, V.M. Giordano, M. de Boissieu, Phys. Rev. B 97 (2018) 014304.
[438] F. Bridges, L. Downward, Phys. Rev. B 70 (2004) 140201.
[439] S. Christensen, M.S. Schmøkel, K.A. Borup, G.K.H. Madsen, G.J. McIntyre, S.C. Capelli, M. Christensen, B.B. Iversen, J. Appl. Phys. 119 (2016) 185102.
[440] T. Tadano, Y. Gohda, S. Tsuneyuki, Phys. Rev. Lett. 114 (2015) 095501.
[441] G.K.H. Madsen, A. Katre, C. Bera, Phys. Status Solidi 213 (2016) 802–807.
[442] M. Beekman, A. VanderGraaff, J. Appl. Phys. 121 (2017) 205105.
[443] J.H. Roudebush, E.S. Toberer, H. Hope, G. Jeffrey Snyder, S.M. Kauzlarich, J. Solid State Chem. 184 (2011) 1176–1185.
[444] H. Anno, H. Yamada, T. Nakabayashi, M. Hokazono, R. Shirataki, J. Solid State Chem. 193 (2012) 94–104.
[445] X. Yan, E. Bauer, P. Rogl, S. Paschen, Phys. Rev. B 87 (2013) 115206.
[446] W.-Q. Cao, Y.-G. Yan, X.-F. Tang, S.-K. Deng, J. Phys. D Appl. Phys. 41 (2008) 215105.
[447] E.S. Toberer, M. Christensen, B.B. Iversen, G.J. Snyder, Phys. Rev. B 77 (2008) 075203.
[448] X. Shi, J. Yang, S. Bai, J. Yang, H. Wang, M. Chi, J.R. Salvador, W. Zhang, L. Chen, W. Wong- Ng, Adv. Funct. Mater. 20 (2010) 755–763.
[449] S. Deng, X. Tang, P. Yang, M. Li, J. Mater. Sci. 44 (2009) 939–944.
[450] H. Zhang, H. Borrmann, N. Oeschler, C. Candolfi, W. Schnelle, M. Schmidt, U. Burkhardt, M. Baitinger, J.-T. Zhao, Y. Grin, Inorg. Chem. 50 (2011) 1250–1257.
[451] S. Deng, X. Tang, P. Li, Q. Zhang, J. Appl. Phys. 103 (2008) 073503.
[452] S. Koda, K. Kishimoto, K. Akai, H. Asada, T. Koyanagi, J. Appl. Phys. 116 (2014) 023710.
[453] S. Deng, Y. Saiga, K. Suekuni, T. Takabatake, J. Appl. Phys. 108 (2010) 073705.
[454] Y. Saiga, B. Du, S.K. Deng, K. Kajisa, T. Takabatake, J. Alloys. Compd. 537 (2012) 303–307.
[455] Y. Saiga, K. Suekuni, S.K. Deng, T. Yamamoto, Y. Kono, N. Ohya, T. Takabatake, J. Alloys. Compd. 507 (2010) 1–5.
[456] M.W. Gaultois, T.D. Sparks, C.K.H. Borg, R. Seshadri, W.D. Bonificio, D.R. Clarke, Chem. Mater. 25 (2013) 2911–2920.
[457] S. Kauzlarich, F. Sui, C. Perez, Materials (Basel) 9 (2016) 714.
[458] F. Sui, H. He, S. Bobev, J. Zhao, F.E. Osterloh, S.M. Kauzlarich, Chem. Mater. 27 (2015) 2812–2820.
[459] Y. Dong, P. Chai, M. Beekman, X. Zeng, T.M. Tritt, G.S. Nolas, Inorg. Chem. 54 (2015) 5316–5321.
[460] S. Munetoh, M. Arita, H. Makiyama, T. Motooka, MRS Proc. 1102 (2008) 1102-LL04-30.
[461] F. Sui, S.M. Kauzlarich, Chem. Mater. 28 (2016) 3099–3107.
[462] A. Prokofiev, A. Sidorenko, K. Hradil, M. Ikeda, R. Svagera, M. Waas, H. Winkler, K. Neumaier, S. Paschen, Nat. Mater. 12 (2013) 1096–1101.
[463] P. Norouzzadeh, C.W. Myles, D. Vashaee, Sci. Rep. 4 (2015) 7028.
[464] F. Heusler, Verhandlungen Der DPG 5 (1903) 219.
[465] C. Felser, G.H. Fecher, B. Balke, Angew. Chemie Int. Ed. 46 (2007) 668–699.
[466] T. Graf, C. Felser, S.S.P. Parkin, Prog. Solid State Chem. 39 (2011) 1–50.
[467] F. Casper, T. Graf, S. Chadov, B. Balke, C. Felser, Semicond. Sci. Technol. 27 (2012).
[468] S. Öğüt, K.M. Rabe, Phys. Rev. B 51 (1995) 10443–10453.
[469] H.C. Kandpal, C. Felser, R. Seshadri, J. Phys. D-Applied Phys. 39 (2006) 776–785.
[470] W. Wunderlich, Y. Motoyama, MRS Online Proc. Libr. 1128 (2008).
[471] R. Asahi, T. Morikawa, H. Hazama, M. Matsubara, J. Physics-Condensed Matter 20 (2008).
[472] K. Bartholomé, B. Balke, D. Zuckermann, M. Köhne, M. Müller, K. Tarantik, J. König, J. Electron. Mater. 43 (2014) 1775.
[473] J.P.A. Makongo, D.K. Misra, X. Zhou, A. Pant, M.R. Shabetai, X. Su, C. Uher, K.L. Stokes, P.F.P. Poudeu, J. Am. Chem. Soc. 133 (2011) 18843–18852.
[474] C.U.I. Yu, T. Zhu, K.A.I. Xiao, J. Shen, X. Zhao, Funct. Mater. Lett. 03 (2010) 227–231.
[475] X. Yan, G. Joshi, W. Liu, Y. Lan, H. Wang, S. Lee, J.W. Simonson, S.J. Poon, T.M. Tritt, G. Chen, Z.F. Ren, Nano Lett. 11 (2011) 556–560.
[476] J.E. Garay, Annu. Rev. Mater. Res. 40 (2010) 445–468.
[477] M.A. Verges, P.J. Schilling, P. Upadhyay, W.K. Miller, R. Yaqub, K.L. Stokes, P.F.P. Poudeu, Sci. Adv. Mater. 3 (2011) 659–666.
[478] S. Chen, Z.L.B.-Cr. Ren, Mater. Today 16 (2013) 387–395.
[479] C.S. Birkel, W.G. Zeier, J.E. Douglas, B.R. Lettiere, C.E. Mills, G. Seward, A. Birkel, M.L. Snedaker, Y. Zhang, G.J. Snyder, T.M. Pollock, R. Seshadri, G.D. Stucky,

Chem. Mater. 24 (2012) 2558–2565.
[480] C. Uher, J. Yang, S. Hu, D.T. Morelli, G.P. Meisner, Phys. Rev. B 59 (1999) 8615–8621.
[481] Y. Kimura, H. Ueno, Y. Mishima, J. Electron. Mater. 38 (2009) 934–939.
[482] W. Xie, Q. Jin, X. Tang, J. Appl. Phys. 103 (2008) 43711.
[483] M. Zhou, L. Chen, C. Feng, D. Wang, J.-F. Li, J. Appl. Phys. 101 (2007) 113714.
[484] M. Schwall, B. Balke, Appl. Phys. Lett. 98 (2011) 42106.
[485] F.G. Aliev, N.B. Brandt, V.V. Moshchalkov, V.V. Kozyrkov, R.V. Skolozdra, A.I. Belogorokhov, Zeitschrift Für Phys. B Condens. Matter 75 (1989) 167–171.
[486] F.G. Aliev, V.V. Kozyrkov, V.V. Moshchalkov, R.V. Scolozdra, K. Durczewski, Zeitschrift Für Phys. B Condens. Matter 80 (1990) 353–357.
[487] H. Hohl, A.P. Ramirez, W. Kaefer, K. Fess, C. Thurner, C. Kloc, E.C. Bucher, MRS Proc. 478 (1997) 109.
[488] H. Hohl, A.P. Ramirez, C. Goldmann, G. Ernst, B. Wolfing, E. Bucher, J. Phys.-Condens. Matter 11 (1999) 1697–1709.
[489] Q. Shen, L.M. Zhang, L.D. Chen, T. Goto, T. Hirai, J. Mater. Sci. Lett. 20 (2001) 2197–2199.
[490] Q. Shen, L. Chen, T. Goto, T. Hirai, J. Yang, G.P. Meisner, C. Uher, Appl. Phys. Lett. 79 (2001) 4165–4167.
[491] S.R. Culp, S.J. Poon, N. Hickman, T.M. Tritt, J. Blumm, Appl. Phys. Lett. 88 (2006) 42106.
[492] Y. Kimura, T. Kuji, A. Zama, Y. Shibata, Y. Mishima, MRS Online Proc. Libr. 886 (2005).
[493] S. Sakurada, N. Shutoh, Appl. Phys. Lett. 86 (2005) 2105.
[494] M. Schwall, B. Balke, Phys. Chem. Chem. Phys. 15 (2013) 1868–1872.
[495] G. Joshi, T. Dahal, S. Chen, H.Z. Wang, J. Shiomi, G. Chen, Z.F. Ren, Nano Energy 2 (2013) 82–87.
[496] P.H. Ngan, D.V. Christensen, G.J. Snyder, L.T. Hung, S. Linderoth, N. Van Nong, N. Pryds, Phys. Status Solidi 211 (2014) 9–17.
[497] Z.-H. Wu, H.-Q. Xie, Y.-B. Zhai, Appl. Phys. Lett. 103 (2013) 243901.
[498] T. Sekimoto, K. Kurosaki, H. Muta, S. Yamanaka, Jpn J. Appl. Phys. Part 2-Lett. Express Lett. 46 (2007) L673–L675.
[499] Y. Gelbstein, B. Dado, O. Ben-Yehuda, Y. Sadia, Z. Dashevsky, M.P. Dariel, Chem. Mater. 22 (2010) 1054–1058.
[500] W. Liu, X. Yan, G. Chen, Z. Ren, Nano Energy 1 (2012) 42–56.
[501] S.J. Poon, D. Wu, S. Zhu, W. Xie, T.M. Tritt, P. Thomas, R. Venkatasubramanian, J. Mater. Res. 26 (2011) 2795–2802.
[502] X. Yan, W. Liu, H. Wang, S. Chen, J. Shiomi, K. Esfarjani, H. Wang, D. Wang, G. Chen, Z.L.B.-Y. Ren, Energy Environ. Sci. 5 (2012) 7543–7548.
[503] E. Rausch, B. Balke, S. Ouardi, C. Felser, Phys. Chem. Chem. Phys. 16 (2014) 25258–25262.
[504] E. Rausch, B. Balke, J.M. Stahlhofen, S. Ouardi, U. Burkhardt, C. Felser, J. Mater. Chem. C 3 (2015) 10409–10414.
[505] G. Rogl, P. Sauerschnig, Z. Rykavets, V.V. Romaka, P. Heinrich, B. Hinterleitner, A. Grytsiv, E. Bauer, P. Rogl, Acta Mater. 131 (2017) 336–348.
[506] E. Rausch, B. Balke, S. Ouardi, C. Felser, Energy Technol. 3 (2015) 1217–1224.
[507] D.P. Young, P. Khalifah, R.J. Cava, A.P. Ramirez, J. Appl. Phys. 87 (2000) 317–321.
[508] L. Jodin, J. Tobola, P. Pecheur, H. Scherrer, S. Kaprzyk, Phys. Rev. B 70 (2004) 184207.
[509] J. Yang, H. Li, T. Wu, W. Zhang, L. Chen, J. Yang, Adv. Funct. Mater. 18 (2008) 2880–2888.
[510] C.G. Fu, H.H. Xie, Y.T. Liu, T.J. Zhu, J. Xie, X.B. Zhao, Intermetallics 32 (2013) 39.
[511] C.G. Fu, H.H. Xie, T.J. Zhu, J. Xie, X.B. Zhao, J. Appl. Phys. 112 (2012) 124915.
[512] M.M. Zou, J.F. Li, J. Phys. D Appl. Phys. 43 (2010) 415403.
[513] C.G. Fu, T.J. Zhu, H.H. Xie, X.B. Zhao, Eur. Lett. 104 (2013) 46003.
[514] C.G. Fu, Y.T. Liu, H.H. Xie, X.H. Liu, X.B. Zhao, G.J. Snyder, J. Xie, T.J. Zhu, J. Appl. Phys. 114 (2013) 134905.
[515] C. Fu, T. Zhu, Y. Pei, H. Xie, H. Wang, G.J. Snyder, Y. Liu, Y. Liu, X. Zhao, Adv. Energy Mater. 4 (2014) 1400600.
[516] C. Fu, T. Zhu, Y. Liu, H. Xie, X. Zhao, Energy Environ. Sci. 8 (2015) 216–220.
[517] C.G. Fu, S.Q. Bai, Y.T. Liu, Y.S. Tang, L.D. Chen, X.B. Zhao, T.J. Zhu, Nat. Commun. 6 (2015) 8144.
[518] C.G. Fu, H.J. Wu, Y.T. Liu, J.Q. He, X.B. Zhao, T.J. Zhu, Adv. Sci. 3 (2016) 1600035.
[519] J. Yu, C. Fu, Y. Liu, K. Xia, U. Aydemir, T.C. Chasapis, G.J. Snyder, X. Zhao, T. Zhu, Adv. Energy Mater. 8 (2018) 1701313.
[520] T. Graf, G.H. Fecher, J. Barth, J. Winterlik, C. Felser, J. Phys. D-Appl. Phys. 42 (2009).
[521] J. Barth, G.H. Fecher, B. Balke, S. Ouardi, T. Graf, C. Felser, A. Shkabko, A. Weidenkaff, P. Klaer, H.J. Elmers, H. Yoshikawa, S. Ueda, K. Kobayashi, Phys. Rev. B 81 (2010).
[522] T. Graf, J. Barth, B. Balke, S. Populoh, A. Weidenkaff, C. Felser, Scr. Mater. 63 (2011) 925–928.
[523] B. Balke, S. Ouardi, T. Graf, J. Barth, C.G.F. Blum, G.H. Fecher, A. Shkabko, A. Weidenkaff, C. Felser, Solid State Commun. 150 (2010) 529–532.
[524] M. Schwall, L.M. Schoop, S. Ouardi, B. Balke, C. Felser, P. Klaer, H.-J. Elmers, Adv. Funct. Mater. 22 (2012) 1822–1826.
[525] Y. Nishino, Y. Tamada, J. Appl. Phys. 115 (2014) 123707.
[526] Y. Nishino, J. Jpn. Inst. Met. Mater. 79 (2015) 548.
[527] Y. Nishino, Mater. Sci. Forum 449–452 (2004) 909–912.
[528] I. Terasaki, Y. Sasago, K. Uchinokura, Phys. Rev. B 56 (1997) R12685–R12687.
[529] Y. Wang, N.S. Rogado, R.J. Cava, N.P. Ong, Nature 423 (2003) 425–428.
[530] Q. Huang, M.L. Foo, R.A. Pascal, J.W. Lynn, B.H. Toby, T. He, H.W. Zandbergen, R.J. Cava, Phys. Rev. B 70 (2004) 184110.
[531] M. Lee, L. Viciu, L. Li, Y. Wang, M.L. Foo, S. Watauchi, R. a Pascal, R.J. Cava, N.P. Ong, Nat. Mater. 5 (2006) 537–540.
[532] J.-Y. Kim, J.-I. Kim, S.-M. Choi, Y. Soo Lim, W.-S. Seo, H. Jin Hwang, J. Appl. Phys. 112 (2012) 113705.
[533] P. Ruleova, C. Drasar, P. Lostak, C.-P. Li, S. Ballikaya, C. Uher, Mater. Chem. Phys. 119 (2010) 299–302.
[534] J.-L. Lan, Y.-C. Liu, B. Zhan, Y.-H. Lin, B. Zhang, X. Yuan, W. Zhang, W. Xu, C.-W. Nan, Adv. Mater. 25 (2013) 5086–5090.
[535] J. Sui, J. Li, J. He, Y.-L. Pei, D. Berardan, H. Wu, N. Dragoe, W. Cai, L.-D. Zhao, Ener. Environ. Sci. 6 (2013) 2916–2920.
[536] Y.L. Pei, H. Wu, D. Wu, F. Zheng, J. He, J. Am. Chem. Soc. 136 (2014) 13902–13908.
[537] G. Kieslich, G. Cerretti, I. Veremchuk, R.P. Hermann, M. Panthöfer, J. Grin, W. Tremel, Phys. Status Solidi 213 (2016) 808–823.
[538] W. Koshibae, K. Tsutsui, S. Maekawa, Phys. Rev. B - Condens. Matter Mater. Phys. 62 (2000) 6869–6872.
[539] M. Karppinen, H. Fjellvåg, T. Konno, Y. Morita, T. Motohashi, H. Yamauchi, Chem. Mater. 16 (2004) 2790–2793.
[540] R. Tian, T. Zhang, D. Chu, R. Donelson, L. Tao, S. Li, J. Alloys. Compd. 615 (2014) 311–315.
[541] R. Tian, R. Donelson, C.D. Ling, P.E.R. Blanchard, T. Zhang, D. Chu, T.T. Tan, S. Li, J. Phys. Chem. C 117 (2013) 13382–13387.
[542] S. Saini, H.S. Yaddanapudi, K. Tian, Y. Yin, D. Magginetti, A. Tiwari, Sci. Rep. 7 (2017) 44621.
[543] H. Fonzes-Diacon, Compt. Rend. 130 (1990) 1025–1026.
[544] Y. Takano, C. Ogawa, Y. Miyahara, H. Ozaki, K. Sekizawa, J. Alloys. Compd. 249 (1997) 221–223.
[545] A.M. Kusainova, P.S. Berdonosov, L.G. Akselrud, L.N. Kholodkovskaya, V.A. Dolgikh, B.A. Popovkin, J. Solid State Chem. 112 (1994) 189–191.
[546] L.D. Zhao, D. Berardan, Y.L. Pei, C. Byl, L. Pinsard-Gaudart, N. Dragoe, Appl. Phys. Lett. 97 (2010) 092118.
[547] L. Pinsard-Gaudart, D. Bérardan, J. Bobroff, N. Dragoe, Phys. Status Solidi - Rapid Res. Lett. 2 (2008) 185–187.
[548] S.N. Ruddlesden, P. Popper, Acta Crystallogr. 11 (1958) 54–55.
[549] T. Okuda, K. Nakanishi, S. Miyasaka, Y. Tokura, Phys. Rev. B 63 (2001) 113104.
[550] K. Koumoto, Y. Wang, R. Zhang, A. Kosuga, R. Funahashi, Annu. Rev. Mater. Res. 40 (2010) 363–394.
[551] H. Ohta, S. Kim, Y. Mune, T. Mizoguchi, K. Nomura, S. Ohta, T. Nomura, Y. Nakanishi, Y. Ikuhara, M. Hirano, H. Hosono, K. Koumoto, Nat. Mater. 6 (2007) 129–134.
[552] S. Andersson, B. Collén, U. Kuylenstierna, A. Magnéli, Acta Chem. Scand. 11 (1957) 1641–1652.
[553] E. Canadell, M.-H. Whangbo, Chem. Rev. 91 (1991) 965–1034.
[554] G. Kieslich, W. Tremel, AIMS Mater. Sci. 1 (2014) 184–190.
[555] G. Cerretti, B. Balke, G. Kieslich, W. Tremel, Mater. Today Proc. 5 (2018) 10240–10248.
[556] M. Joos, G. Cerretti, I. Veremchuk, P. Hofmann, H. Frerichs, D.H. Anjum, T. Reich, I. Lieberwirth, M. Panthöfer, W.G. Zeier, W. Tremel, Inorg. Chem. 57 (2018) 1259–1268.
[557] F. Krumeich, A. Hussain, C. Bartsch, R. Gruehn, Anorg. Allg. Chem. 621 (1995) 799–806.
[558] S. Lee, R.H.T. Wilke, S. Trolier- McKinstry, S. Zhang, C.A. Randall, Appl. Phys. Lett. 96 (2010) 031910.
[559] G. Cerretti, M. Schrade, X. Song, B. Balke, H. Lu, T. Weidner, I. Lieberwirth, M. Panthöfer, T. Norby, W. Tremel, J. Mater. Chem. A 5 (2017) 9768–9774.
[560] C.P. Heinrich, M. Schrade, G. Cerretti, I. Lieberwirth, P. Leidich, A. Schmitz, H. Fjeld, E. Mueller, T.G. Finstad, T. Norby, W. Tremel, Mater. Horiz. 2 (2015) 519–527.
[561] P. Jood, R.J. Mehta, Y. Zhang, G. Peleckis, X. Wang, R.W. Siegel, T. Borca-Tasciuc, S.X. Dou, G. Ramanath, Nano Lett. 11 (2011) 4337–4342.
[562] Y. Kinemuchi, M. Mikami, K. Kobayashi, K. Watari, Y. Hotta, J. Electron. Mater. 39 (2010) 2059–2063.
[563] M. Ohtaki, K. Araki, K. Yamamoto, J. Electron. Mater. 38 (2009) 1234–1238.
[564] H. Shirakawa, E.J. Louis, A.G. MacDiarmid, C.K. Chiang, A.J. Heeger, J. Chem. Soc. Chem. Commun. 0 (1977) 578.
[565] J.J. Bozell, G.R. Petersen, Green Chem. 12 (2010) 539.
[566] R.-J. van Putten, J.C. van der Waal, E. de Jong, C.B. Rasrendra, H.J. Heeres, J.G. de Vries, Chem. Rev. 113 (2013) 1499–1597.
[567] O. Bubnova, X. Crispin, Energy Environ. Sci. 5 (2012) 9345.
[568] R. Kroon, D.A. Mengistie, D. Kiefer, J. Hynynen, J.D. Ryan, L. Yu, C. Müller, Chem. Soc. Rev. 45 (2016) 6147–6164.
[569] I.E. Jacobs, A.J. Moulé, Adv. Mater. 29 (2017) 1703063.
[570] O. Bubnova, Z.U. Khan, A. Malti, S. Braun, M. Fahlman, M. Berggren, X. Crispin, Nat. Mater. 10 (2011) 429–433.
[571] D. Moses, A. Denenstein, Phys. Rev. B 30 (1984) 2090–2097.
[572] C. Li, H. Ma, Z. Tian, Appl. Therm. Eng. 111 (2017) 1441–1447.
[573] J. Liu, X. Wang, D. Li, N.E. Coates, R.A. Segalman, D.G. Cahill, Macromolecules 48 (2015) 585–591.
[574] X. Hu, G. Chen, X. Wang, H. Wang, J. Mater. Chem. A 3 (2015) 20896–20902.
[575] O. Bubnova, Z.U. Khan, H. Wang, S. Braun, D.R. Evans, M. Fabretto, P. Hojati-Talemi, D. Dagnelund, J.B. Arlin, Y.H. Geerts, S. Desbief, D.W. Breiby, J.W. Andreasen, R. Lazzaroni, W.M. Chen, I. Zozoulenko, M. Fahlman, P.J. Murphy, M. Berggren, X. Crispin, Nat. Mater. 13 (2014) 190–194.
[576] F. Jiang, L. Wang, C. Li, X. Wang, Y. Hu, H. Liu, H. Yang, F. Zhao, J. Xu, J. Polym. Res. 24 (2017) 68.
[577] D. Beretta, A.J. Barker, I. Maqueira- Albo, A. Calloni, G. Bussetti, G. Dell'Erba, A. Luzio, L. Duò, A. Petrozza, G. Lanzani, M. Caironi, ACS Appl. Mater. Interfaces 9

(2017) 18151–18160.
[578] S.N. Patel, A.M. Glaudell, K.A. Peterson, E.M. Thomas, K.A. O'Hara, E. Lim, M.L. Chabinyc, Sci. Adv. 3 (2017) e1700434.
[579] A. Hamidi-Sakr, L. Biniek, J.-L. Bantignies, D. Maurin, L. Herrmann, N. Leclerc, P. Lévêque, V. Vijayakumar, N. Zimmermann, M. Brinkmann, Adv. Funct. Mater. 27 (2017) 1700173.
[580] J. Hynynen, D. Kiefer, C. Müller, RSC Adv. 8 (2018) 1593–1599.
[581] A.M. Glaudell, J.E. Cochran, S.N. Patel, M.L. Chabinyc, Adv. Energy Mater. 5 (2015) 1401072.
[582] S.N. Patel, M.L. Chabinyc, J. Appl. Polym. Sci. 134 (2017) 44403.
[583] J.D. Ryan, D.A. Mengistie, R. Gabrielsson, A. Lund, C. Müller, ACS Appl. Mater. Interfaces 9 (2017) 9045–9050.
[584] H. Fang, B.C. Popere, E.M. Thomas, C.-K. Mai, W.B. Chang, G.C. Bazan, M.L. Chabinyc, R.A. Segalman, J. Appl. Polym. Sci. 134 (2017) 44208.
[585] L.C. Isett, Phys. Rev. B 18 (1978) 439–447.
[586] K. Hayashi, T. Shinano, Y. Miyazaki, T. Kajitani, J. Appl. Phys. 109 (2011) 023712.
[587] M. Inoue, M.B. Inoue, C. Cruz- Vazquez, S. Roberts, Q. Fernando, Synth. Met. 19 (1987) 641–646.
[588] M. Oyama, Q. Wei, M. Mukaida, Y. Kawanishi, T. Ishida, Synth. Met. 230 (2017) 12–17.
[589] A.B. Kaiser, Phys. Rev. B 40 (1989) 2806–2813.
[590] Y. Xuan, X. Liu, S. Desbief, P. Leclère, M. Fahlman, R. Lazzaroni, M. Berggren, J. Cornil, D. Emin, X. Crispin, Phys. Rev. B 82 (2010) 115454.
[591] C.K. Mai, R.A. Schlitz, G.M. Su, D. Spitzer, X. Wang, S.L. Fronk, D.G. Cahill, M.L. Chabinyc, G.C. Bazan, J. Am. Chem. Soc. 136 (2014) 13478–13481.
[592] R.B. Aïch, N. Blouin, A. Bouchard, M. Leclerc, Chem. Mater. 21 (2009) 751–757.
[593] Q. Zhang, Y. Sun, W. Xu, D. Zhu, Macromolecules 47 (2014) 609–615.
[594] R. Kroon, D. Kiefer, D. Stegerer, L. Yu, M. Sommer, C. Müller, Adv. Mater. 29 (2017) 1700930.
[595] S.N. Patel, A.M. Glaudell, D. Kiefer, M.L. Chabinyc, ACS Macro Lett. 5 (2016) 268–272.
[596] M. Culebras, C.M. Gómez, A. Cantarero, J. Mater. Chem. A Mater. Energy Sustain. 2 (2014) 10109–10115.
[597] G.H. Kim, L. Shao, K. Zhang, K.P. Pipe, Nat. Mater. 12 (2013) 719–723.
[598] D.A. Mengistie, C.-H. Chen, K.M. Boopathi, F.W. Pranoto, L.-J. Li, C.-W. Chu, ACS Appl. Mater. Interfaces 7 (2015) 94–100.
[599] T. Menke, D. Ray, J. Meiss, K. Leo, M. Riede, Appl. Phys. Lett. 100 (2012) 093304.
[600] M. Sumino, K. Harada, M. Ikeda, S. Tanaka, K. Miyazaki, C. Adachi, Appl. Phys. Lett. 99 (2011) 093308.
[601] Z.H. Wang, K. Ichimura, M.S. Dresselhaus, G. Dresselhaus, W.-T. Lee, K.A. Wang, P.C. Eklund, Phys. Rev. B 48 (1993) 10657–10660.
[602] F. Gao, Y. Liu, Y. Xiong, P. Wu, B. Hu, L. Xu, Front. Optoelectron. China 10 (2017) 117–123.
[603] G. Zuo, Z. Li, E. Wang, M. Kemerink, Adv. Electron. Mater. 4 (2017) 1700501.
[604] J. Liu, L. Qiu, G. Portale, M. Koopmans, G. ten Brink, J.C. Hummelen, L.J.A. Koster, Adv. Mater. 29 (2017) 1701641.
[605] K.C. See, C. Landis, A. Sarjeant, H.E. Katz, Chem. Mater. 20 (2008) 3609–3616.
[606] H.E. Katz, A.J. Lovinger, J. Johnson, C. Kloc, T. Siegrist, W. Li, Y.-Y. Lin, A. Dodabalapur, Nature 404 (2000) 478–481.
[607] B. Russ, M.J. Robb, B.C. Popere, E.E. Perry, C.-K. Mai, S.L. Fronk, S.N. Patel, T.E. Mates, G.C. Bazan, J.J. Urban, M.L. Chabinyc, C.J. Hawker, R.A. Segalman, Chem. Sci. 7 (2016) 1914–1919.
[608] B. Russ, M.J. Robb, F.G. Brunetti, P.L. Miller, E.E. Perry, S.N. Patel, V. Ho, W.B. Chang, J.J. Urban, M.L. Chabinyc, C.J. Hawker, R.A. Segalman, Adv. Mater. 26 (2014) 3473–3477.
[609] D. Yuan, D. Huang, C. Zhang, Y. Zou, C. Di, X. Zhu, D. Zhu, ACS Appl. Mater. Interfaces 9 (2017) 28795–28801.
[610] D. Huang, H. Yao, Y. Cui, Y. Zou, F. Zhang, C. Wang, H. Shen, W. Jin, J. Zhu, Y. Diao, W. Xu, C. Di, D. Zhu, J. Am. Chem. Soc. 139 (2017) 13013–13023.
[611] R.A. Schlitz, F.G. Brunetti, A.M. Glaudell, P.L. Miller, M.A. Brady, C.J. Takacs, C.J. Hawker, M.L. Chabinyc, Adv. Mater. 26 (2014) 2825–2830.
[612] B.D. Naab, S. Zhang, K. Vandewal, A. Salleo, S. Barlow, S.R. Marder, Z. Bao, Adv. Mater. 26 (2014) 4268–4272.
[613] D. Madan, X. Zhao, R.M. Ireland, D. Xiao, H.E. Katz, APL Mater. 5 (2017) 086106.
[614] D. Kiefer, A. Giovannitti, H. Sun, T. Biskup, A. Hofmann, M. Koopmans, C. Cendra, S. Weber, L.J. Anton Koster, E. Olsson, J. Rivnay, S. Fabiano, I. McCulloch, C. Müller, ACS Energy Lett. (2018) 278–285.
[615] J. Liu, L. Qiu, R. Alessandri, X. Qiu, G. Portale, J. Dong, W. Talsma, G. Ye, A.A. Sengrian, P.C.T. Souza, M.A. Loi, R.C. Chiechi, S.J. Marrink, J.C. Hummelen, L.J.A. Koster, Adv. Mater. (2018) 1704630.
[616] Y. Wang, M. Nakano, T. Michinobu, Y. Kiyota, T. Mori, K. Takimiya, Macromolecules 50 (2017) 857–864.
[617] B.D. Naab, X. Gu, T. Kurosawa, J.W.F. To, A. Salleo, Z. Bao, Adv. Electron. Mater. 2 (2016) 1600004.
[618] S. Wang, H. Sun, U. Ail, M. Vagin, P.O.Å. Persson, J.W. Andreasen, W. Thiel, M. Berggren, X. Crispin, D. Fazzi, S. Fabiano, Adv. Mater. 28 (2016) 10764–10771.
[619] K. Shi, F. Zhang, C.-A. Di, T.-W. Yan, Y. Zou, X. Zhou, D. Zhu, J.-Y. Wang, J. Pei, J. Am. Chem. Soc. 137 (2015) 6979–6982.
[620] X. Zhao, D. Madan, Y. Cheng, J. Zhou, H. Li, S.M. Thon, A.E. Bragg, M.E. DeCoster, P.E. Hopkins, H.E. Katz, Adv. Mater. 29 (2017) 1606928.
[621] Y. Sun, P. Sheng, C. Di, F. Jiao, W. Xu, D. Qiu, D. Zhu, Adv. Mater. 24 (2012) 932–937.
[622] Y. Sun, L. Qiu, L. Tang, H. Geng, H. Wang, F. Zhang, D. Huang, W. Xu, P. Yue, Y. Guan, F. Jiao, Y. Sun, D. Tang, C. Di, Y. Yi, D. Zhu, Adv. Mater. 28 (2016) 3351–3358.
[623] K.C. See, J.P. Feser, C.E. Chen, A. Majumdar, J.J. Urban, R.A. Segalman, Nano Lett. 10 (2010) 4664–4667.
[624] R.M. Ireland, Y. Liu, X. Guo, Y.T. Cheng, S. Kola, W. Wang, T. Jones, R. Yang, M.L. Falk, H.E. Katz, Adv. Sci. 2 (2015) 1500015.
[625] C. Yu, K. Choi, L. Yin, J.C. Grunlan, ACS Nano 5 (2011) 7885–7892.
[626] C. Cho, K.L. Wallace, P. Tzeng, J.-H. Hsu, C. Yu, J.C. Grunlan, Adv. Energy Mater. 6 (2016) 1502168.
[627] A.D. Avery, B.H. Zhou, J. Lee, E.-S. Lee, E.M. Miller, R. Ihly, D. Wesenberg, K.S. Mistry, S.L. Guillot, B.L. Zink, Y.-H. Kim, J.L. Blackburn, A.J. Ferguson, Nat. Energy 1 (2016) 16033.
[628] D.J. Bergman, O. Levy, J. Appl. Phys. 70 (1991) 6821–6833.
[629] Y. Chen, M. He, B. Liu, G.C. Bazan, J. Zhou, Z. Liang, Adv. Mater. 29 (2017) 1604752.
[630] C.-K. Mai, J. Liu, C.M. Evans, R.A. Segalman, M.L. Chabinyc, D.G. Cahill, G.C. Bazan, Macromolecules 49 (2016) 4957–4963.
[631] B. Dörling, J.D. Ryan, J.D. Craddock, A. Sorrentino, A. El Basaty, A. Gomez, M. Garriga, E. Pereiro, J.E. Anthony, M.C. Weisenberger, A.R. Goñi, C. Müller, M. Campoy-Quiles, Adv. Mater. 28 (2016) 2782–2789.
[632] D. Kiefer, L. Yu, E. Fransson, A. Gómez, D. Primetzhofer, A. Amassian, M. Campoy-Quiles, C. Müller, Adv. Sci. 4 (2017) 1600203.
[633] C. Bounioux, P. Díaz-Chao, M. Campoy-Quiles, M.S. Martín-González, A.R. Goñi, R. Yerushalmi-Rozen, C. Müller, Energy Environ. Sci. 6 (2013) 918–925.
[634] B.A. MacLeod, N.J. Stanton, I.E. Gould, D. Wesenberg, R. Ihly, Z.R. Owczarczyk, K.E. Hurst, C.S. Fewox, C.N. Folmar, K. Holman Hughes, B.L. Zink, J.L. Blackburn, A.J. Ferguson, Energy Environ. Sci. 10 (2017) 2168–2179.
[635] Y. Nonoguchi, M. Nakano, T. Murayama, H. Hagino, S. Hama, K. Miyazaki, R. Matsubara, M. Nakamura, T. Kawai, Adv. Funct. Mater. 26 (2016) 3021–3028.
[636] W. Zhou, Q. Fan, Q. Zhang, K. Li, L. Cai, X. Gu, F. Yang, N. Zhang, Z. Xiao, H. Chen, S. Xiao, Y. Wang, H. Liu, W. Zhou, S. Xie, Small 12 (2016) 3407–3414.
[637] A.R. Abramson, W.C. Kim, S.T. Huxtable, H. Yan, Y. Wu, A. Majumdar, C.-L. Tien, P. Yang, J. Microelectromech. Syst. 13 (2004) 505–513.
[638] B. Zhang, J. Sun, H.E. Katz, F. Fang, R.L. Opila, ACS Appl. Mater. Interfaces 2 (2010) 3170–3178.
[639] S.K. Yee, N.E. Coates, A. Majumdar, J.J. Urban, R.A. Segalman, Phys. Chem. Chem. Phys. 15 (2013) 4024–4032.
[640] N.E. Coates, S.K. Yee, B. McCulloch, K.C. See, A. Majumdar, R.A. Segalman, J.J. Urban, Adv. Mater. 25 (2013) 1629–1633.
[641] M. He, J. Ge, Z. Lin, X. Feng, X. Wang, H. Lu, Y. Yang, F. Qiu, Energy Environ. Sci. 5 (2012) 8351.
[642] E.W. Zaia, A. Sahu, P. Zhou, M.P. Gordon, J.D. Forster, S. Aloni, Y.S. Liu, J. Guo, J.J. Urban, Nano Lett. 16 (2016) 3352–3359.
[643] J. Choi, J.Y. Lee, S.-S. Lee, C.R. Park, H. Kim, Adv. Energy Mater. 6 (2016) 1502181.
[644] Z. Liang, M.J. Boland, K. Butrouna, D.R. Strachan, K.R. Graham, J. Mater. Chem. A 5 (2017) 15891–15900.
[645] Y. Liu, Z. Song, Q. Zhang, Z. Zhou, Y. Tang, L. Wang, J. Zhu, W. Luo, W. Jiang, RSC Adv. 5 (2015) 45106–45112.
[646] J. Sun, M.L. Yeh, B.J. Jung, B. Zhang, J.P. Feser, A. Majumdar, H.E. Katz, Macromolecules 43 (2010) 2897–2903.
[647] G. Zuo, X. Liu, M. Fahlman, M. Kemerink, Adv. Funct. Mater. 1703280 (2017) 1703280.
[648] K. Zhang, S. Wang, J. Qiu, J.L. Blackburn, X. Zhang, A.J. Ferguson, E.M. Miller, B.L. Weeks, Nano Energy 19 (2016) 128–137.
[649] Y. Du, S.Z. Shen, W. Yang, R. Donelson, K. Cai, P.S. Casey, Synth. Met. 161 (2012) 2688–2692.
[650] L. Wang, Q. Yao, H. Bi, F. Huang, Q. Wang, L. Chen, J. Mater. Chem. A 2 (2014) 11107.
[651] K. Zhang, Y. Zhang, S. Wang, Sci. Rep. 3 (2013) 3448.
[652] T.A. Amollo, G.T. Mola, M.S.K. Kirui, V.O. Nyamori, Crit. Rev. Solid State Mater. Sci. 43 (2018) 133–157.
[653] J.L. Blackburn, A.J. Ferguson, C. Cho, J.C. Grunlan, Adv. Mater. 30 (2018) 1704386.
[654] M. Monthioux, V.L. Kuznetsov, Carbon N. Y. 44 (2006) 1621–1623.
[655] S. Iijima, Nature 354 (1991) 56–58.
[656] M. Moniruzzaman, K.I. Winey, Macromolecules 39 (2006) 5194–5205.
[657] M. Jouni, D. Djurado, V. Massardier, G. Boiteux, Polym. Int. 66 (2017) 1237–1251.
[658] C. Yu, Y.S. Kim, D. Kim, J.C. Grunlan, Nano Lett. 8 (2008) 4428–4432.
[659] D. Kim, Y. Kim, K. Choi, J.C. Grunlan, C. Yu, ACS Nano 4 (2010) 513–523.
[660] Q. Yao, Q. Wang, L. Wang, L. Chen, Energy Environ. Sci. 7 (2014) 3801–3807.
[661] H. Wang, S. Yi, X. Pu, C. Yu, ACS Appl. Mater. Interfaces 7 (2015) 9589–9597.
[662] J.-H. Hsu, W. Choi, G. Yang, C. Yu, Org. Electron. 45 (2017) 182–189.
[663] C. Cho, B. Stevens, J.-H. Hsu, R. Bureau, D.A. Hagen, O. Regev, C. Yu, J.C. Grunlan, Adv. Mater. 27 (2015) 2996–3001.
[664] C.T. Hong, W. Lee, Y.H. Kang, Y. Yoo, J. Ryu, S.Y. Cho, K.-S. Jang, J. Mater. Chem. A 3 (2015) 12314–12319.
[665] C.T. Hong, Y.H. Kang, J. Ryu, S.Y. Cho, K.-S. Jang, J. Mater. Chem. A 3 (2015) 21428–21433.
[666] J.P. Small, K.M. Perez, P. Kim, Phys. Rev. Lett. 91 (2003) 256801.
[667] M.C. Llaguno, J.E. Fischer, A.T. Johnson, J. Hone, Nano Lett. 4 (2004) 45–49.
[668] K. Yanagi, S. Kanda, Y. Oshima, Y. Kitamura, H. Kawai, T. Yamamoto, T. Takenobu, Y. Nakai, Y. Maniwa, Nano Lett. 14 (2014) 6437–6442.
[669] Y. Oshima, Y. Kitamura, Y. Maniwa, K. Yanagi, Appl. Phys. Lett. 107 (2015) 43106.
[670] B. Norton-Baker, R. Ihly, I.E. Gould, A.D. Avery, Z.R. Owczarczyk, A.J. Ferguson, J.L. Blackburn, ACS Energy Lett. 1 (2016) 1212–1220.
[671] M. Nakano, T. Nakashima, T. Kawai, Y. Nonoguchi, Small 13 (2017) 1700804.
[672] Y. Nonoguchi, K. Ohashi, R. Kanazawa, K. Ashiba, K. Hata, T. Nakagawa,

C. Adachi, T. Tanase, T. Kawai, Sci. Rep. 3 (2013) 3344.
[673] C.J. An, Y.H. Kang, H. Song, Y. Jeong, S.Y. Cho, J. Mater. Chem. A 5 (2017) 15631–15639.
[674] Y. Nonoguchi, A. Tani, T. Ikeda, C. Goto, N. Tanifuji, R.M. Uda, T. Kawai, Small 13 (2017) 1603420.
[675] C. Cho, M. Culebras, K.L. Wallace, Y. Song, K. Holder, J. Hsu, C. Yu, J.C. Grunlan, Nano Energy 28 (2016) 426–432.
[676] M. Shim, A. Javey, N.W. Shi Kam, H. Dai, J. Am. Chem. Soc. 123 (2001) 11512–11513.
[677] Y. Ryu, D.D. Freeman, C. Yu, Carbon N. Y. 49 (2011) 4745–4751.
[678] C. Yu, A. Murali, K. Choi, Y. Ryu, Energy Environ. Sci. 5 (2012) 9481.
[679] C.A. Hewitt, D.S. Montgomery, R.L. Barbalace, R.D. Carlson, D.L. Carroll, J. Appl. Phys. 115 (2014) 184502.
[680] D.S. Montgomery, C.A. Hewitt, R. Barbalace, T. Jones, D.L. Carroll, Carbon N. Y. 96 (2016) 778–781.
[681] S.L. Kim, K. Choi, A. Tazebay, C. Yu, ACS Nano 8 (2014) 2377–2386.
[682] C.J. An, Y.H. Kang, A.-Y. Lee, K.-S. Jang, Y. Jeong, S.Y. Cho, ACS Appl. Mater. Interfaces 8 (2016) 22142–22150.
[683] W. Zhou, Q. Fan, Q. Zhang, L. Cai, K. Li, X. Gu, F. Yang, N. Zhang, Y. Wang, H. Liu, W. Zhou, S. Xie, Nat. Commun. 8 (2017) 14886.
[684] H. Wang, J.-H. Hsu, S.-I. Yi, S.L. Kim, K. Choi, G. Yang, C. Yu, Adv. Mater. 27 (2015) 6855–6861.
[685] C.-K. Mai, B. Russ, S.L. Fronk, N. Hu, M.B. Chan-Park, J.J. Urban, R.A. Segalman, M.L. Chabinyc, G.C. Bazan, Energy Environ. Sci. 8 (2015) 2341–2346.
[686] R. Fritts, Thermoelectric Materials and Devices, Reinhold Pub. Corp, New York, 1960.
[687] A. Saramat, G. Svensson, A.E.C. Palmqvist, C. Stiewe, E. Mueller, D. Platzek, S.G.K. Williams, D.M. Rowe, J.D. Bryan, G.D. Stucky, J. Appl. Phys. 99 (2006) 023708.
[688] J.-P. Fleurial, A. Borshchevsky, T. Caillat, D.T. Morelli, G.P. Meisner, Fifteenth Int. Conf. Thermoelectr. Proc. ICT' 96, IEEE, (2018), pp. 91–95.
[689] X.Y. Zhao, X. Shi, L.D. Chen, W.Q. Zhang, S.Q. Bai, Y.Z. Pei, X.Y. Li, T. Goto, Appl. Phys. Lett. 89 (2006) 092121.
[690] B. Russ, A. Glaudell, J.J. Urban, M.L. Chabinyc, R.A. Segalman, Nat. Rev. Mater. 1 (2016) 16050.
[691] J.R. Salvador, J.Y. Cho, Z. Ye, J.E. Moczygemba, A.J. Thompson, J.W. Sharp, J.D. Koenig, R. Maloney, T. Thompson, J. Sakamoto, H. Wang, A.A. Wereszczak, Phys. Chem. Chem. Phys. 16 (2014) 12510–12520.
[692] J. Wang, O.I. Lebedev, K. Lee, J.-A. Dolyniuk, P. Klavins, S. Bux, K. Kovnir, Chem. Sci. 8 (2017) 8030–8038.
[693] Y. Liang, B. Böhme, A. Ormeci, H. Borrmann, O. Pecher, F. Haarmann, W. Schnelle, M. Baitinger, Y. Grin, Chem. - A Eur. J. 18 (2012) 9818–9822.
[694] T.F.T. Cerqueira, S. Pailhès, R. Debord, V.M. Giordano, R. Viennois, J. Shi, S. Botti, M.A.L. Marques, Chem. Mater. 28 (2016) 3711–3717.
[695] W. Liu, H.S. Kim, Q. Jie, Z. Ren, Scr. Mater. 111 (2015) 3–9.
[696] J. Yang, T. Caillat, MRS Bull. 31 (2006) 224–229.
[697] W. Liu, Q. Zhang, K. Yin, H. Chi, X. Zhou, X. Tanga, C. Uher, J. Solid State Chem. 203 (2018) 333–339.
[698] S. Ohta, T. Nomura, J. Appl. Phys. 97 (2005) 034106.
[699] M. Schwall, B. Balke, Materials 11 (2018) 649.
[700] G. Pastorino, J. Thermoelectr. 1 (2009) 7–10.
[701] P. Rogl, D.M. Rowe (Ed.), Thermoelectrics Handbook: Macro to Nano, CRC Press, 200632-1.
[702] M. Flambigl, P.F. Rogl, D.M. Rowe (Ed.), Modules, Systems, and Applications in Thermoelectrics, CRC Press, 2012.